On the dielectric properties of water confined in cement-like materials

PhD Thesis Submitted by

Manuel Monasterio Jaqueti

to the

University of the Basque Country

Supervised by

***Dr.* SILVINA CERVENY MURCIA**

Donostia – San Sebastián, March 2015

Abstract

Hydrated cements have pore sizes that range from a few nanometers to microns. The physical and chemical properties of cements (creep, strength, chemical reactivity and shrinkage) are significantly influenced by water molecules in this pore network. Hence, a main task to the cement science is to understand the behavior of water in the pore network to control the physical and chemical properties of cement-based materials.

It is known that the structural and physical properties of water near surfaces or confined in small cavities, can be different than those of bulk water. Solid surfaces affect the behavior of water mainly reducing the tetrahedral network of bulk water. However after decades of study, the structure, dynamics and physical properties of this near-surface water remains poorly understood.

In this thesis, we focus on the problem of the dynamics of water confined in the nano-pores of different sizes of cement-like materials by means of broadband dielectric spectroscopy. This technique has proven to be powerful when studying the reorientation dynamics of polar molecules such as water. In addition, thermal analysis and other spectroscopic techniques have been used to characterize the structure of these materials.

This thesis contains four main topics:

1) Dynamics of water in C-S-H gel, the main binding phase of cement materials. From a scientific perspective, the C-S-H gel offers an attractive confinement system where chemical and geometrical effects of the confinement of water can be investigated. In C-S-H gel, the water molecules are trapped mainly in the interlayer space between the highly disordered calcium silicate layers forming the interlayer water.

2) Dynamics of water confined in C-S-H synthesized with the addition of both silica- and amino propyl functionalized nano-particles, before the hydration reaction.

3) Dynamics water confined in tobermorite (natural and synthetic). Structurally Tobermorite is considered an analogue of C-S-H gel.

4) Dynamics of water confined in Portland cements at different water-to-cement ratio.

The results of this thesis showed that the nature of water in all these systems split into different relaxations (normally three different dynamics) depending on the different chemical environment and/or physical environment where water molecules are situated. Some relaxations were unequivocally related with water molecules relaxing in small gel pores (< 1 nm) whereas other water molecules were structurally linked to the structure of the different materials analyzed. The main relaxation of water confined in C-S-H, C-S-H with the addition of nanoparticles and tobermorite were faster than the so-called universal β-relaxation of water. By contrast, water in Portland cement was similar to the universal β-relaxation of water. The water dynamics in Portland cements showed similar characteristics to that observed in other well-defined confinement systems such as molecular sieves or MCM-41. In this thesis, we will discuss the implications of these observations.

Key-words: Water dynamics, confinement effects, tobermorite, C-S-H gel, nanoparticles, Portland cement

Acknowledgments

Antes que a nadie me gustaría agradecerle este trabajo, por supuesto, a Silvina y principalmente a su paciencia. Sin la ayuda de ambas, este trabajo no habría sido posible, tanto a nivel experimental como a nivel teórico.

Agradecer también a los nuestros colaboradores de Tecnalia: Javier Dolado, Jontxu Gaitero, y Edurne Erkizia, aportando ideas, medidas y su tiempo, y a Hegoi Manzano de la UPV, por sus ideas.

I would like to express my gratitude to Helen Jansson, my supervisor during my time in Sweden. Lovely person and nice worker. And the rest of the people in Sweden, Shuping, Arezou, Emma, etc… I cannot imagine better place to work than Göteborg.

A mi novia Susana, por aguantarme durante todo el proceso del doctorado y seguir apoyándome por voluntad propia, sin amenazas ni sobornos de por medio. Sigo sin entender la lógica de por qué sigue conmigo, hay gente buena por naturaleza.

A mis padres, Herminia y Manuel, no estaría aquí si no fuera por ellos (literalmente). Por demostrarme lo que es luchar contra viento y marea y salir indemnes. A mis hermanos, una por aguantar una infancia entera conmigo y el otro por la suerte que tuvo de librarse de ella. Y a todo el resto de mi familia, demasiado larga como para ponerla aquí, pero una sola mención especial para mi abuela y mi abuelo, que decidieron irse antes de tiempo y no esperar a los demás. No sabes lo que necesitas a la gente hasta que la pierdes.

A mis compañeros, Alejandro el boludo, Jon el moñas y mi hermano Musthafa. Que diferente habría sido todo sin vosotros. A mis desgraciadas Irma y Luisa, siempre aportando ideas, invitando a chocolates y acompañando cuando se necesitaba. Y al resto de compañeros de grupo, Amaia, Natalia, Ana, Isabel, Marina, Izaskun, Alex, Gerardo, Ewa, Lucia, Ana Lucia, Guillermina, Marian, Stephan y Guido, tanto por ayudarme cuando lo necesitaba como por aguantar mis chascarrillos. Buena gente.

Y al resto de la gente del grupo, desde Luis rellenándonos los tanques hasta Ángel silbando por los pasillos. Gracias a todos por ayudarme. Sin olvidar al MPC por financiarme y darme una mesa en la que trabajar.

Table of Contents

Notations

Along this work, cement chemistry notation has been used frequently, in some cases, in combination with general chemistry notation. In the following, we show the equivalences between both:

$S = SiO_2$	$C = CaO$	$H = H_2O$
$\bar{S} = SO_3$	$F = Fe_2O_3$	$A = Al_2O_3$

Other abbreviations used in this works were:

OPC: Ordinary Portland cement
C-S-H or CSH: Calcium silicate hydrate
LD C-S-H: Low density C-S-H
HD C-S-H: High density C-S-H
C/S or Ca/Si: Calcium to silicon ratio
w/c: water-to-cement ratio

Chapter I

Introduction to Cement Chemistry

In this chapter, we introduce the most relevant concepts on the basis of cement materials. We analyze the composition of the clinker. Then, we focus on the hydration process with particular emphasis on the structure of C-S-H gel at different scales (macro, micro and nano). Finally, we present definitions of the pore space in cementitious materials as well as the different terminology used in the literature.

a. Cement-based materials

Cement is a fine mineral powder and, when mixed with water, it transform in to a paste with the ability of binding solid mater to a compact whole. Cement is the widely used construction material in the world. An early version of cement was made with lime, sand and gravel in the old Mesopotamia (3000 years B.C. and after for the Egyptians). The first concrete was employed by the Ancient Macedonian and, some centuries after, by the Roman engineers on a larger scale [1]. However, all this knowledge was lost during the middle Age. In 1756, John Smeaton experimented with a combination of different limestones and additives recovering the idea of improving cement materials. In the late 18^{th} century, Roman cement became very popular until it was replaced by Portland cement in the 1850s. This material was extensively used by Joseph Aspdin (patented in 1824), and its name comes from the Portland stone used in its fabrication. This proto-Portland cement was then further improved until obtaining the material we use nowadays [2].

Last year, the cement world production was about four thousand millions of tons (figure I.1a) [3]. One of the main environmental problem during the cement production is the released of carbon dioxide. In particular, cement industry produces about 5% of global CO_2 emissions, with a total emission nearly of 900 kg of CO_2 for every ton of produced cement [4]. With the aim of both to increase the production and to control the emissions, a large research of cement materials was done in the last years. On the one

hand, most efforts were directed towards increasing the strength of the cement-binder and saving cost in the production. On the other hand, research efforts focused on enlarge the knowledge the basic problem of cement chemistry and chemical reacting occurring during hydration.

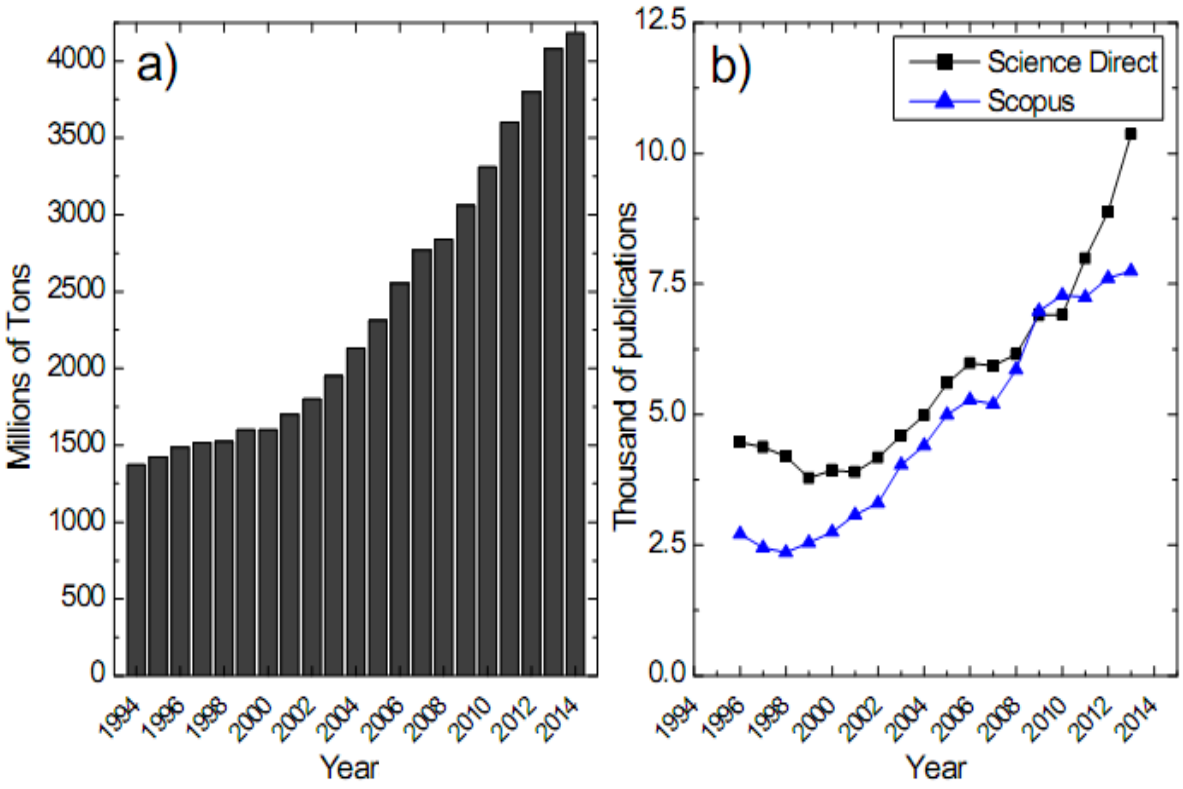

Figure I.1. a) The cement global production (1994 to 2013). b) Number of publications using the word "cement" in different search engines.

The above mentioned researches efforts are reflected in figure I.1.b). As shown, the amount of cement related publications has increased in the analyzed period. Although most of users are not aware of their existence, the understanding of both the complex chemical reactions occurring within cement during hydration and the influence of the obtained pore structure in the final strength of the materials is of utmost importance. Cement research is therefore a multidisciplinary field where civil engineers and architects involved in the construction of large buildings, as well as physicists and chemists, involved in nanoscale characterization and simulations, cooperate in order to reach the objective of a better understanding of this material.

Cements can be classified into two large groups: hydraulic and non-hydraulic cements. The cement usually used in construction is the hydraulic type, due to its better performance. Some examples are Portland, calcium sulfoaluminate or geopolymeric cements.

Ordinary Portland Cement (OPC) is defined as a material composed by two thirds (in mass) of calcium silicates and one third of aluminium and iron oxides. In addition, there are other sub-classifications of Portland cement which in turn depend on composition and additives. Raw Portland cement is a combination of clays and limestone grinded and stirred until obtaining a fine, homogeneous powder (clinker). This powder mixture is then introduced in a shape-cylinder oven with a slow rotation and a temperature gradient along the rotation axis: 1) from 100ºC to 900ºC, the thermal decomposition of the mixture occurs (with the limestone and silicoaluminates dissociation, and the elimination of water and OH from the clays); 2) from 700ºC to 1350ºC, the solid state reactions occurs and the heat produce belite (C_2S), tricalcium aluminate (C_3A) and aluminoferrite (C_4AF); and 3) from 1350ºC to 1600ºC, when alite (C_3S) is obtained [5]. The mixture is then cooled and stored in the form of "clinker".

Table I.1. The Initial and final components of the clinker with its percentages.

Initial components		Final components	
CaO	60-69%	Alite	60-70%
SiO_2	18-24%	Belite	15-30%
Al_2O_3	4-8%	Tricalcium aluminate	5-15%
Fe_2O_3	1-8%	Aluminoferrite	7-15%

Once the above mentioned process is completed, the cement is prepared to be hydrated (process in which it will acquire the grey color and the hardness).

b. Clinker

The clinker is the primary material of the cement production process. The raw materials involved in clinker production are directly obtained from the quarry (see table I.1.). After the first grind (homogenization), the clinker is placed in a rotary oven, where the previously described temperature reactions occur.

In a more detailed view, the first reaction is a thermo decomposition of the primary materials. The most important process in this step is the limestone decomposition at about 650ºC, producing CaO. In addition, the clay decompose in its basic oxide components by losing OH, $2Si_2Al_2O_5(OH)_4 \rightarrow 2Si_2Al_2O_7 + 4H_2O$ and later producing Si and Al oxides $Si_2Al_2O_7 \rightarrow 2SiO_2 + Al_2O_3$. During the second step the solid state reactions occur, thus producing belite (C_2S), aluminate (C_3A) and ferrite (C_4AF). Finally, in the third step the molten state reactions take place i.e: the belite reaction at 1450ºC with the calcium oxide to form alite (C_3S) [6]. All this reactions are represented in figure I.2 as a function of the temperature. After leaving the oven, the clinker is fast cooled in order to avoid crystal growing (which would have a negative influence on the subsequent hydration and the mechanical resistance of the cement).

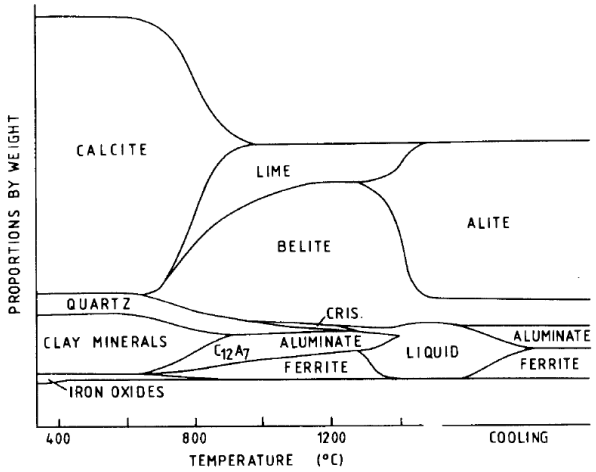

Figure I.2. Schematic diagram showing the variations in typical contents during the formation of Portland cement clinker [7].

A brief description of the principal components of the clinker is shown below:

b.1 Alite ($3CaO \cdot SiO_2 = C_3S$)

Alite is a mineralogical compound and the main component of Portland cement. It is the chemically modified form of pure tricalcium silicate (C_3S). It presents reversible transitions, being triclinic morphology (T_1) the most stable at room temperature. Figure I.3 shows the Alite structure.

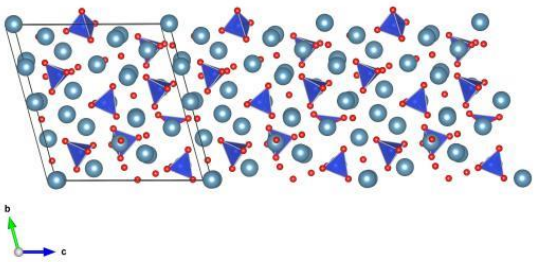

Figure I.3. Structure of Alite by Vesta, with projection 110 [8]. The blue balls represent the calcium atoms, the blue triangles represent the silicon tetrahedronds, and the small red balls are oxygen.

b.2 Belite ($2CaO \cdot SiO_2 = C_2S$)

Belite is responsible (together with alite) of the formation of C-S-H gel. Belite is a mineralogical compound known to take four polymorphs forms which easily reacts with water and transform into hydrated dicalcium silicate. The crystal structure of belite (see Figure I.4) is similar to alite, with SiO_4^{-4} tetrahedra and Ca^{+2} ions (but lacking the O^{-2} ions). The structures of α'_H, α'_L, and β polymorphs are derived from that of α-C_2S by progressive decreases in symmetry (in turn derived from changes in the orientation of the $Si0_4^{-4}$ tetrahedra and small movements of Ca ions).

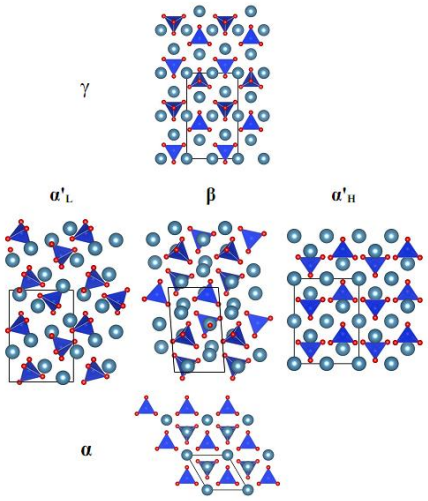

Figure I.4. Representation of belite on their multiples polymorphics. Projection is 101 for all phases except α, where it is 110. The blue balls represent the calcium atoms, the blue tetrahedrons are silicon atoms, and the small red balls are oxygen.

b.3 Tricalcium Aluminate ($3CaO \cdot Al_2O_3 = C_3A$)

Tricalcium aluminate (C_3A) is the third most abundant component in Portland cement. The C_3A has a cubic symmetry and is stable all along the explored temperature range. C_3A unit cell is composed of $Al_6O_{18}^{-18}$ rings, with their charge balanced by Ca^{+2} ions located in the space between them [9].

Na substitution dominates and continues determining which polymorph is obtained (substitution of $2Na^{+}$ by Ca^{+2} produces a decrease in the symmetry, and consequently, the appearing of orthorhombic and monoclinic polymorphs). A cubic symmetry is maintained as long as the Na_2O content is below 2%, while orthorhombic symmetry appears if this content is above 4.5%. Other kinds of substitutions can be observed, as Al^{+3} by Fe^{+3} or Si^{+4} [10] (the partial substitution by Fe^{+3} has relatively little effect on the polymorphism of the aluminate [2]).

In the OPC clinkers at room temperature, the monoclinic form has not been detected while the cubic and orthorhombic polymorphs appear, alone or in combination. The cubic form is usually mixed with dendritic crystals of ferrite phases [5].

b.4 Aluminoferrite ($4CaO \cdot Al_2O_3 \cdot Fe_2O_3 = C_4AF$)

Aluminoferrite is the fourth element of the clinker, and a modification of ferrite (C_2F) in which aluminum atoms enters into the structure. At room temperature and pressure conditions, the solid solution $Ca_2(Al_xFe_{1-x})_2O_5$ can vary between x = 1 to about 0.7 (being the C_4AF possible only with x = 0.5 and C_2A with x = 1, the latter only for high pressures [11]). Each Ca^{2+} ion in C_4AF has 7 oxygen neighbors at 0.23-0.26 nm [12]. The aluminum and iron atoms are both distributed between octahedral and tetrahedral sites, and the fraction of the aluminum entering tetrahedral sites under equilibrium conditions decreases with temperature. In the unit cell of pure C_2F there are two different positions occupied by iron ions, one with tetrahedral and the other one with octahedral coordination (being the number of the latter twice the number of the former). When a high amount of titanium enters the structure perovskite-like zones appear mixed with ferrite [2,13].

c. Hydration Process

The hydration process in cement chemistry represents the chemical reactions which take place when clinker is in contact with water. This is a very complex process, mainly due to the amount of different reactions involved (as well as the components, the additives, and the different clinker phases, in turn with their own particle size, shape, and impurities). For all these reasons, although from a macroscopic point of view it seems a simple reaction, clinker hydration is not yet well understood. In figure I.5 a scheme of the hydration products as a function of reaction time is shown.

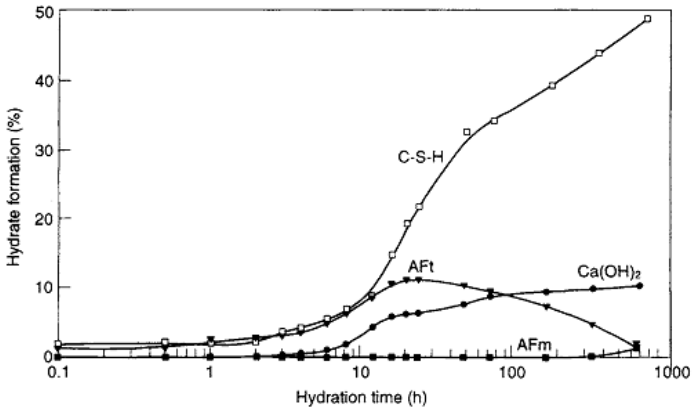

Figure I.5. General representation of the amount of hydration products in function of reaction time [2].

A small deviation of a variable as the amount of water, yield large changes in the final properties of the product, as the Young's moduli [7] or the pores sizes [14]. As a consequence, research efforts for understanding such a complex behavior were done since the early XX century [15,16] and continue until our days. The most important chemical reactions in the hydration process of the cement are described below:

c.1 Hydration of Alite

Alite hydration is the responsible of the hardness of cement during the first days. The equation of the alite hydration can be written as:

$$2Ca_3SiO_5 + 6H_2O \rightarrow 3CaO \cdot 2SiO_2 \cdot 3H_2O + 3Ca(OH)_2 \qquad \text{(I.1)}$$

or in the cement notation:

$$2C_3S + 6H \rightarrow C - S - H\ gel + CH \quad \text{(I.2)}$$

The hydration of alite is rather complex and fast. About the 70% of alite reacts in the first twenty eight days, and almost the 100% after one year. The products obtained in this reaction (C-S-H gel and portlandite) are main components of the cement. The stoichiometry of the C-S-H gel is not fixed and the eq. (I.2) is only approximated. Other stoichiometries of the reaction can be expressed as:

$$2CaO \cdot SiO_2 + (3 + m - n)H_2O = nCaO \cdot SiO_2 \cdot mH_2O + (3 - n)Ca(OH)_2 \quad \text{(I.3)}$$

c.2 Hydration of Belite

The hydration reaction of belite equation (in its β phase) is similar to the alite. The main difference is the lower production of Portlandite. The reaction equation can be written as [17]:

$$4CaO \cdot 2SiO_2 + 4H_2O \rightarrow 3CaO \cdot 2SiO_2 \cdot 3H_2O + Ca(OH)_2 \quad \text{(I.4)}$$

or in cement notation:

$$2C_2S + 4H \rightarrow C_3S_2H_3 + CH \quad \text{(I.5)}$$

Despite the produced amount of Portlandite, another difference with the alite reaction is the kinetics. The velocity of this reaction is much lower than the alite. In twenty eight days only 30% of belite has reacted and the 90% in one year. The hydration in the β and α phases is similar, while in the γ phase it does not occur (as already mentioned in the previous section, γ is a non-reactive phase).

c.3 Hydration of tricalcium aluminate

The tricalcium aluminate hydration affects the workability of the final cement. When alite reacts with water, a very fast process starts. The explanation of this lies in the formation of a protective barrier of hydration products (hexagonal hydrates) upon

the alite surface. The conversion of the hexagon hydrates into cubic breaks this barrier and the hydration is again fast (accompanied by intense heat release) (in cement notation):

$$2\ C_3A + 27\ H \rightarrow C_4AH_{19}(C_4AH_{13}) + C_2AH_8 \rightarrow 2\ C_3AH_6 \quad \text{(I.6)}$$

The addition of sulfates, such as gypsum, has the objective of control the cement setting. In this way, ettringite is obtained as the first hydration stable product with enough amount of calcium sulfate. During the reaction, when sulfate level decreases, ettringite becomes unstable and transforms into C_3A:

$$C_3A + 26H + 3C\bar{S}H_2(gypsum) \rightarrow C_6A\bar{S}_3H_{32}(ettringite) \quad \text{(I.7)}$$

$$C_6A\bar{S}_3H_{32} + 2\ C_3A + 4H \rightarrow 3\ C_4A\bar{S}H_{12} \quad \text{(I.8)}$$

without gypsum the reaction is faster:

$$C_3A + 6H \rightarrow C_3AH_6 \quad \text{(I.9)}$$

In fact, the reaction is so fast that it results in flash set, which is the immediate stiffening after mixing, making proper placing, compacting and finishing impossible.

Experimentally, ettringite crystals are always over the surface of alite particles. Therefore, the common interpretation is that ettringite forms in early stages as a layer over the alite, preventing the diffusion of sulfate, hydroxide and calcium ions and creating an induction period. Once the liquid phase has fault of calcium and sulfate ions, ettringite transforms into $C_3A\bar{S}H_{12}$. There is some controversy about the real implication of the sulfates, due to the fact that some authors have proposed that the sulfate groups block the reactive points in the alite surface [18,19].

c.4 Hydration of Aluminoferrite

Hydration of C_4AF is similar in many aspects with alite phase but slower. It hydrates rapidly but it contributes slightly to the final strength. Its use allows lower kiln

temperatures in portland cement manufacturing. It acts as a flux in clinker manufactor and imparts grey color. Hydration reaction is:

$$C_4AF + 2\,CH + 14H \rightarrow C_4(A,F)13H + (A,F)3H \qquad \text{(I.10)}$$

d. Mechanism of Hydration

The hydration of cement has been deeply studied. The term "hydration" comprises all the physical and chemical processes in the cement-water system. This includes the dissolution of clinker phases, formation of hydrated phases and the diffusion processes at longer/later hydration times.

It can be separate in five different steps, as seen in the calorimetric measurements represented in figure I.6.

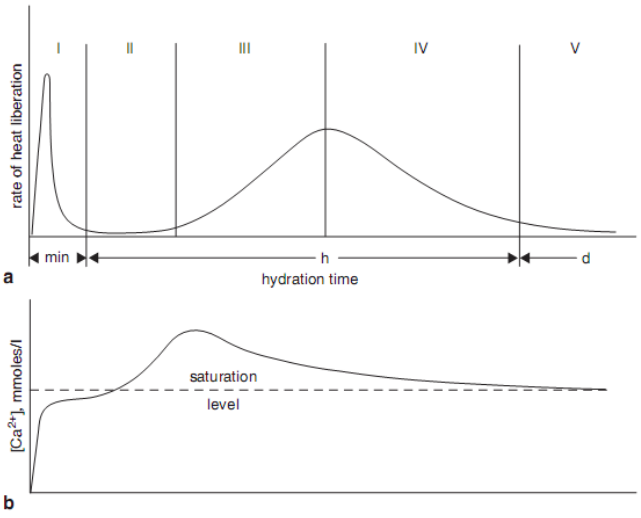

Figure I.6. Microcalorimetric curve of C_3S (a), change of Ca^{2+} ions concentration in the liquid phase (b), formation of hydrates [20].

The hydration of cementitious materials is time dependent and can be divided into five major periods [5]:

- **Initial reaction period.** As soon as the anhydrous grain comes into contact with water, soluble components such as alkalis calcium sulfate phases and free lime are dissolved by the surrounding water. The main reaction of this period is the

exothermic reaction of C_3A with gypsum. The solution formed increases in pH until a point of super saturation is attained.

- **Dormant or induction period.** This period is characterized for the slow and steady reaction which the degree of hydration and microstructure not present relevant changes. The initial set of the paste occurs at the end of this stage.

- **Acceleration period.** C_3S and C_3A are accelerated to a high level of activity and maximum reaction is reached. Outer C-S-H starts to form from the reaction of C_3S with water making the strength of the paste increase. C_2S starts to react at lower rate of reaction if compared with C_3S and C_3A. Pore volume starts to decrease with increasing of reactions and decreasing of w/c ratio.

- **Period of deceleration.** The rate of reaction decreases and the reaction get controlled by the diffusion of silicate trough a layer of existing products. Inner C-S-H starts to form on inside of the shell from the continuing hydration of C_3S. Secondary reaction of C_3A takes place and producing long rods of Aft.

- **Final slow reaction**. This is a period of steady reaction and decreasing of diffusion process. The deposition of hydrates becomes inhibited by lack of space. From one to three days, C_3A reacts with Aft forming hexagonal plates of AFm. At approximately seven days, inner C-SH formed is sufficient to decrease the separation of the "shell" and core of the paste. In order it reduces the porosity of the cementitious matrix. And the outer C-S-H becomes more fibrous. The hydration proceed slowly, some of the remaining anhydrous material reacts to form additional inner C-S-H. The ferrite phase appears to remain unreacted.

e. Structure of hydrated cement

The cement paste is a complex system with a great number of components. In the cement paste we can find together components with a crystalline defined structure (for instance portlandite), components semi-amorphous (C-S-H gel) and even anhydrate clinker particles of different sizes. The location inside the paste of these different

elements depends of the initial conditions and also of the composition and size of the clinker particles. For this reason is important a good heterogeneous mixture in the first steps of clinker preparation. The pore structure has a great relevance on the final properties of the product; therefore we describe the three different levels in the cement:

e.1 Macro scale

In the macro scale, the cement paste is considered homogeneous and aggregates can be distinguished (see Figure I.7). In this scale the pore size is located in the range of 0.1-0.5 mm, generally produced by the air introduced during the cement hydration. These pores are very harmful for the mechanical properties of the cement [21].

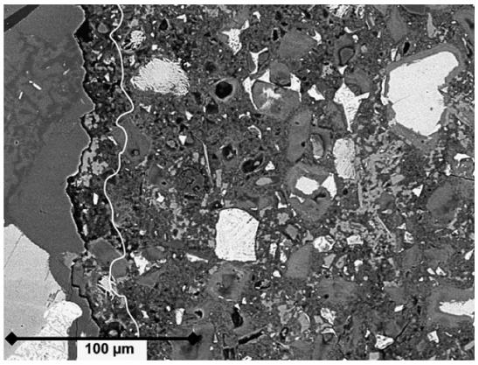

Figure I.7. Backscattered electron imaging image of concrete including paste aggregate interface. [22]

e.2 Micro scale

In this scale (between the millimeter and the nanometer), we can observe that cement is a heterogeneous composition of different elements (see Figure I.8). The C-S-H gel appears as an amorphous material. The initial parameters, (for instance, the water-to-cement ratio [23]), the stage of the grow of the hydration products and the available space [24] have a relevant importance in the morphology of C-S-H.

C-S-H can be divided in two categories: the inner C-S-H and the outer C-S-H [2,5,25]. The inner C-S-H grows towards the inside of the clinker grain, occupying the place of the anhydrous phases while the outer C-S-H grows outwards the boundaries of clinker grain, space occupied by the water. The inner C-S-H is more compact and

amorphous than the outer C-S-H [5]. With regards to the crystalline components, the portlandite is easier recognizable as hexagon shapes crystals. In this scale, we found capillary pores as a consequence of the empty space when the hydration products replace the space occupied initially for the water and cement. The sizes of these pores change in function of the age of the cement. For early hydration cements, the size can reach 5 micrometers while for old cements, the size is between 10 and 50 nanometers [21].

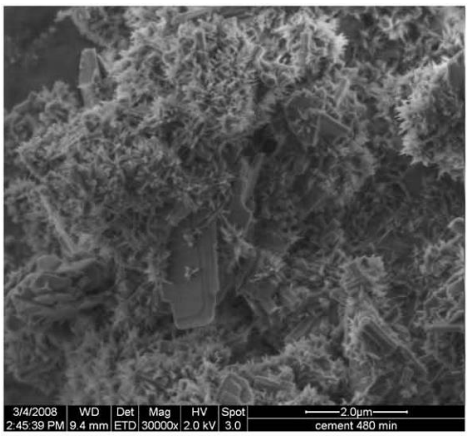

Figure I.8. SEM pictures of cement surface hydrated for 480 min [26]

e.3 Nano scale

In this scale ($<10^{-6}$m), we focus on the C-S-H gel structure. It is a very heterogeneous material and, consequently, it is difficult to obtain an accurate description of its structure. All the pores at this scale are inside of C-S-H and they induce processes as shrinkage or creep. Due to the importance of C-S-H gel, the structure and models to describe it will be discussed below.

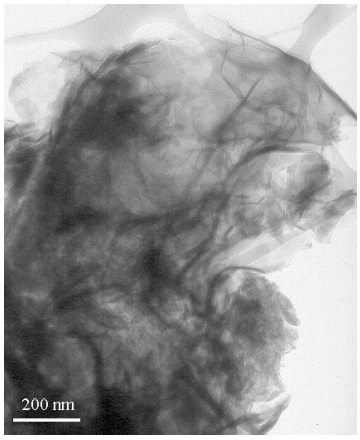

Figure I.9. TEM image of a synthetic C-S-H [27].

f. Hydration cement products

Here we describe the different elements obtained during or after the hydration. These final products define the cement properties and they depend of the all previous factors, as the water-to-cement ratio or curing time.

f.1 Calcium hydroxide ($Ca(OH)_2$)

Calcium hydroxide known as portlandite and with the chemical formula $Ca(OH)_2$ or CH in cement notation, is a crystalline product that occupies about 25% of volume in the paste. The size of each crystal is about a micrometer [28]. Portlandite has a hexagonal structure consisting of octahedrally coordinated calcium ion layers and tetrahedrally coordinated oxygen layers with hydrogen bound to oxygen as we can see in Figure I.10. The layers are too far away to establish hydrogen bond or other kind of interaction, thus the layer only interact themselves by weak dispersive forces [29].

The incidence of portlandite to the mechanical strength of the cement is negligible. However, it plays an important role in the degradation processes (as calcium leaching [30,31]) or in the corrosion of metals and the carbonatation. The carbonatation process is a degradation produced by the atmospheric CO_2 in contact with the calcium inside the portlandite. This degradation is faster in presence of water [32]. The presence of large portlandite amounts ensures the high alkalinity levels of the cement paste, and protects the metals [21].

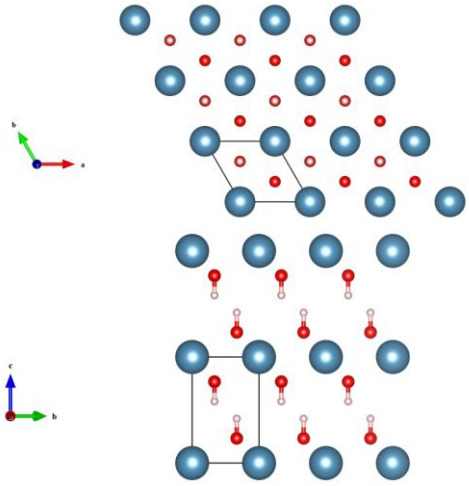

Figure I.10. Portlandite structure from two different points of view, being the blue balls the calcium, the red balls the oxygen and the white balls the hydrogen atoms.

f.2 Ettringite ($C_6A\bar{S}_9H_{32}$)

Ettringite is the result of the hydration processes of aluminate and ferrite clinker phases with gypsum. During the hydration, when all the gypsum is consumed, the dissolution of aluminate continues and ferritephases consumes the ettringite to form another product with lower sulphate content. Despite this, the ettringite can survive this depredation and persist in the cement paste, with rod-shaped morphology, reaching until 10 micrometers of length [5]. Ettringite belongs to the AFt family of compounds (Al_2O_3-Fe_2O_3-trisulpho). The ettringite structure is based on columns arranged parallel, formed by aluminium atoms octahedrally coordinated to hydroxyl groups alternated with three calcium atoms in a plane. The Ca atoms share and are coordinated to the hydroxyl groups of aluminium and to four water molecules placed in the space between columns. The stoichiometry of the columns leads to a charge excess, which is neutralized by sulphate ions placed in the channels between these columns [33,34].

f.3 Monosulphoaluminate ($C_4A\bar{S}H_{12}$)

Monosulphoaluminate is an AFm compound (Al_2O_3-Fe_2O_3-monosulpho), which is generated in the cement paste after the dissolution of ettringite, when the gypsum content has been consumed. It has a stoichiometry C_4ASH_{12}, with a layered structure

derived from that of portlandite. One in three Ca^{+2} ions are replaced by Al^{+3}, distorting the principal layer and displacing alternate calcium atoms in opposite directions from the centre of the sheet. The charge defect is compensated by the inclusion of SO_4^{-4} ions in the intralayer space, surrounded by water molecules. The water content is uncertain, variable in the range between 12 to 18 molecules per unit cell [5]. The structure of low water content varieties has not been yet determined. However, the most hydrated variety (with 18 water molecules in the interlaminar space) has a natural analogue called kuzelite, for which the structure is fully resolved [35].

f.4 C-S-H gel (Calcium silicate hydrate)

C-S-H gel is the most important hydration product in the cement. It constitutes up to the 70% of volume of the solid phase, and is the main responsible for the chemical and mechanical behavior of the paste. The acronym C-S-H stands for Calcium-Silicate-Hydrated with no fixed stoichiometry.

C-S-H gel is a poorly crystalline material (semi-amorphous) of variable composition with a layer structure, similar to that of the mineral analogue tobermorite. Due to this poor crystalline structure, the accurate description of the C-S-H gel structure at the nanoscale is difficult. The electron microscopy techniques do not have enough resolution nowadays to reach the small sizes necessary to investigate the disordered C-S-H gel structure, thus indirect methods as NMR, IR or X-Ray are the only available techniques to investigate it [36,37].

A typical idealization of C-S-H gel structure is showed in figure I.11. The gel is composed of silicate chains separated by calcium oxide layers, forming a layered structure. Water molecules occupy the interlayer space and also ions (Na^{+1} or Ca^{+2}) are present in the solution [25,38,39]. The silicate chains follow a wollastonite-like arrangement [40]. Each unit is an orthosilicic acid group, $Si(OH)_4$, which has polymerized by condensation reactions to form the chains. In a early Portland cement pastes, almost all the chains are dimers, although they continue growing and the mean chain length after 23 years is 4.8 [41]. To explain the length of silicate chains, Richardson proposed the growth model, where a dimer cannot continue growing to form

a trimer, however two dimeric structures merged through a bridging monomer to form the pentamer [25,39,42].

C-S-H gel structure is not whole fixed, and for this reason, calcium silicon ratio (Ca/Si ratio) is generally used to characterize its composition. In first steps of hydration, the Ca/Si ratio value is between 1 and 2, but this value changes at final steps of the hydration, obtaining finally a mean value around of 1.75 [39,43].

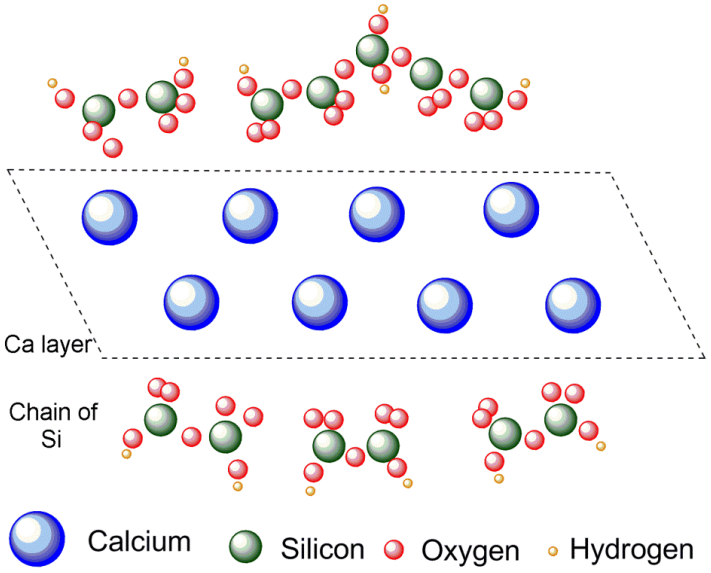

Figure I.11. Schematic representation of the C-S-H gel. The length of silicate chains keeps together by a Ca-O layer. The atom sizes are not to scale.

As we mentioned above, the C-S-H structure is not whole fixed, however in nature exists two minerals (tobermorite and jennite) with a similar structure and normally used as a model system for C-S-H gel.

f.4.1 Tobermorite ($Ca_5Si_6O_{16}(OH)_2 \cdot 7\ H_2O$)

Tobermorite can be found in three different structures: tobermorite 9Å (or riverseidite), tobermorite 11Å, and tobermorite 14Å (or plombierite). All these structures are built of calcium oxide layers ribbed on both sides by silicate chains, forming layered structures, with water molecules and extra Ca^{+2} ions in the interlaminar space. The difference between the above mentioned forms of tobermorite is the

interlayer distance, labeling in the name of the structure. The space between the layers is filled with water.

The tobermorite more similar to C-S-H gel is the so called tobermorite 14Å, due to the high amount of water in comparison with the others structures [23]. The tobermorite 11Å is a natural mineral (see figure I.12) but it can be also synthesized under hydrothermal conditions [44].

The structure of tobermorite 14 Å is formed by a central calcium oxide layers connected with silicate chains in both sides. The silicate chains follow the already cited wollastonite-like arrangement, repeating the structure every three silicate tetrahedral. Two silicates tetrahedral are nearly connected to the calcium oxide layer while the remaining one is oriented to the interlaminar space. The Ca/Si ratio is ≈ 0.83, with a density of 2.20 $g \cdot cm^{-3}$ [44].

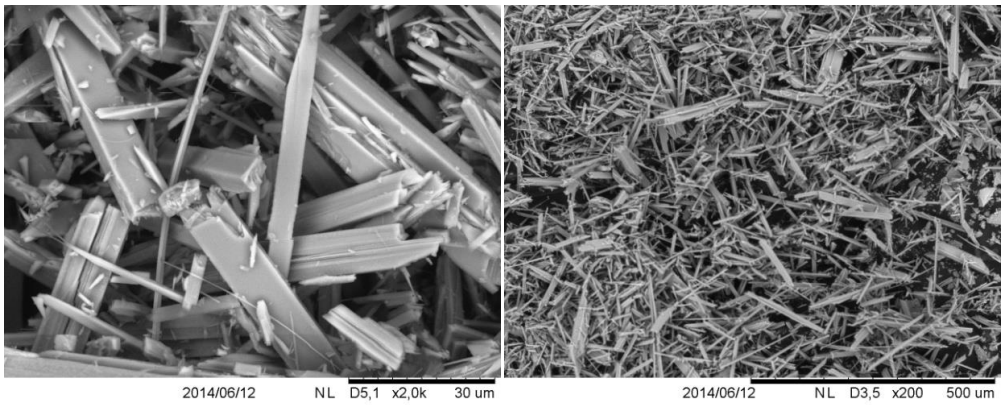

Figure I.12. SEM images of Natural Tobermorite at different magnifications.

f.4.2 Jennite ($Ca_9Si_6O_{18}(OH)_6 \cdot 8\ H_2O$)

Jennite is a very rare mineral in nature, similar to tobermorite [45]. The structure of the jennite is similar to that of tobermorite with two differences: a) The tetrahedral silicate chains are also connected with the calcium-oxide layer and b) only half of the calcium atoms are connected with the oxygen atoms of the silicate group due to the higher content of calcium in the layer. Other half is connected to the hydroxyl groups which join the calcium oxide layer. The silicate chains are shifted, and the layers are charged negatively, counterbalanced by the Ca^{+2} ions placed in the interlayer space

together with water molecules. The Ca/Si ratio value is around 1.5 and the density is 2.325 $g \cdot cm^{-3}$ [46].

g. Models for C-S-H gel – Porosity characterization

This thesis deals with the study of water in the porosity of cementitious materials. Therefore, in this section we describe in detail different models to characterize the porosity of hydrated materials. There are still several questions about the pore space in cementitious materials and therefore model systems can help to describe the experimental results obtained for different characterization methods such as low temperature calorimetry, area BET and scanning electron microscopy (SEM).

g.1 Microstructure

Microstructural models are used for a representation of the complex pore network in the hydrated materials [47–50]. In the following we focus on models describing the structure of C-S-H gel.

There are two different types of models: from one side it was suggested a granular model for C-S-H [47,49], and the other side, C-S-H was proposed to be composed of sheets with granulated structures [48].

The early work of Powers and Brownyard [47,51] proposed that the C-S-H gel is composed of particles that have a layered structure arranged randomly and bonded together by surface forces as in clays (Figure I.13.a)). Later Feldman and Sereda [48] improved this model by considering that the sheets composing the C-S-H gel do not have an ordered layered structure but they are rather an irregular array of single layers in which water molecules are structurally incorporated in the C-S-H structure (see Figure I.13.b)). These surfaces are covered by hydroxyl groups which are able to establish hydrogen bonds with the surrounding water molecules. McDonald et al. [50] proposed that water in a C-S-H gel pore can be immobile or mobile depending if water is intra CSH sheet or inter CSH sheet (see Figure I.13.c)).

We finally put special emphasis on the most recent colloidal model (CM) proposed by Jennings [49] since it can explain most of the experimental results reported in the literature regarding to hydrated cement. According to this model, the basic unit of C-S-H is a colloidal particle (globules) having a size of about 4 nm with a layered internal structure, in agreement with other models in the literature. During hydration, these globules form clusters to produce a porous structure with two different characteristic lengths: small gel pores (dimensions 1–3 nm) and large gel pores (dimensions 3–12 nm). Consequently, during the cure reaction water can be located in different confinement lengths ranging from 1 to 12 nm. It is important to note that the observation of the basic globule of C-S-H is very difficult. The only attempt in the literature corresponds to the atomistic study of Dolado et al. [52]. The authors studied the formation of C-S-H clusters by molecular dynamic simulations to predicte the appearance of a branched C-S-H nanostructure with segments of 3 x 3 x 6 nm^3 sized which provided a satisfactory comparison with numerous experiments.

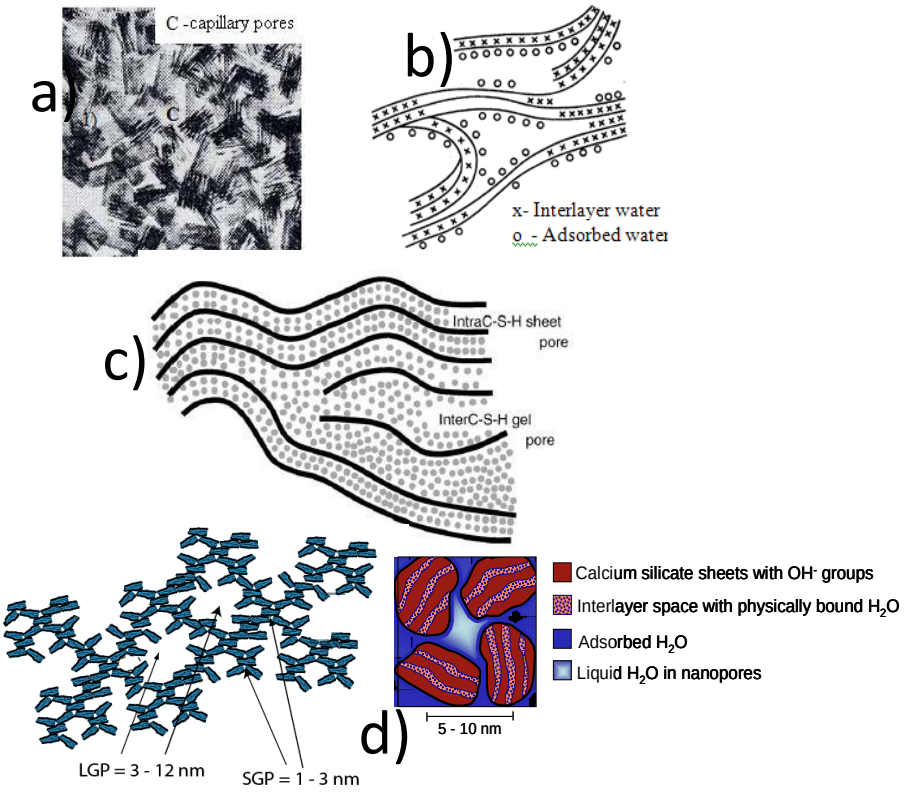

Figure I.13. Models for C-S-H structure: (a) Powers [47]; (b) Feldman and Sereda [48]; (c) McDonald et al.[50]; (d) Jennings [49].

Despite a great number of models, the pore structure formation in hydrated cementitious materials is not fully understood. The pore structure is very complex and it changes with curing conditions or even with the inclusion of other supplementary materials, which makes it difficult to model and describe it in detail.

The present thesis has the aim to contribute for the pore structure characterization of hydrated cementitious materials by studying the dynamics of confined water.

In the following, we focus on the different classification of the pores in cementitious materials.

g.2 Pores in cementitious materials

When water reacts with cement, a porous material is obtained. After the reaction, part of water remains free in the pore space whereas other part forms structural component of the new solids.

Pores in cementitious are defined as empty space or space which is filled with water. In the literature there are different pore classifications and also different terminology is used.

A typical pore size distribution for hydrated cement covers a large range of pore sizes, from about a cm to as small as nm in diameter. Figure I.14 and Table I.2 show the different range of pores as well as the different terminology used in the literature.

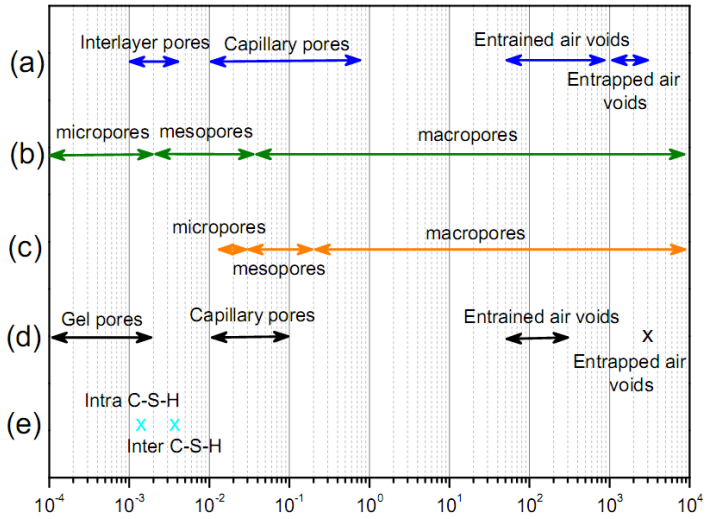

Figure I.14. Range of pores and nomenclature used in the literature. a) Powers and Brownyard [47], b) IUPAC, c) Mindess [53], d)Metha-Monteiro [54] e)McDonald [50]

Table I.2. Classification of pores and features in concrete [55]

Type of Pore	Description	Size	Water
Capillary pores	Large	10 μm – 50 nm	Evaporable bulk water
	Medium	50 – 10 nm	Evaporable moderate menisci
Gel pores	Small	10 – 2.5 nm	Evaporable strong menisci
	Micropores	2.5 – 0.5 nm	Non-evaporable Intermolecular interactions
Interlayer spaces	Structural	< 0.5 nm	Non-evaporable Ionic/covalent bond
Other features	ITZ	20 – 50 μm	Bulk water
	Microcracks	50 - > 200 μm	Bulk water

The most common pore classification and the one used in this thesis is the following:

- Small gel pores
- Big gel pores
- Capillary pores
- Air voids

g.2.1 Gel pores, interlayer spaces in C-S-H, micropores, nanopores

Gel pores might be defined as: "the gel porosity in the intrinsic part of the C-S-H" [5]. Gel pores contribute to about 26% to 28% of paste porosity.

According to Powers [56] the gel pores size is about 0.002 to 0.004 μm of diameter. Feldman and Sereda [48] proposed that the width of the gel pores could

fluctuate from 0.0005 to 0.0025 μm. McDonald and co-workers have proposed 0.004 μm for inter C-S-H gel and 0.0015 μm for intra C-S-H gel [50].

At the present time, the most successful model is the Jennings model as above mentioned. In this model, Jennings analyses the N_2 sorption with a measurement of Specific Surface Area (SSA) by Small Angle Neutron Scattering (SANS) and proposed the existence of two different types of C-S-H gel, based in their porosity [57]. In the model (CM-I, see Figure I.13 (d)), the C-S-H gel forms spherical building blocks with radius around 1.2 nm and with densities of 2.8 g/cm^{-3}. Those spheres formed bigger structures called "globules" of 3 nm of radius with the density changing in function of the water content. These globules are packed in two different forms in function of their package factor: High Density (HD) and Low Density (LD). The main difference is that in HD C-S-H gel N_2 cannot penetrate, meanwhile opposite occurs with LD C-S-H gel. In addition, SANS measurements cannot resolve where the HD C-S-H is located.

In the Colloidal Model-II (CM-II), the microstructure of a cement paste can be schematically described as in Figure I.15. The basic globule is a disk-like object, whose thickness is around 4 nm, having a layered internal structure. The water inside the globule is located both in the interlamellar spaces and in very small cavities (intraglobular pores, IGP), with dimensions of 1 nm. The packing of these globules produces a porous structure, where two other main pores populations can be identified: the small gel pores (SGP), with dimensions 1-3 nm; and the large gel pores (LGP), 3-12 nm in size. The inclusion of the sub-nanometric porosity in the description of the microstructure justifies most of the experimental evidence, representing a decisive step for the understanding and the control of the relationships between structure and properties.

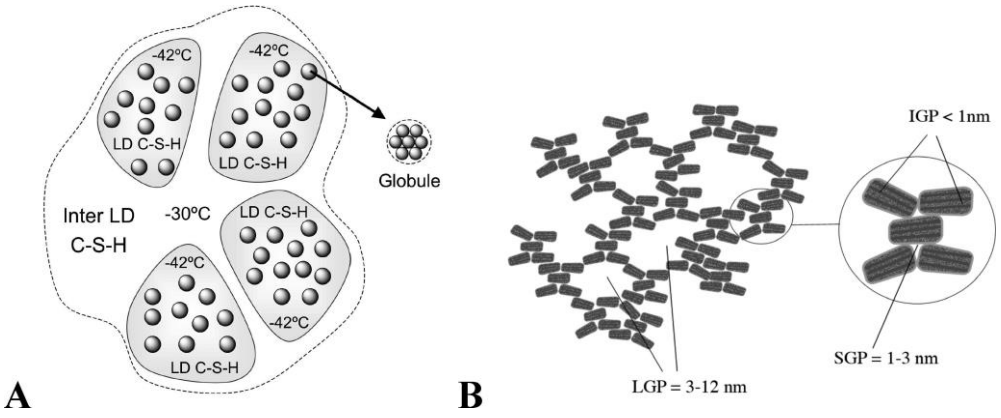

Figure I.15. Scheme representation of the CM-II.

g.2.2 Capillary pores, macropores, mesopores

Capillary pores (also called macropores or mesopores) are defined as the empty spaces after the hydration reaction takes place.

Capillary pores depend on initial separation of cement particles, which is controlled by the *w/c* ratio. Studies have reported that capillary pores are direct related to the strength and durability issues [53].

g.2.3 Air voids

Air voids are generally spherical and they are usually divided in entrained (50 to 200 μm) and entrapped (approx. 3 mm) air voids. Entrapped air is the empty pores formed during the mixing and casting process. Entrained air is air purposely entrained by the addition of admixtures to the cement mixture.

h. Water in cement-like materials

Water is indispensable for the reaction of cement particles. Water is introduced during the process of mixing of the cement paste. The state of the pore water depends on the size of the pores and the ions in solution. Sereda [58] classified the water contained in cement pastes into three types:

(1) Chemically bound water (also called non-evaporable), is chemically bound to cement particles and becomes part of the cement gel.

(2) Physically bound water (also called chemisorbed water) occupies the gel pores.

(3) Free water is water inside the capillary pores.

1) **Chemically bound water** or **Non-evaporable water**

Non-evaporable water is a constituent of the solid material in the paste [59]. This water may be removed at low relative humidity or at high temperatures. Taylor and co-workers [60] recommended drying at 11% RH to find chemically bound water which the interlayer water is part.

2) **Physically bound water** or **Gel water**

Powers and Brownyard [59] defined the gel water as the water contained in the pores of C-S-H gel. Gel water can be divided into: adsorbed and interlayer water.

3) **Capillary water or free water**

The sum of capillary water and gel water is termed evaporable water, which may be removed from the cement based materials using oven at 105 ºC [47]. According to Powers and Brownyard [59], capillary water is held in larger pores by capillary forces and it can be represent by desorption isotherm in equilibrium with RH of 40 to 100%.

h.1 Experimental study of the dynamics of water confined in hydrated cementitious materials

Very briefly, there are three main techniques to analyze the dynamics of water confined in hydrated cements:

a) Quasi-elastic neutron scattering (QENS).
b) Nuclear magnetic resonance techniques (NMR).
c) Broadband dielectric spectroscopy (BDS).

While the equipment and data analysis are rather complex in a) and b), dielectric spectroscopy is much simpler. In addition, BDS can access a very broad frequency and temperature range compared with a) and b). The weakness of dielectric spectroscopy is the absence of spatial resolution. However, following a correct strategy, the dielectric results can be related with the microstructure of the material analyzed.

All these techniques were used to analyze the dynamics of water in cementitious materials. We can mention the work of McDonald et al [61], Bohris et al [62], Korb et al [63] and Nonat [64] using NMR and the work of Bordallo [65,66], Zhang [67], Ridi et al [68,69] to analyze the dynamics of water through QENS.

In addition, and also to analyze the distribution of water molecules in these type of materials, several researchers [70–72] have studied the dielectric response of cement-based materials mainly in the high-frequency range (10^4–10^9 Hz) but also in the low frequency range (10^{-2}–10^6 Hz) at room temperatures or higher [73]. However, to our knowledge, dielectric studies at subzero temperatures are missing in the literature until the development of this thesis [74–76].

i. Aim of this study

This thesis aims to investigate the behavior of water molecules confined in cementitious material from an experimental point of view. Due to the complexity of the cement-water system, first we study the isolated C-S-H gel (the mayor binding phase that controls the chemistry and mechanics of cement). C-S-H gel is already a complex system with a broad distribution of the pores of different sizes. However, by means of dielectric experiments, we can access the dynamics of confined water molecules at supercooled temperatures. The dynamics of water in this system comprises different relaxations which spans a broad temperature and frequencies range. This is the first time to report the behavior of ultra-confined water at supercooled temperatures in cement like materials.

Additionally, we study the influence of adding nano-silica (SiO2) and aminopropyl (-(CH2)3-NH2,) functionalized silica nanoparticles during the synthesis of

C-S-H gel. The structural characteristics were studied by solid state 29Si NMR, ATR-FTIR, 13C NMR and XRD and XPS spectroscopy. In addition, the dynamics of water within the pores of C-S-H gel was analyzed by BDS. We observed that water confined in C-S-H formed with the addition of nanoparticles is faster than that in C-S-H gel which can be related to a different porous structure in these materials.

We also analyzed the dynamics of water confined in tobermorite because is a mineral used as a model system to describe microstructure of C-S-H gel. Water in tobermorite shows two different dynamics, the fastest process represents water molecules in Aluminium rich cavities; meanwhile the slow process represents the water in siliceous cavities.

At the end, we analyzed the OPC at different water-to-cement ratio and water content. It is a complex material, with large number of water dynamics due to its porous structure.

j. References

1. Hill, D. *A History of Engineering in Classical and Medieval Times*. **19,** 278 (Routledge, 2013).

2. Hewlett, P. *Lea's Chemistry of Cement and Concrete*. *Science* **58,** 1066 (2004).

3. Cement data. at <http://minerals.usgs.gov/minerals/pubs/commodity/cement/mcs-2015-cemen.pdf>

4. Mahasenan, N., Smith, S. and Humphreys, K. *Greenhouse Gas Control Technologies - 6th International Conference*. *Greenhouse Gas Control Technologies - 6th International Conference* **II,** 995–1000 (Elsevier, 2003).

5. Taylor, H. F. *Cement Chemistry:2nd edition*. *1990*

6. Mindess, S., Ska and Skalny, J. *Material Science of Concrete V*. 579 (1997).

7. Yurtdas, I., Peng, H., Burlion, N. and Skoczylas, F. Influences of water by cement ratio on mechanical properties of mortars submitted to drying. *Cem. Concr. Res.* **36,** 1286–1293 (2006).

8. Momma, K. and Izumi, F. VESTA 3 for three-dimensional visualization of crystal, volumetric and morphology data. *J. Appl. Crystallogr.* **44,** 1272–1276 (2011).

9. Stephan, D. and Wistuba, S. Crystal structure refinement and hydration behaviour of doped tricalcium aluminate. *Cem. Concr. Res.* **36,** 2011–2020 (2006).

10. Lee, F. C., Banda, H. M. and Glasser, F. P. Substitution of Na, Fe and Si in tricalcium aluminate and the polymorphism of solid solutions. *Cem. Concr. Res.* **12,** 237–246 (1982).

11. Aggarwal, P., Gard, J., Glasser, F. and Biggar, G. . Synthesis and properties of dicalcium aluminate, 2CaO.Aℓ2O3. *Cem. Concr. Res.* **2,** 291–297 (1972).

12. Colville, A. A. and Geller, S. The crystal structure of brownmillerite, Ca2FeAlO5. *Acta Crystallogr. Sect. B Struct. Crystallogr. Cryst. Chem.* **27,** 2311–2315 (1971).

13. Marinho, M. B. and Glasser, F. P. Polymorphism and phase changes in the ferrite phase of cements induced by titanium substitution. *Cem. Concr. Res.* **14,** 360–368 (1984).

14. Živica, V. Effects of the very low water/cement ratio. *Constr. Build. Mater.* **23,** 3579–3582 (2009).

15. Meade, R. K. A review of the american portland cement industry. *J. Am. Chem. Soc.* **28,** 1257–1264 (1906).

16. Humphrey, R. L. The inspection and testing of cements. *J. Franklin Inst.* **152,** 441–461 (1901).

17. Živica, V. Properties of blended sulfoaluminate belite cement. *Constr. Build. Mater.* **14,** 433–437 (2000).

18. Brown, P. W., Liberman, L. O. and Frohnsdorff, G. Kinetics of the Early Hydration of Tricalcium Aluminate in Solutions Containing Calcium Sulfate. *J. Am. Ceram. Soc.* **67,** 793–795 (1984).

19. Minard, H., Garrault, S., Regnaud, L. and Nonat, A. Mechanisms and parameters controlling the tricalcium aluminate reactivity in the presence of gypsum. *Cem. Concr. Res.* **37,** 1418–1426 (2007).

20. Kudowski, W. *Cement and Concrete Chemistry*. (2014).

21. Mehta, P. K. and Monteiro, P. J. M. *Concrete: structure, properties, and materials*. (1993).

22. Scrivener, K. L. Backscattered electron imaging of cementitious microstructures: understanding and quantification. *Cem. Concr. Compos.* **26,** 935–945 (2004).

23. Richardson, I. G. Tobermorite/jennite- and tobermorite/calcium hydroxide-based models for the structure of C-S-H: Applicability to hardened pastes of tricalcium silicate, β-dicalcium silicate, Portland cement, and blends of Portland cement with blast-furnace slag, metakao. *Cem. Concr. Res.* **34,** 1733–1777 (2004).

24. Jennings, H. M., Dalgleish, B. J. and Pratt, P. L. Morphological Development of Hydrating Tricalcium Silicate as Examined by Electron Microscopy Techniques. *J. Am. Ceram. Soc.* **64,** 567–572 (1981).

25. Richardson, I. G. and Cabrera, J. G. The nature of C-S-H in model slag-cements. *Cem. Concr. Compos.* **22,** 259–266 (2000).

26. Ylmén, R., Jäglid, U., Steenari, B. M. and Panas, I. Early hydration and setting of Portland cement monitored by IR, SEM and Vicat techniques. *Cem. Concr. Res.* **39,** 433–439 (2009).

27. Lachowski, E. E., Hong, S. Y. and Glasser, F. P. TEM image of synthetic C-S-H gel.

28. Regnault, O., Lagneau, V. and Schneider, H. Experimental measurement of portlandite carbonation kinetics with supercritical CO2. *Chem. Geol.* **265,** 113–121 (2009).

29. Henderson, D. M. and Gutowsky, H. S. A nuclear magnetic resonance determination of the hydrogen positions in Ca(OH)2. (1962).

30. Gaitero, J. J., Campillo, I., Guerrero, A. and J.J. Gaitero, I. Campillo, A. G. Reduction of the calcium leaching rate of cement paste by addition of silica nanoparticles. *Cem. Concr. Res.* **38,** 1112 (2008).

31. Porro, A., Dolado, J. S., Gaitero, J. J. and Manzano, H. Nanotechnology and Concrete. *Transp. Res. Rec. J. Transp. Res. Board* **2142,** 127–129 (2010).

32. Funk, A. and Trettin, H. F. R. DFT Study on the Effect of Water on the Carbonation of Portlandite. *Ind. Eng. Chem. Res.* **52,** 2168–2173 (2013).

33. Moore, A. and Taylor, H. F. W. Crystal Structure of Ettringite. *Nature* **218,** 1048–1049 (1968).

34. Taylor, H. F. W., Famy, C. and Scrivener, K. . Delayed ettringite formation. *Cem. Concr. Res.* **31,** 683–693 (2001).

35. Allmann, R. Refinement of the hybrid layer structure Ca2Al(OH)6 + 1 2 SO4 • 3H2O. *Neues Jahrb. fur Mineral. Monatshefte* 136–144 (1977).

36. Jennings, H. M., Thomas, J. J., Gevrenov, J. S., Constantinides, G. and Ulm, F. J. A multi-technique investigation of the nanoporosity of cement paste. *Cem. Concr. Res.* **37,** 329–336 (2007).

37. Ramachandran, V. S. and Beaudoin, J. J. *Handbook of analytical techniques in concrete science and technology*. (2001).

38. Taylor, H. F. W. Proposed Structure for Calcium Silicate Hydrate Gel. *J. Am. Ceram. Soc.* **69,** 464–467 (1986).

39. Richardson, I. G. and Groves, G. W. Models for the composition and structure of calcium silicate hydrate (C-S-H) gel in hardened tricalcium silicate pastes. *Cem. Concr. Res.* **22,** 1001–1010 (1992).

40. Deer, W. A., Howie, R. A. and Zussman, J. *Introduction to the Rock-Forming Minerals*. (2013).

41. Rodger, S. A. Microstructural development during hydration of cement. in *Material Research Society Symposium Proceedings* (1987).

42. Richardson, I. G. and Groves, G. W. The incorporation of minor and trace elements into calcium silicate hydrate (C-S-H) gel in hardened cement pastes. *Cem. Concr. Res.* **23,** 131–138 (1993).

43. Merlino, S., Bonaccorsi, E. and Armbruster, T. The real structure of tobermorite 11 angstrom: normal and anomalous forms, OD character and polytypic modifications. *Eur. J. Mineral.* **13,** 577–590 (2001).

44. Bonaccorsi, E., Merlino, S. and Kampf, A. R. The crystal structure of tobermorite 14A?? (plombierite), a C-S-H phase. *J. Am. Ceram. Soc.* **88,** 505–512 (2005).

45. Carpenter, a. B., Chalmers, R. a., Gard, J. a., Speakman, K. & Taylor, H. F. W. Jennite, a new mineral. *Am. Mineral.* **51,** 56–74 (1966).

46. Bonaccorsi, E., Merlino, S. and Taylor, H. F. W. The crystal structure of jennite, Ca9Si6O18(OH)6·8H2O. *Cem. Concr. Res.* **34,** 1481–1488 (2004).

47. T. C. Powers and T. I. Brownyard. *Studies of the physical properties of hardened Portland cement paste*. (1958).

48. R. F. Feldman and P. J.Sereda. A new model for hydrated portland cement and its practical implications. *Eng. J. Canada* 53, 53 (1970).

49. Thomas, J. J. and Jennings, H. M. A colloidal interpretation of chemical aging of the C-S-H gel and its effects on the properties of cement paste. *Cem. Concr. Res.* **36,** 30–38 (2006).

50. McDonald, P. J., Rodin, V. and Valori, A. Characterisation of intra- and inter-C–S–H gel pore water in white cement based on an analysis of NMR signal amplitudes as a function of water content. *Cem. Concr. Res.* **40,** 1656–1663 (2010).

51. Powers, T. C. and Brownyard, T. I. No Title. *J. Am. Concr. Inst.* **43,** 101, 249, 469, 669, 845, 865, 933, 971 (1947).

52. Dolado, J. S., Griebel, M., Hamaekers, J. and Heber, F. The nano-branched structure of cementitious calcium–silicate–hydrate gel. *J. Mater. Chem.* **21,** 4445 (2011).

53. Mindess, S. and Young, J. F. *Concrete*. 671 (1981).

54. Monteiro, P. J. M. and Mehta, P. *Concrete: Microstructure, properties and materials*. (2006).

55. Science of concrete. http://iti.northwestern.edu/cement/index.html.

56. Powers, T. C. *Resistance of concrete to freezing and thawing*.

57. Thomas, J. J., Jennings, H. M. and Allen, A. J. The Surface Area of Hardened Cement Paste as Measured by Various Techniques. *Cem. Concr. Res.* **28,** 897–905 (1998).

58. Sereda, P. J., Feldman, R. F. and Ramachandra, V. S. Proceeding of the seventh international congress on chemistry of cement. in *Proceeding of the seventh international congress on chemistry of cement* (1980).

59. C. Powers and T. I. Brownyard. Proc. am. concrete inst. 43, 971–992 (1947). *Proc. am. Concr. inst.* 43, 971–992 (1947).

60. Taylor, H. F. W. and Turner, A. B. Reactions of tricalcium silicate paste with organic liquids. *Cem. Concr. Res.* **17,** 613–623 (1987).

61. McDonald, P. J., Korb, J.-P., Mitchell, J. and Monteilhet, L. Surface relaxation and chemical exchange in hydrating cement pastes: a two-dimensional NMR relaxation study. *Phys. Rev. E. Stat. Nonlin. Soft Matter Phys.* **72,** 011409 (2005).

62. Bohris, A. J. *et al.* A broad line NMR and MRI study of water and water transport in portland cement pastes. *Magn. Reson. Imaging* **16,** 455–461 (1998).

63. Korb, J.-P., McDonald, P. J., Monteilhet, L., Kalinichev, A. G. and Kirkpatrick, R. J. Comparison of proton field-cycling relaxometry and molecular dynamics simulations for proton–water surface dynamics in cement-based materials. *Cem. Concr. Res.* **37,** 348–350 (2007).

64. Colombet, P., Grimmer, A.-R., Zanni, H. and Sozzani, P. *Nuclear magnetic resonance spectroscopy of cement-based materials*. (1998).

65. Bordallo, H. N., Aldridge, L. P. and Desmedt, A. Water dynamics in hardened ordinary portland cement paste or concrete: From quasielastic neutron scattering. *J. Phys. Chem. B* **110,** 17966–17976 (2006).

66. Jacobsen, J. *et al.* Nano-scale hydrogen-bond network improves the durability of greener cements. *Sci. Rep.* **3,** 2667 (2013).

67. Zhang, Y. *et al.* Observation of dynamic crossover and dynamic heterogeneity in hydration water confined in aged cement paste. *J. Phys. Condens. Matter* **20,** 502101 (2008).

68. Ridi, F., Luciani, P., Fratini, E. and Baglioni, P. Water confined in cement pastes as a probe of cement microstructure evolution water confined in cement pastes as a probe of cement microstructure evolution. *J. Phys. Chem. B* **113,** 3080–7 (2009).

69. Ridi, F., Fratini, E. and Baglioni, P. Cement: a two thousand year old nano-colloid. *J. Colloid Interface Sci.* **357,** 255–64 (2011).

70. Hager, N. E. and Domszy, R. C. Monitoring of cement hydration by broadband time-domain-reflectometry dielectric spectroscopy. *J. Appl. Phys.* **96,** 5117 (2004).

71. Miura, N., Shinyashiki, N., Yagihara, S. and Shiotsubo, M. Microwave Dielectric Study of Water Structure in the Hydration Process of Cement Paste. *J. Am. Ceram. Soc.* **81,** 213–216 (2005).

72. Yagihara, S. *et al.* Microwave Dielectric Study on Water Structure and Physical Properties of Aqueous Systems Using Time Domain Reflectometry with Flat-End Cells. *Subsurf. Sens. Technol. Appl.* **2,** 15–30

73. Tsonos, C. *et al.* Probing the microstructure of cement mortars through dielectric parameters' variation. *J. Phys. Chem. Solids* **70,** 576–583 (2009).

74. Cerveny, S., Arrese-Igor, S.,Dolado, J. S., Gaitero, J. J., Alegría, A., Colmenero, J, Effect of hydration on the dielectric properties of C-S-H gel. *J. Chem. Phys.* **134,** 034509 (2011).

75. Monasterio, M., Jansson, H., Gaitero, J. J., Dolado, J. S. & Cerveny, S. Cause of the fragile-to-strong transition observed in water confined in C-S-H gel. *J. Chem. Phys.* **139,** (2013).

76. Monasterio, M., Gaitero, J. J., Erkizia, E., Guerrero, A., Miccio, L. A., Dolado, J S. Cerveny, S., Effect of addition of silica- and amine functionalized silica-nanoparticles on the microstructure of C-S-H gel. *J. Colloid Interface Sci.*

Chapter II

The Water molecule

a. Introduction

Water is the major constituent of the living organism. Water makes up 70 -80 % of all organisms and life is impossible without it. Cell biologists have come to recognize the importance of water for living organization and function [1]. In addition, abundance of water on the earth makes it involved in the processes involved in various fields of science and technology [2]. Most of water on the earth is in the bulk phase: crystalline form in glaciers and polar caps, liquid phase in the oceans and vapor in the air. In addition, part of water on the earth is affected by the presence of different boundaries, borders or restrictions. This water is usually called *interfacial water* and this is the type of water we are interested in this thesis. Sometimes in nature, water molecules are located in small nanometer sized cavities and in this case water is normally called *confined water*.

Water differs from most other liquids with respect to many physical properties. The anomalous properties of water are those where the behavior of liquid water is quite different from what is found with other liquids [3]. Frozen water (ice) also shows anomalies when compared with other solids. In the literature, there are several reviews where all the water anomalies are explained in detail [4]

b. Inside the water molecule

Water molecules (H_2O) are made up of two hydrogen atoms bonded to one oxygen atom (Figure II.1 (a)). Because of the way in which oxygen and hydrogen atoms are bonded, the area near the oxygen has a slight negative charge and the areas near the hydrogen have a slight positive charge. The positive and negative areas of the water molecule cause it to be attracted to other water molecules. Notice that the oxygen from one water molecule is attracted to the hydrogen from another and vice versa. This

allows water molecules to form associations with other water molecules in several directions at the same time. This interaction is known as hydrogen bonding.

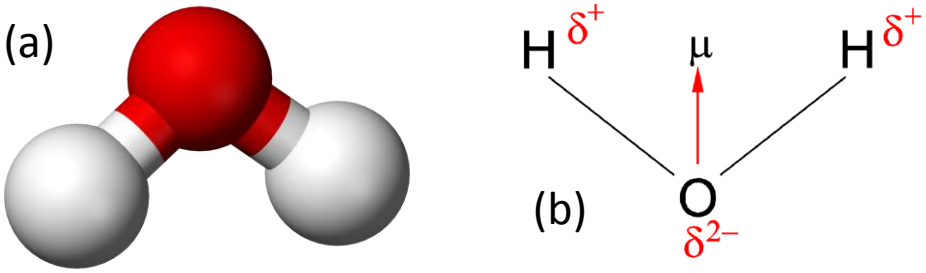

Figure II.1. (a) The water molecule. (b) Dipole moment of water.

As above mentioned, oxygen in the water molecule attracts electrons much more strongly than hydrogen, resulting in a net positive charge on the hydrogen atoms, and a net negative charge on the oxygen atom. The presence of a charge on each of these atoms gives each water molecule a net dipole moment (see Figure II.1 (b)). The molecules of water are constantly moving in relation to each other, and the hydrogen bonds are continually breaking and reforming at timescales faster than 200 femtoseconds [5].

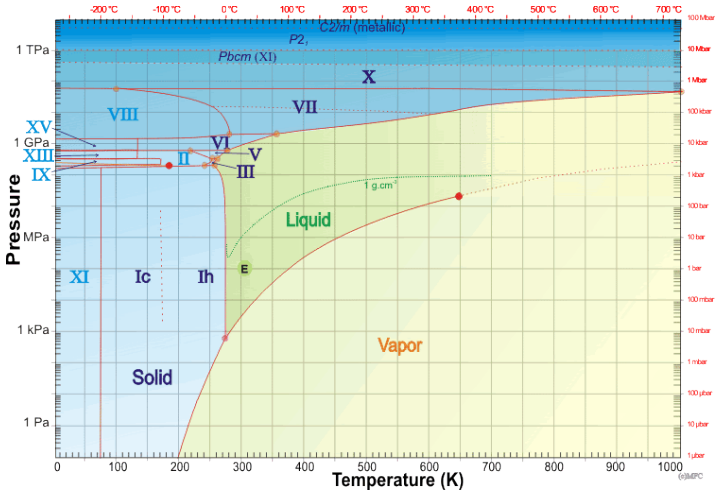

Figure II.2. Phase diagram of water. Liquid, Vapor and the eleven different types of ice can be seen in the figure.

The phase diagram of the water is complex (see Figure II.2), having a number of triple and critical points. Phase diagram of bulk water describes how the phase state of water changes with temperatures and pressure. This includes the liquid-vapor, liquid-

solid and solid-solid phase transitions and also the hypothesized transitions between amorphous (glassy or liquid) phases of supercooled water. In the solid state water form more than 15 crystalline forms where the hexagonal ice is the most abundant. At 273.15 K water freezes into hexagonal ice.

c. Supercooled water

Super-cooling is the process of lowering the temperature of a liquid or a gas below its freezing point without it becoming a solid. Bulk water become a solid at 273.25 K However, applying fast cooling rates (~ 10^5 K/min), water can be supercooled up to about T_N = -42 ^oC (231.15 K). This is the nucleation temperature (T_N) below which water becomes inevitably ice. This is a very particular temperature, usually called the starting point of the "no man´s land" [6]. Near of this range, water crystallizes into ice so rapidly that it can be difficult to observe the molecules that remain in liquid form. In addition, by fast rate of cooling or by compressing ordinary ice at low temperatures, very pure liquid water can be cooled (supercooled) below its glass transition temperature (T_g, a value still discussed in the literature [4,7]) in milliseconds to prevent the spontaneous nucleation of crystals. Amorphous ice is distinguished of regular ice by a lack of long-range order in its molecular arrangement. Different types of amorphous water can be formed called "hyperquenched glassy water" (HGW) or amorphous solid water (ASW). These glasses have a thermodynamic similarity with liquid water as well as some structural alike, due to their methods of formations and amorphous properties. However, amorphous water also crystallizes on heating at about 150 K.

Thus, between 150 and 231 K there is no bulk liquid water as crystallization exist. These two temperatures define a temperature region called "no man´s land" in the sense that water cannot be liquid. Figure II.3 schematically shows the temperature regions discussed above.

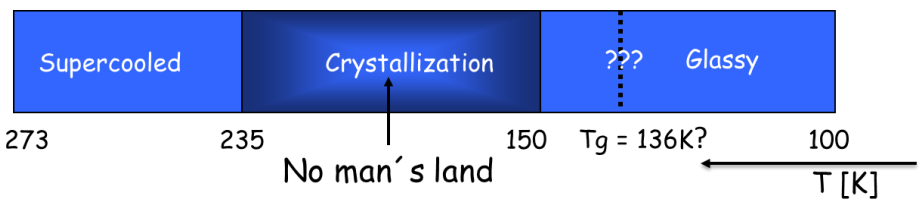

Figure II.3. This chart shows water's phases at different temperatures. Temperature is displayed in Kelvin.

In the 1970s, Speedy and Angell suggested that the existence of a second critical point at ~220 K that could explain many of the anomalous properties of water. Unfortunately, this second critical point is difficult to study as it lies below the homogeneous nucleation temperature. Figure II.4 shows the water phase diagram at low temperatures where this second critical point is displayed. There are several discursion in the literature regarding the experimental verification of this hypothesis [8–10]. Until now, there is no a clear experimental report which indefinitely indicates the existence of this 2nd critical point.

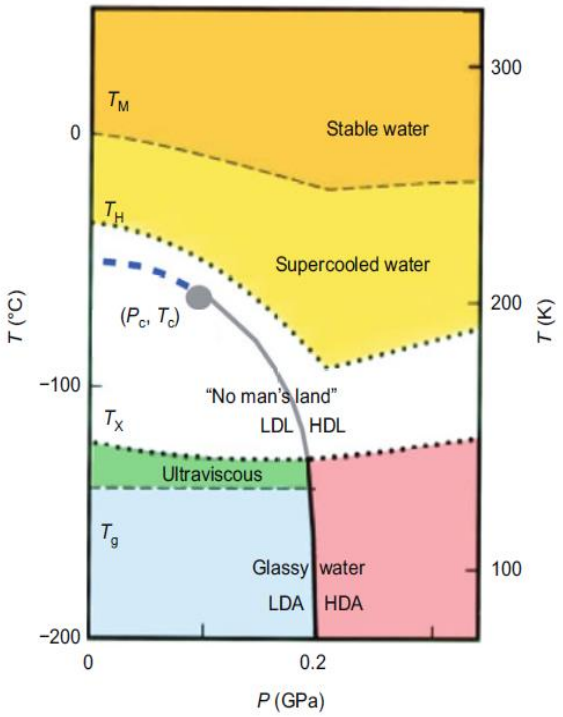

Figure II.4. This chart shows water's various phases at different temperatures and pressures. Figure taken from reference [11].

d. Confined water – Dynamical behavior

When water molecules are trapped in the pore geometry of another material, we refer this situation as *confined water*. In this case, the phase diagram differs from the bulk one. Bulk phase transitions and surface transitions are modified due to the confinement in pores.

Almost all water in our bodies can be considered as confined or interfacial, since most of these water molecules are never more than about 5Å from other types of molecules, such as proteins, lipids and many other types of biomolecules [1]. In addition, certain amount of confined water may be expected in comets, which presumably represent a mixture of dust and ice. Furthermore, such interfacial water plays a major role in geology and in the type of materials analyzed in this thesis. It is therefore not surprising that the structural and dynamical properties of water in different types of environments have been extensively studied over several decades.

Rigid porous materials can be categorized according to the degree of hydrophilicity or hydrophobicity, the topology of the network (order/disorder) and their pore diameter d (micro d < 20 Å, meso 20 Å < d < 500 Å and macro d > 500 Å). Water has been confined in disordered porous materials such as mineral clays [12], cement like materials [13–15], silica hydrogels [16], molecular sieves [17] and graphite oxide [18]. These materials are hydrophilic and display an interconnected pore structure with a broad pore size distribution and therefore give rise to an incomplete filling of the pores and water-surface interactions are therefore promoted. These characteristics are the source of changes in the dynamical behavior of the confined water. However, when water is confined in more regular systems such MCM-41 [19], the water dynamics is less influenced by the surface interactions, and a more 'universal' relaxation behavior is obtained [4].

Figure II.5 compares the main relaxation of water confined in different confinement types (with sizes between 10 and 21 Å and well-defined geometry) as well as in some water solutions (at very high water concentrations, before crystallization occurs). Considering only these systems, it is evident that the relaxation time of water in both hard and soft confinement systems has the same time scale and the same activation energy at low temperatures, even if the nature of the confinement is different. This relaxation is the so called universal β-relaxation of water [4], and it can only be observed at very high water concentrations for soft confinements and for well-defined geometries (T>200K) with 'smooth' surfaces in hard confinements. At high temperatures surface or solute interactions dominate and the differences between the two types of systems are generally larger. In hard confinement systems with rough surfaces, the water relaxation becomes systematically faster than this universal

relaxation. The causes of this acceleration are not fully clear but it can be explained if the water forms small clusters of imperfect tetrahedral networks, rather than an extended hydrogen-bonded network.

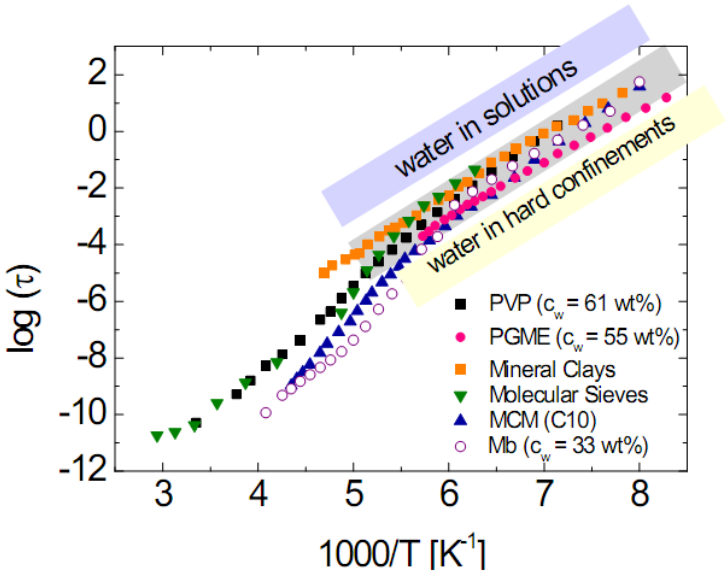

Figure II.5. Temperature dependence of the relaxation time in some confinement systems (hard-confinements): mineral clays [12], molecular sieves [17], MCM-41[19], silica hydrogel [16], graphite oxide (GO) [18], white cement [15] AND C-S-H gel [13,14] and soft confinements: PVP [20] and PGME [21].

Commonly, the high-temperature dynamics of the interfacial water is strongly dependent on the porous host material, but below the crossover temperature both the activation energy and the relaxation time of the water relaxation is almost independent of the system.

The relaxation time of water confined in all the materials above mentioned shows an Arrhenius behavior at low temperatures (170 to 200 K) with common activation energy of 0.5 eV [16]. At higher temperatures, a dynamic crossover from high-temperature non-Arrhenius dependence to a low-temperature Arrhenius behavior is normally observed.

It is not clear why this crossover occurs, but it could be related with finite-size effects. Following the Adam-Gibbs theory [22], the size of the cooperative rearranging regions associated with the α-relaxation increases when the temperature decreases. When it reaches a certain size, in function of the confinement, these α-like cooperative

motions can no longer occur and only the intrinsic β-relaxation remains. When the confinement is sufficiently severe, the same phenomenon will occur for all liquids [23], but the anomaly for water is that it seems to occur even for relatively moderate confinements of sizes considerably larger than the size of a few water molecules. Nevertheless, due to the strong network character of water at low temperatures, it is possible that the cooperative rearranging regions associated with the α-relaxation grow rapidly with the decreasing of the temperature and soon become larger than the size of the confinement. Although this interpretation cannot be fully proven it seems to be a good explanation for why the α-relaxation cannot be observed below the crossover temperature and for the almost system independent time scale and activation energy of the low-temperature water relaxation. It also explains why confined water does not exhibit any clear calorimetric T_g [24–26] since T_g corresponds to the temperature for which the structural α-relaxation time reaches a time scale in the order of 100 s, and this time scale is never reached due to the confinement-induced vanishing of the α-relaxation. Thus, although the proposed explanation for the dynamic crossover cannot be proven, it is consistent with all available experimental findings. It is worth to mention then rather interpretations of this crossover were proposed in the literature. Most QENS studies of supercooled water in both hard confinements and on protein surfaces have indicated that there is a dynamic crossover at about 225K [8,27], although it has been argued that this crossover is due to an incorrect data analysis at the limit of the experimental energy resolution [28].

e. References

1. Middendorf, H. D. Neutron studies of the dynamics of biological water. *Phys. B Condens. Matter* **226,** 113–127 (1996).

2. Schlapbach, L. and Züttel, A. Hydrogen-storage materials for mobile applications. *Nature* **414,** 353–8 (2001).

3. Ball, P. Water as an active constituent in cell biology. *Chem. Rev.* **108,** 74–108 (2008).

4. Swenson, J. and Cerveny, S. Dynamics of deeply supercooled interfacial water. *J. Phys. Condens. Matter* **033102,** 33102 (2015).

5. Smith, J. D. *et al.* Unified description of temperature-dependent hydrogen-bond rearrangements in liquid water. *Proc. Natl. Acad. Sci. U. S. A.* **102,** 14171–14174 (2005).

6. Phrase of the Week: No-Man's Land | SLAC Today. at <https://news.slac.stanford.edu/features/phrase-week-no-mans-land>

7. Johari, G. P. State of water at 136 K determined by its relaxation time. *Phys. Chem. Chem. Phys.* **7,** 1091–5 (2005).

8. Liu, L., Chen, S.-H., Faraone, A., Yen, C.-W. and Mou, C.-Y. Pressure Dependence of Fragile-to-Strong Transition and a Possible Second Critical Point in Supercooled Confined Water. *Phys. Rev. Lett.* **95,** 117802 (2005).

9. Swenson, J. Comment on "Pressure dependence of fragile-to-strong transition and a possible second critical point in supercooled confined water". *Phys. Rev. Lett.* **97,** 189801; discussion 189803 (2006).

10. Cerveny, S., Colmenero, J. and Alegría, A. Comment on "Pressure Dependence of Fragile-to-Strong Transition and a Possible Second Critical Point in Supercooled Confined Water." *Phys. Rev. Lett.* **97,** 189802 (2006).

11. Sun, Z., Sun, G., Chen, Y. and Xu, L. Liquid-liquid phase transition in water. *Sci. China Physics, Mech. Astron.* **57,** 810–818 (2014).

12. Bergman, R. and Swenson, J. Dynamics of supercooled water in confined geometry. *Nature* **403,** 283–6 (2000).

13. Cerveny, S., Arrese-Igor, S.,Dolado, J. S., Gaitero, J. J., Alegría, A., Colmenero J., Effect of hydration on the dielectric properties of C-S-H gel. *J. Chem. Phys.* **134,** 034509 (2011).

14. Monasterio, M., Jansson, H., Gaitero, J. J., Dolado, J. S. and Cerveny, S. Cause of the fragile-to-strong transition observed in water confined in C-S-H gel. *J. Chem. Phys.* **139,** (2013).

15. Zhang, Y. *et al.* Observation of dynamic crossover and dynamic heterogeneity in hydration water confined in aged cement paste. *J. Phys. Condens. Matter* **20,** 502101 (2008).

16. Cammarata, M. *et al.* Structure and dynamics of water confined in silica hydrogels: X-ray scattering and dielectric spectroscopy studies. *Eur. Phys. J. E. Soft Matter* **12 Suppl 1,** S63–6 (2003).

17. Jansson, H. and Swenson, J. Dynamics of water in molecular sieves by dielectric spectroscopy. *Eur. Phys. J. E. Soft Matter* **12 Suppl 1,** S51–4 (2003).

18. Cerveny, S., Barroso-Bujans, F., Alegría, Á. and Colmenero, J. Dynamics of Water Intercalated in Graphite Oxide. *J. Phys. Chem. C* **114,** 2604–2612 (2010).

19. Sjöström, J., Swenson, J., Bergman, R. and Kittaka, S. Investigating hydration dependence of dynamics of confined water: monolayer, hydration water and Maxwell-Wagner processes. *J. Chem. Phys.* **128,** 154503 (2008).

20. Cerveny, S., Alegría, Á. and Colmenero, J. Broadband dielectric investigation on poly(vinyl pyrrolidone) and its water mixtures. *J. Chem. Phys.* **128,** 044901 (2008).

21. Sjöström, J. *et al.* Dielectric secondary relaxation of water in aqueous binary glass-formers. *Phys. Chem. Chem. Phys.* **12,** 10452–6 (2010).

22. Adam, G. and Gibbs, J. H. On the Temperature Dependence of Cooperative Relaxation Properties in Glass-Forming Liquids. *J. Chem. Phys.* **43,** 139 (1965).

23. Swenson, J., Jansson, H. and Bergman, R. Relaxation Processes in Supercooled Confined Water and Implications for Protein Dynamics. *Phys. Rev. Lett.* **96,** 247802 (2006).

24. Swenson, J., Elamin, K., Jansson, H. and Kittaka, S. Why is there no clear glass transition of confined water? *Chem. Phys.* **424,** 20–25 (2013).

25. Elamin, K., Jansson, H., Kittaka, S. and Swenson, J. Different behavior of water in confined solutions of high and low solute concentrations. *Phys. Chem. Chem. Phys.* **15,** 18437–44 (2013).

26. Swenson, J., Jansson, H., Hedström, J. and Bergman, R. Properties of hydration water and its role in protein dynamics. *J. Phys. Condens. Matter* **19,** 205109 (2007).

27. Faraone, A., Liu, L., Mou, C.-Y., Yen, C.-W. and Chen, S.-H. Fragile-to-strong liquid transition in deeply supercooled confined water. *J. Chem. Phys.* **121,** 10843–6 (2004).

28. Doster, W. *et al.* Dynamical Transition of Protein-Hydration Water. *Phys. Rev. Lett.* **104,** 098101 (2010).

Chapter III

Experimental Techniques and Samples

The present section covers the experimental investigation of the project. First, an overview of the experimental techniques is given (Section a). Then, the characteristics (e.g. chemical and physical properties) of the materials used in this thesis are described (Section b).

a. Experimental Techniques

a.1 Differential Scanning Calorimetry (DSC)

Differential scanning calorimetry is a technique that allows the study of different thermal transitions in materials. DSC quantifies the heat associated with these thermal transitions, induced in a controlled atmosphere by temperature changes (usually N_2). The heat flow can be written as

$$\frac{dH}{dt} = c_p \frac{dT}{dt} + f(T, t) \qquad \text{(III.1)}$$

where $\frac{dH}{dt}$ is the DSC heat flow signal, c_p is the heat capacity, $\frac{dT}{dt}$ is the heating rate and $f(T, t)$ is the time dependent heat flow at an absolute temperature [1].

In this thesis, the calorimetric measurements (DSC) were performed using a Q2000 TA Instruments to determine thermal events on all the samples (see Figure III.1). DSC measurements were normally performed using a cooling–heating cycle between 140 K and 300 K, at a rate of 10 K/min.

Figure III.1. DSC Q 2000 from TA Instruments employed for the calorimetric measurements.

a.2 Thermogravimetric Analysis (TGA)

Thermogravimetric analysis is based on the measurement of the sample mass as a function of temperature. The detection is performed through a microbalance, in a controlled atmospheric furnace. In this way, this technique is sensitive to any mass changes in the sample, therefore rendering information of decomposition, oxidation, and evaporation or desorption processes.

In this thesis, the thermogravimetry analysis (TGA) was performed using a TA Instruments Q500 thermogravimetric analyzer (see Figure III.2). Samples were heated from room temperature to 800 °C with a ramp rate of 5 °C/min under a constant N_2 flow of 25 mL/min.

Figure III.2. Q500 thermogravimetric analyzer by TA Instruments employed for the TGA measurements.

a.3 Fourier Transform Infrared Spectroscopy (FT-IR)

In infrared spectroscopy, IR radiation is passed through a sample. Some part of the infrared radiation is absorbed by the sample and another part passed through (transmitted). The resulting spectrum represents the molecular absorption and transmission, creating a molecular fingerprint of the sample. No two unique molecular structures produce the same infrared spectrum. This makes infrared spectroscopy useful for several types of analysis. The infrared portion of the electromagnetic spectrum is usually divided into three regions: a) Near (4000-14000 cm^{-1}), b) Mid (400-4000 cm^{-1}) and c) Far (10-400 cm^{-1}).

FTIR was used in addition with an attenuated total reflectance (ATR) stage. ATR generally allows qualitative or quantitative analysis of samples with little or no sample preparation. The main benefit of ATR sampling comes from the very thin sampling path length and depth of penetration of the IR beam into the sample. This measure way is different in comparison with traditional FT-IR sampling by transmission where the sample must be diluted with IR transparent salt, pressed into a pellet or pressed to a thin film, prior to analysis to prevent totally absorbing bands in the infrared spectrum.

In this thesis, the infrared spectra were measured at room temperature over the range 600−4000 cm^{-1} using a JASCO 6500 spectrometer which was equipped with an attenuated-total-reflectance unit (ATR) (see Figure III.3). Each spectrum was collected with a resolution of 4 cm^{-1} and an average of 200 repetitive scans. The spectra were corrected for the base line using the software Spectra Analysis from Jasco and no smoothing of the data was performed.

Figure III.3. FT-IR spectrometer 6500 by Jasco employed for FTIR experiments.

a.4 Broadband Dielectric Spectroscopy (BDS)

The basis of dielectric relaxation spectroscopy as a tool to investigate molecular dynamics is the 'Fluctuation-Dissipation Theorem', which states that when a weak perturbation is applied to a system in thermodynamic equilibrium, its response reflects the internal fluctuations without perturbation [2–4]. In our case, we will study the dynamics of water in hard confinement systems by means of this relaxation technique. For that, we will measure the dielectric properties of a medium as a function of frequency at constant temperature. This allows us to extract information about both the dynamics (relaxation time) and interactions (via the permittivity values) of our systems.

BDS is a technique used to study the polarization mechanisms in several materials caused either, (i) due to charge migration, or (ii) due to the orientation of permanent dipoles. When materials containing permanent dipoles are placed in an alternating (sinusoidal) external electric field, dipole orientation takes place due to the alignment of dipoles in the direction of the applied electric field. At high frequencies of the applied field, molecular dipoles fail to follow the variations in the direction of the external field and the measured dielectric permittivity will be determined by induced atomic and electronic polarization. However, as the frequency decreases the molecular dipoles will try to orient in the direction of the applied electric field. Further decrease in the frequency of the applied field increases the degree of orientation of molecular dipoles, which in turn increase the dielectric permittivity. At low enough frequencies, molecular dipoles follow the alternating electric field and a plateau of the dielectric permittivity (static value) is observed. This behavior is shown in Figure III.4.

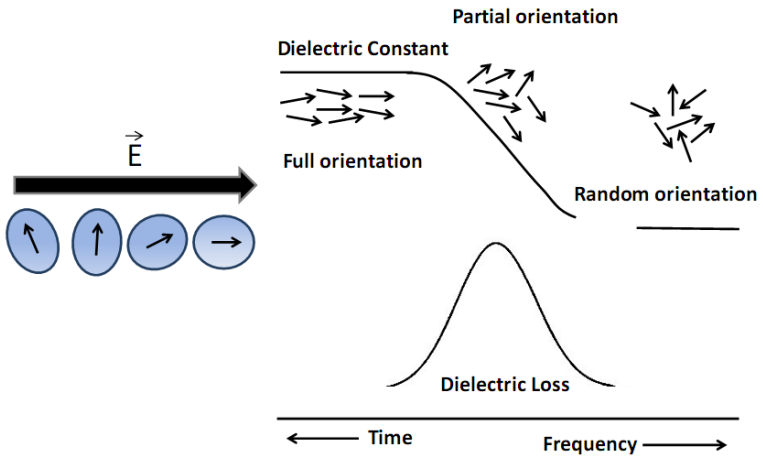

Figure III.4 Scheme of the behavior shown by dipoles when an external electric field is applied.

In a BDS experiment, the sample under study is placed between two parallel disk-shaped electrodes and the capacitance is described by

$$c = \varepsilon \cdot \varepsilon_o \frac{S}{d} \tag{III.2}$$

where c is the capacity, ε is the relative dielectric permittivity of the sample, ε_o the permittivity in the vacuum, S is the area of the electrodes and d the distance between them. By considering a sinusoidal excitation, equation (III.2) can be rewritten

$$C^*(\omega) = \varepsilon^*(\omega) \cdot \varepsilon_o \frac{S}{d} \tag{III.3}$$

where $\omega = 2\pi f$. The complex permittivity can in turn be written as

$$\varepsilon^*(\omega) = \varepsilon'(\omega) - i\varepsilon''(\omega) = C^*(\omega) \cdot \frac{d}{\varepsilon_0 S} \tag{III.4}$$

being c_o the empty capacity.

On the other hand, the voltage and intensity of a sinusoidal function are

$$V(t) = V_{max} \cos(\omega t) \rightarrow V^* = V_{max} \tag{III.5}$$

$$I(t) = I_{max} \cos(\omega t - \delta) \rightarrow I^* = I_{max} \cos\delta - iI_{max} \sin\delta \tag{III.6}$$

being $\delta = \omega\Delta t$.

The impedance (Z^*) in a function of the resistance (R_S) and the capacitor (C_S) is

$$Z^*(\omega) = \frac{V^*(\omega)}{I^*(\omega)} = \frac{V_o e^{i\omega t}}{I_o e^{i\omega t + \delta}} \tag{III.7}$$

we can recover equation (III.4), and write (III.7) as

$$C^*(\omega) = -i \frac{I^*(\omega)}{V^*(\omega)} \tag{III.8}$$

therefore, just measuring the current and the voltage we can obtain the capacity (eq. III.7) and the permittivity using the equation (III.4)

a.4.1 Phenomenological models of dielectric relaxation

The Debye equation [5] represents the simplest problem of polarization. It is assumed that the decrease of the polarization in the absence of an external electric field is directly proportional to the polarization itself. In the Debye model, the permittivity is

$$\varepsilon * (\omega) = \varepsilon'(\omega) - i\varepsilon''(\omega) = \varepsilon_{\infty} + \frac{\Delta\varepsilon}{1 + i\omega\tau} \qquad \text{(III.9)} \quad \text{(I.1)}$$

where $\Delta\varepsilon = (\varepsilon_s - \varepsilon_\infty)$ is the *dielectric relaxation amplitude* (or dielectric strength) and τ is the *Debye- relaxation time*, a single time constant that would describe the dynamics of the system. ε' is the real part of the complex dielectric permittivity and refers to the stored energy in the system, ε'' is the imaginary part and is proportional to the dissipated energy. ε_s is the low frequency permittivity and ε_∞ the high frequency permittivity.

The Debye model fails for describing the relaxation behavior of many materials (and this is enhanced at low temperatures), which present a significantly broader loss peak. In these cases, the dynamics is somewhat 'spread', and it is characterized by a distribution of relaxation times, rather than by a single time. There are several different approaches for accounting for non-Debye behavior. We considered here empirical extensions of the Debye equation such as de Cole-Cole or Havriliak-Negammi equations

Cole – Cole equation

The Cole-Cole equation (CC) models a symmetrically-broadened loss curve (ε´´) and can be described by the formula [6]

$$\varepsilon * (\omega) = \varepsilon_{\infty} + \frac{\Delta\varepsilon}{[1+(i\omega\tau)^{\alpha}]} \qquad \text{(III.10)}$$

the α-parameter describes a symmetric relaxation time distribution around the so-called Cole-Cole relaxation time, τ, which gives the position of maximal loss.

Havriliak-Negammi equation

For representing broadened and asymmetrically shaped dispersion and loss curves, we consider the Havriliak-Negami (HN) equation

$$\varepsilon * (\omega) = \varepsilon_{\infty} + \frac{\Delta\varepsilon}{[1+(i\omega\tau_{HN})^{\alpha}]^{\gamma}} \quad \text{(III.11)}$$

where α and γ represent the shape of the dielectric spectra. α accounts for the broadening of the spectra, and γ, for the skewing of the spectra at high frequency.

a.4.2 Relaxation times

The mobility of dipoles depends on the local constraints experienced from their immediate surroundings. Local variations of these constraints results in the distribution of relaxation times. These relaxation time distributions present a characteristic time, at which, the dipolar relaxation reaches its maximum

$$\tau_{max} = \frac{1}{2\pi f_{max}} \quad \text{(III.12)}$$

where f_{max} corresponds with the frequency at the maximum loss.

Arrhenius equation

The Arrhenius equation, originally introduced to describe the variation of the rate constant of a chemical reaction with temperature, represents a widely used way for describing the temperature dependence of relaxation times

$$\tau(T) = \tau_o \exp\left(\frac{E_a}{kT}\right) \quad \text{(III.13)}$$

where E_a is the *activation energy* related to rotational barriers, k is the Boltzmann's constant, and τ_o is related to a molecular vibration time. This approach is based on the

idea that particles are pushed by thermal fluctuations to make transitions between two energetic levels, where an energy barrier E_a must be overcome.

Vogel-Fulcher-Tamman equation

Glass-forming liquids are often characterized by nonlinearity in the ln τ = f(1/T) behavior, which can be described via the Vogel-Fulcher-Tamman (VFT) equation [7]

$$\tau_\alpha = \tau_o \exp\left(\frac{B}{T - T_o}\right) \qquad \text{(III.14)}$$

where τ_o can be understood as the reciprocal of a 'transition-attempt frequency', B is a temperature factor and T_0 is the so-called VFT-temperature, which is usually found at several tens below the glass-transition temperature T_g.

α- and β- relaxation processes

In glass-forming systems, the so-called α- and β- relaxation processes can be distinguished. The α-relaxation is a cooperative process involving segmental motions, thus subjected to interactions of both intra- and intermolecular nature. Its temperature dependence is usually described by the VFT law, Eq. (III.14)

On the other hand, many systems exhibit localized secondary relaxations, known as β-relaxations, which are attributed to localized rotational fluctuations of the dipole vector (local conformational rearrangements). In this case, the temperature dependence is usually well described by an Arrhenius law.

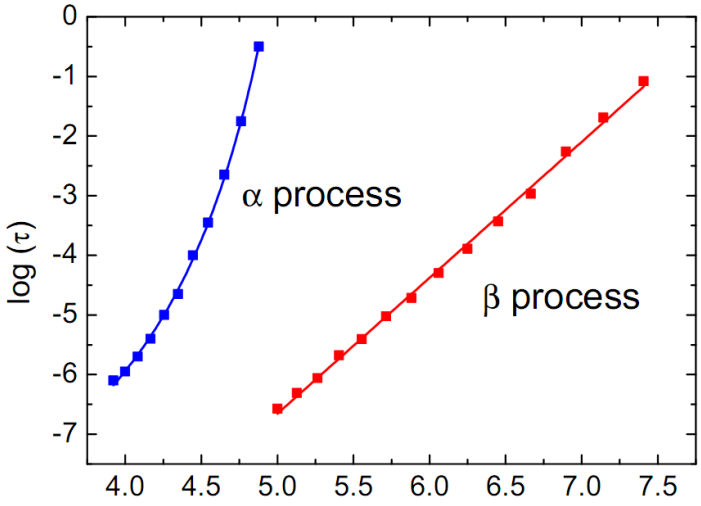

Figure III.5 Relaxation times against the inverse of the temperature. Comparison of the temperature dependence for α- (VFT) and β- processes (Arrhenius).

The explained features are implemented in the Novocontrol Alpha analyzer system, which is the device used for the study of water in cementitious materials. The measured temperature range was 110 – 250 K, and the frequency range 10^{-2} Hz – 10^{6} Hz, where the relevant relaxations appear at low temperatures. The samples were placed between parallel gold-plated electrodes, with a diameter of 20 mm and were typically 0.4 mm thick. After fast cooling (rate > 20 K/min), the isothermal frequency scans recording $\varepsilon^*(\omega)$ were performed every 5^{o} over a temperature range of 100-250 K.

Figure III.6. *Left*: general perspective of the Novocontrol Alpha analyzer and the temperature control. *Right:* sample cell. The sample is placed between parallel gold-plated electrodes.

a.5 Scanning Electron Microscopy (SEM)

SEM renders images of the sample surface by probing the specimen with a focused electron beam that is scanned across a rectangular area. Due to the interaction with the sample, the electron beam loses energy by a variety of mechanisms. This energy is in turn converted into alternative forms such as heat, emission of low-energy secondary electrons and high-energy backscattered electrons, light emission (cathodoluminescence) or X-ray emission, which provide signals carrying information about the properties of the specimen, such as its topography and composition. Therefore, SEM maps the intensity of any of these signals as a function of the position. A SEM microscope, seldom reach 50 KV and can show 40000x of magnification.

In this thesis, we were used two different SEM equipments, a TM3000 tabletop microscope (Hitachi High-Technologies Corporation) and a Quanta^{TM} 250 FEG (Intertek). In the first case, a direct magnification between 100x and 8000x and a voltage of 15 KV was used whereas the second case, a voltage of 30 KV and magnifications around 20000x was employed.

a.6 Wide-angle X-Ray scattering

The WAXS technique is used to determine the atomic and molecular structure of a crystal. This technique specifically refers to the analysis of Bragg peaks scattered to wide angles, which implies that they are caused by sub-nanometer-sized structures [8]. The diffraction pattern generated allows determining the chemical composition, phase composition, or the crystalline structure of materials.

The sample is scanned in a wide-angle X-ray goniometer, and the scattering intensity is plotted as a function of the 2θ angle. When X-rays are directed in solids, they will scatter in predictable patterns based upon the internal structure of the solid. A crystalline solid consists of regularly spaced atoms (electrons) that can be described by imaginary planes. The distance between these planes is called the *d*-spacing. The intensity of the *d*-space pattern is directly proportional to the number of electrons (atoms) that are found in the imaginary planes

In this thesis, X-ray diffraction patterns were recorded on a Philips Expert Pro, using Cu $K_{\alpha 1}$ radiation (λ = 1.54056 Å), with a back monochromator. The radiation source was operated at a generator voltage of 40 kV and a current of 40 μA. The scans were carried out over the range from 2° to 70° (2θ) at 25 °C. Powder samples were manually compressed into the sample holder to produce pellets.

a.7 ^{29}Si MAS-NMR

Nuclear magnetic resonance (NMR) is a physical phenomenon in which a nucleus in a magnetic field absorbs and re-emits radiation. The specific resonance frequency of the radiation emission depends on the strength of the magnetic field and the magnetic properties of the isotope of the atoms. NMR allows the observation of specific quantum mechanical magnetic properties of the atomic nucleus. The NMR applied to solid samples is frequently used to determine their structures.

NMR interaction has isotropic and anisotropic interactions, in function of the direction and intensity of the magnetic field. The anisotropic interactions depend of the expression $3\cos^2(\theta - 1)$ being θ the angle between the magnetic field and the molecules of the sample. With simples geometrical considerations, if we choose θ = 54° 44', the expression is equal to 0, canceling all the anisotropic interactions. This angle is called "magic angle", which gives name to the device (MAS-NMR). Despite of avoid the anisotropic interactions; there are some problems for NMR solid measurements, as chemical shift, scalar and dipolar attachment and quadrupole interactions.

^{29}Si MAS-NMR has been a great advantage to determine silicon-like structures. A ^{29}Si MAS-NMR signal is perfectly characterized by three parameters: position, width and intensity. The chemical shift is determined for the signal position in the spectrum in the frequency domain. The silicates structures can be explained from tetrahedrons that share from zero to four corners. Q^n nomenclature is used to describe the condensation degree of silicates units. *Q* indicates the binding of silicon with oxygen atoms and the *n* is the number of tetrahedrons linked by corners. In this way, Q^0 describes an insolated tetrahedron, Q^1 a tetrahedron that share a corner with another tetrahedron, Q^2 two corners, as it is represented in figure III.7. The chemical shift regions are not exclusive for each kind of condensation, where the signals can be overlap (see Figure III.8)

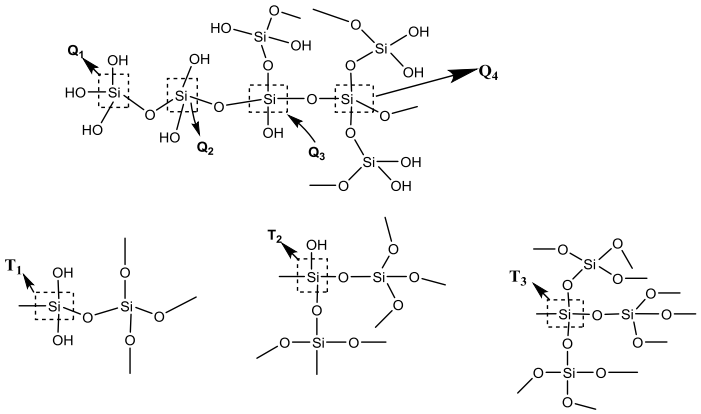

Figure III.7 Scheme of the different silicon positions in function of the *n* value.

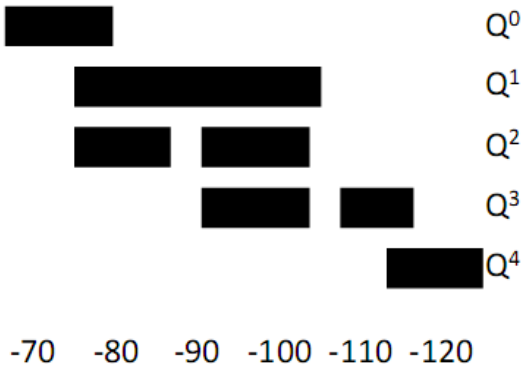

Figure III.8 ^{29}Si Chemical shift in function of the condensation grade of the SiO_4 tetrahedron.

Another important application is the study of alumino-silicates, when occurs an isomorphic substitution of silicon by aluminum. To determine Q^n, there is a displacement to more negative values when the number of aluminum that encloses the silicon atoms increased. Q^n(1Al) means that the silicon is enclose by one Al and *n* oxygen atoms. Q^n(2Al) means a silicon enclosed by two Al and n oxygen atoms, etc…

In this thesis we have used a ^{29}Si NMR to study silicon molecules in solid state. The device used was a Bruker Avance III, 9.4 T with ^{29}Si frequency of 79.495 MHz. The probes were CP/MAS with 4 mm of diameter. The pulse program was *High power decoupled*, at room temperature, with spinning rate of 10000 Hz, being the number of scans about 10000 per sample.

a.8 X-Ray Fluorescence

X-ray fluorescence (XRF) spectrometer is a relatively non-destructive X-ray instrument used for the chemical analyses of rocks, minerals, sediments and fluids.

In this thesis we have used a WDXRF by PANalytical, AXIOS model with three detectors (gas flow, scintillation and sealed by Xe)

b. Materials

In this section we will explain the protocols to prepare the different samples used in this thesis.

b.1 Calcium silicate hydrate (C-S-H gel)

C-S-H gel was prepared by mixing 5 g of pure tricalcium silicate (C_3S) with 1400 g of distilled water. The great water to C_3S ratio served to maintain the calcium concentration in the solution low enough to prevent portlandite precipitation, but without affecting to the formation of C-S-H gel. The resulting dispersion was sealed in a container to avoid carbonation, and after 39 days of continuous stirring at room temperature, the dispersion was filtered and the obtained solid material was dried in an oven at 60 ^{o}C for an hour. The resulting C-S-H gel had a water content of c_w = 22 wt %, determined by TGA

The X-ray fluorescence analysis reveals the presence of SiO_2 (29.64%) and CaO (38.46%), and trace amounts of Al_2O_3 (0.12%) and Fe_2O_3 (0.05%), being the Ca/Si ratio 1.29.

b.2 C-S-H gel synthesized with the addition of nanoparticles

The synthesis described in this section was done in collaboration with Tecnalia (Dr. Juan José Gaitero, Dr. Edurne Erkizia). First, we describe the nanoparticles used in the synthesis of C-S-H gel. We have used two different types of nanoparticles:

1) Colloidal amorphous Silica (Nyasil^{TM} 20 – Nyacol Nano Technologies, Inc) with a specific surface, $S_{specific}$ = 167 m^2/g (mean diameter of the primary particles is 15 nm with a mean agglomerate size of 1400 nm) and pore volume = 1.74 cm^3/g according to the data provided by the manufacturer.

2) Amine functionalized silica nanoparticles (Stoga). The route of synthesis is based on the Stöber method [9] although in this case the tetraethoxysilane reagent is reacted with aminopropyltriethoxysilane in a one pot reaction to obtain the amine functionalization. Ethanol (4 L), water (83.3 mL), tetraethoxysilane (121 mL, 0.542 moles) and (3-aminopropyl) triethoxysilane (13.2 mL, 0.0566 moles) are added to a 5 L Pyrex glass container. To this, concentrated ammonium hydroxide (39 mL) is added and the reaction is left stirring for three days. After three days, a white colloidal dispersion is obtained. The solid is separated from the solvent by centrifuge and decanting. The solid is washed three times with ethanol to remove any reactants and centrifuged and decant to collect it. The white solid obtained is air dried. The yield of the nanoparticles is around 40 g (between 35 g and 41 g). Size measurement by dynamic light scattering of the reaction dispersion, before centrifuging, of the nanoparticles was performed with a Zetasizer nano ZS (Malvern Instruments) giving a primary particle size of 150-160 nm. However, after the centrifuging and drying the nanoparticles are agglomerated. The ^{29}Si CP-MAS solid NMR (see Figure A of supplementary information) spectrum shows 4 resonances: -111.7 ppm (Q_4), -102.0 ppm (Q_3), -67.9 ppm (T_3) and -62.2 ppm seen as a shoulder in the previous peak (T_2). The ^{13}C CP-MAS NMR spectrum of the product shows three resonances due to the 3 carbons in the aminopropyl group (42.3 ppm (-**C**H_2-NH_2), 21.0 ppm (-**C**H_2-CH_2-NH_2), 9.0 ppm (SiO_2-**C**H_2-CH_2-)) [10]. In Figure III.9 shows a scheme and SEM image of both nanoparticles.

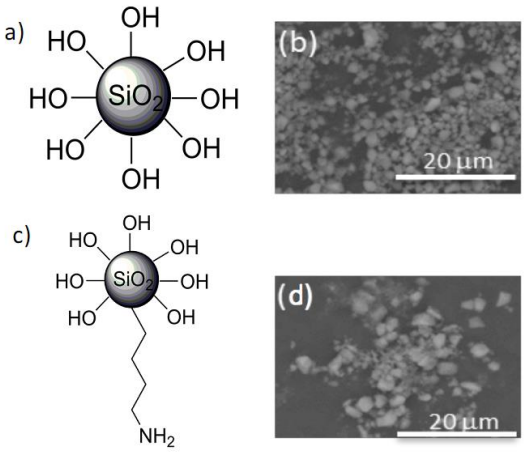

Figure III.9. a) and b) shown a scheme and a SEM image of Nyasil^{TM} nanoparticles, respectively. c) and d) shown the Stoga nanoparticle.

Figure III.10 shows the results of the thermogravimetric analysis of silica (Nyasil^{TM}) and amine functionalized silica (Stoga) nanoparticles respectively. For Nyasil^{TM} two steps on the thermo-grams are observed (seen as peaks in the derivative plot in the inset of Figure III.10). The first rapid initial drop of the mass (from room temperature up to 200 ^{o}C) corresponds with the loss of both adsorbed water on the silica surface and structurally bound water within the silica skeleton [11]. Above 200 ^{o}C, vicinal and geminal silanol groups on silica particles are condensed to siloxanes, and this is seen as a weight drop in a broad temperature range from 200 to 800 ^{o}C [11]. For Stoga particles, three steps are observed. The first step corresponds with the release of water whereas the second one between 200 and 400 ^{o}C, corresponds with the condensation of silanol groups to siloxanes. Finally, the last step between 450 and 800 ^{o}C corresponds with the decomposition of amino groups (which are absent in Nyasil^{TM}) [12].

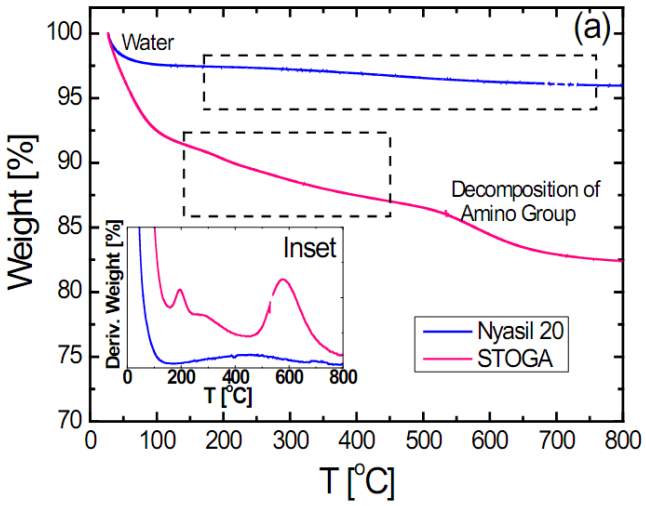

Figure III.10. Thermogravimetric measurements (TGA) of the loss mass up to 800 °C for STOGA and NYASIL-20 silica nano particles as indicated in the figure. The inset shows the weight derivative plot.

Synthesis of C-S-H gel with the addition of nanoparticles: The C-S-H gels with nanosilica were prepared in the same way than CSH gel but also adding Stoga or Nyasil™ nanoparticles. In the case of Stoga we have used 1.36 grams whereas for Nyasil™ 1.2 grams were used. In this way both samples had the same silica percentage. Silica nanoparticles were dispersed in 150 g of water using an ultrasonic probe before adding the rest of the water and the C_3S. The solid material obtained at the end of the hydration process (33 days) was visibly wet even after the 60 min of drying at 60 ºC. As a consequence, drying time was increased in another 20 min. The resulting C-S-H gels had a water content of about c_w = 24 wt % for both types of nanoparticles. Immediately after preparation, samples were further dried at 70 °C in a vacuum oven (this temperature allows water evaporation without structural damage) to reach the same water concentration of ordinary C-S-H sample.

The values of the different components obtained by TGA are showed in Table III.1.

Table III.1 Values obtained by TGA of the water (c_w), and carbonatation (c_{carb}) content for the C-S-H samples

	c_w [wt%]	c_{carb}[wt%]	Ca/Si ratio
C-S-H	21.20	7.90	1.30
C-S-H Stoga	21.20	5.50	1.00
C-S-H Nyasil ™	21.80	2.70	1.00

b.3 Tobermorite

In this thesis, we have used two types of tobermorite. The first one is a natural specimen whereas the second one was synthesized in the laboratory.

Natural Tobermorite: Natural tobermorite was obtained from Sverdlovskaya Oblast, Middle Urals, Russia. Macroscopically, the bulk sample has white needle-like crystals in the interior of the rock (see Fig. III.12.a)). The SEM micrograph (Fig. III.11.b)) shows the typical elongated thin crystals that are observed in natural tobermorite [13]. These needle-like objects are also observed in the transmission electron microscopy micrographs (TEM, see Fig. III.11.d). TEM images reveal a layered structure with an interlayer distance of 1.1 nm. The water content was analyzed using thermogravimetric experiments (see Fig. III.11). The TGA shows a weight loss from room temperature to approximately 200 °C (because of water loss) and another at approximately 600 °C (because of the decomposition of $CaCO_3$). From this experiment, the "as received" sample contains 10.60 wt% of water.

The water content (c_w) was determined based on the "dry" sample. The X-ray fluorescence analysis reveals the presence of SiO2 (41.75 %), CaO (37.07 %), Al2O3 (5 %), MgO (0.26), K2O (0.20) and Fe2O3 (0.17 %), where the number between the brackets represents the weight percentage with respect to each oxide. The Ca/Si ratio is 0.89.

Tobermorite Synthesis: For the hydrothermal synthesis, 3.36 gr of CaO, 9.37 gr of colloidal SiO_2 (Levasil 100/45 % with a solid content of 45 wt%) and 0.23 gr of nanoalumina (Al_2O from Nyacol Nano Technologies) were added to 1.5 L of water with an initial Ca/Si ratio of 0.85. The mixture was maintained at 200 ºC and stirred for 4 hours. Then, the product was filtered and dried at 60 °C for 12 h. Tobermorite was disaggregated with a mortar and pestle to obtain a fine powder and stored at room temperature until use.

The X-ray fluorescence analysis reveals the presence of SiO_2 (4.37%), CaO (35.37%), Al_2O_3 (2.01 %) and MgO (0.22), and the Ca/Si ratio is 0.82. The "as received" sample contains c_w = 10.90 wt% (TGA experiment, Fig. A). The SEM

micrograph (Figure III.11.c) shows a lower overall crystalline material (less crystalline than natural tobermorite), but the TEM micrographs (Figure III.11.e) show the expected layered structure (1.1 nm), which correlates with the X-ray diffraction investigation.

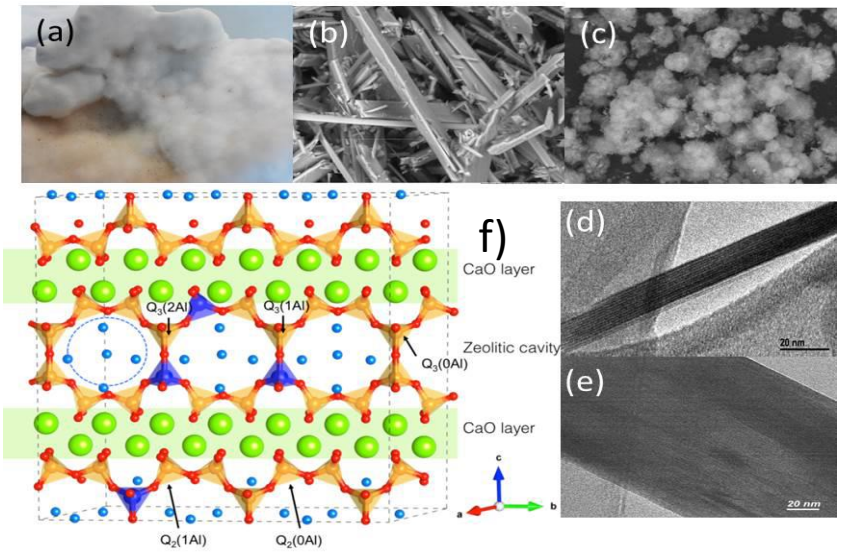

Figure III.11. a) and b) shown images of Natural Tobermorite, at real scale and with SEM, respectively. c) is a image of Synthetic Tobermorite by SEM. d) and e) shown TEM images of Natural and Synthetic Tobermorite respectively. f) represents, schematically, Anomaly Tobermorite.

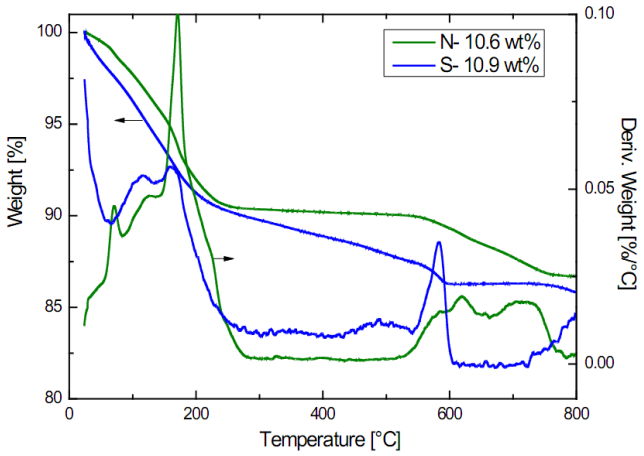

Figure III.12. TGA at 5K/min of both samples, Natural (N) and Synthetic (S) Tobermorite with 10.6 and 10.9 wt% respectively.

The values of the different components obtained by TGA are showed in Table III.2.

Table III.2 Values obtained by TGA of the water (C_w), and carbonatation (C_{carb}) content for the tobermorite samples

	c_w [wt%]	c_{carb}[wt%]	Ca/Si ratio
Natural Tobermorite	10.60	3.60	0.90
Synthetic Tobermorite	10.90	1.30	0.80

b.4 Ordinary Portland Cement (OPC)

The materials described in this section were done in collaboration with the Civil and Environmental Engineering of Chalmers University (Dr. Helen Jansson). The OPC used was supplied for the Cementa (Heidelberg Cement Northern Europe, Sweden). These cements were prepared with different water-to-cement ratio (from 0.3 to 0.4). The water-to-cement ratio, like the hydration degree, are an important factors in the determination of the porosity of hydrated cement (see Figure III.13). The water-to-cement ratio determines the percentage of hydration products and also the distribution of the porosity, which in turns determines the strength or shrinkage [14].

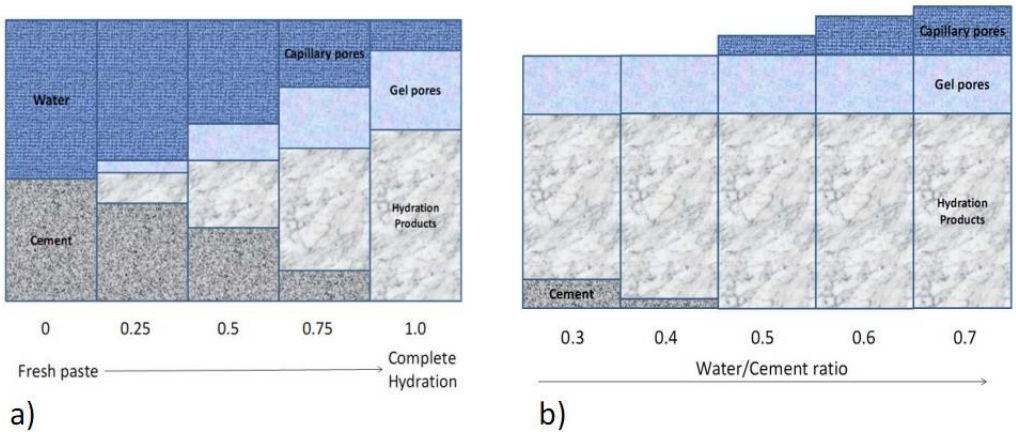

Figure III.13. Volume relationship among constituents of hydrated Portland cement pastes in function of a) the hydration degree and b) the water/cement ratio

For the sample preparation, distilled water was used. To avoid water evaporation and sedimentation during the hardening, each sample was casted in a sealed plastic tube (diameter 2 cm), which was slowly rotated during 2 days. After 1 week of hydration, circular samples was cut from the hardened material and then stored in plastic bags at room temperature (298 K). The analysis of the samples was done 3 weeks after the preparation casting.

Figure III.14 shows the TGA response of cement samples as received. We can observe three different steps, being from lowest temperature to highest, the water loss of the sample, the decomposition of the CaOH and decomposition of $CaCO_3$ into CO_2 and CaO. The values of the different components obtained by TGA are showed in Table III.3

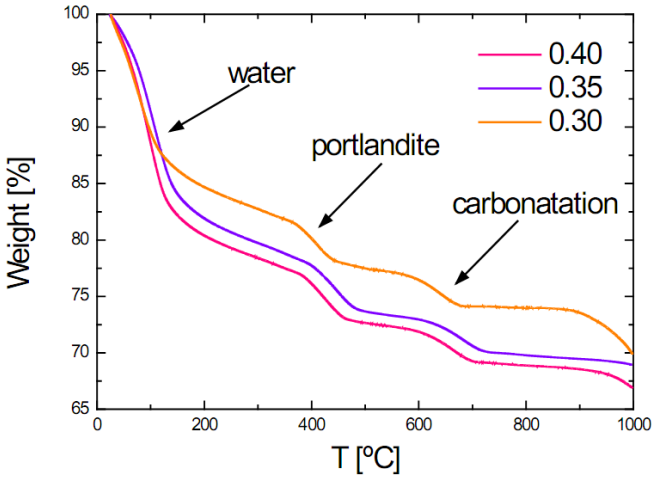

Figure III.14 TGA of all the cement samples at 5K/min. Three clear steps are observed, related with the water, portlandite and $CaCO_3$ decomposition.

Table III.3 Values obtained by TGA of the water (C_w), portlandite (C_{portl}) and carbonatation (C_{carb}) content for the cement samples.

Sample	w/c	c_w [wt %]	c_{port} [wt %]	C_{CaCO3} [wt %]
Cem-0.40	0.40	24.50	5.50	3.80
Cem-0.35	0.35	22.10	5.90	3.70
Cem-0.30	0.30	18.10	4.50	3.40

The X-ray fluorescence analysis reveals the presence of different oxides as shown in Table III.4. The Ca/Si ratio obtained was 3.31. For comparison, we also analyze a sample of white cement at *w/c* = 0.4. The result obtained with X-ray fluorescence analysis of this sample is also seen in Table III.4.

Table III.4. Chemical analysis obtained through fluorescence analysis

Sample	SiO_2	Al_2O_3	Fe_2O_{3t}	MnO	MgO	CaO	Na_2O	K_2O	TiO_2	P_2O_5	SO_3
Portland cement	14.54	2.93	2.20	0.03	1.83	48.20	0.07	0.72	0.22	0.04	1.78

c. References

1. Günther, H., Hemminger, W. F. and Flammersheim, H.-J. *Differential Scanning Calorimetry*. (2003).

2. Kremer, F. and Schönhals, A. *Broadband Dielectric Spectroscopy*. *Springer: Berlin* 729 (2003).

3. Böttcher, C. J. F. *Theory of electric polarization*. 92 (1973).

4. Kubo, R. The fluctuation-dissipation theorem. *Reports Prog. Phys.* **29,** 255–284 (1966).

5. Debye, P. Polar molecules. *J. Soc. Chem. Ind.* **48,** 1036–1037 (1929).

6. Cole, K. S. Dispersion and Absorption in Dielectrics II. Direct Current Characteristics. *J. Chem. Phys.* **10,** 98 (1942).

7. MaCrum, N. G., Read, B. E. and Williams, G. *Anelastic and dielectric effects in polymeric solids*. *Journal of Applied Polymer Science* 617 (1967).

8. Podorov, S. G. *et al.* A new approach to wide-angle dynamical X-ray diffraction by deformed crystals. *J. Appl. Crystallogr.* **39,** 652–655 (2006).

9. Stöber, W., Fink, A. and Bohn, E. Controlled growth of monodisperse silica spheres in the micron size range. *J. Colloid Interface Sci.* **26,** 62–69 (1968).

10. Perez, G., Erkizia, E., Gaitero, J. J., Kaltzakorta, I. and Jiménez I., G. A. No Title. *J. Mater. Sci. Sci.*

11. Cerveny, S. *et al.* Dielectric Study of Hydration Water in Silica Nanoparticles. *J. Phys. Chem. C* **116,** 24340–24349 (2012).

12. Bayal, N. and Jeevanandam, P. Synthesis of SiO2@NiO magnetic core–shell nanoparticles and their use as adsorbents for the removal of methylene blue. *J. Nanoparticle Res.* **15,** 2066 (2013).

13. Tränkle, S. *et al.* Conventional and microwave assisted hydrothermal syntheses of 11 Å tobermorite. *J. Mater. Chem. A* **1,** 10318 (2013).

14. Mindess, S. and Young, J. F. *Concrete*. 671 (1981).

Chapter IV

Water dynamics confined in C-S-H gel

The C-S-H gel is not only the most abundant reaction product, but it is also responsible for most of the engineering properties of the cement paste. As explained in Chapter I, C-S-H gel forms a continuous layer that binds together different crystalline phases developed during cement hydration, into a cohesive whole. The ability of the C-S-H gel to act as a binding phase arises from its nanometer-level structure and in particular from the internal pore system. Models to explain this nanostructure were explained in Chapter I.

Most of the engineering properties of cement are related to the porosity and the water entrapped in this porosity. However, to characterize the porosity and the distribution of water of hydrated cement paste is difficult. Because of the large range of pore sizes (from nanometers to tens of micrometers), no single technique can adequately characterize all of the components of the pore system. Moreover, to study the dynamics of confined water in cementitious materials, there are only three techniques available as also discussed in Chapter I.

In this chapter, we show that broadband dielectric spectroscopy is an appropriated technique to study dynamics of water confined in C-S-H gel and other cementitious materials. From a scientific perspective, C-S-H offers an attractive confinement system where chemical and geometrical effects of the confinement of water can be investigated. We discuss the use of C-S-H gel for investigating the possible existence of a fragile-to-strong transition for water around 220 K. Such transition was observed at 220 K in a previous study [1] on a similar system, and it was there associated with a hidden critical point of bulk water. However, based on the experimental results presented here, there is no sign of a fragile-to-strong transition for water confined in C-S-H gel. Instead, the fragile-to-strong transition can be explained by a merging of two different relaxation processes at about 220 K.

a. Introduction – Dielectric response of C-S-H gel

In a previous work [2], the influence of the hydration level on the dielectric response of C-S-H gel was studied. Different water contents in C-S-H gel were explored (from 6 to 15 wt%) where water remains amorphous for all the studied temperatures. The dielectric spectra revealed three different relaxation processes (see Figure IV.1) related to water molecules in C-S-H samples [2]. Each process has shown its own dynamical characteristics and two of them (2 and 3) are originated in different populations of water molecules. In the following, we described the most important characteristics of each relaxation process based on the relaxation maps at different water contents shown in Figures IV.2 and IV.3.

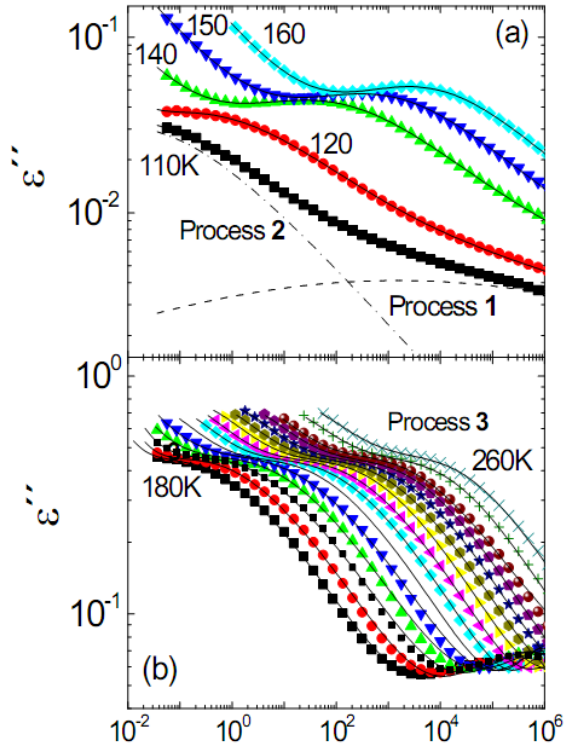

Figure IV.**1** (a) Dielectric loss spectra of C-S-H gel with c_w = 11 wt% measured at different temperatures (110, 120, 140, 150, and 160 K); (b) Dielectric loss spectra of the same sample measured at temperatures from 180 K to 260 K each 5 K. Process 1, 2, and 3 denotes the three dielectric processes observed. The solid line through the data points represents the fits to the experimental data. In (b) dotted line represents the relaxation corresponding to process 1 whereas the dashed-dotted line represents process 2.

Process 2: The temperature dependence of the relaxation time of process 2 (see Figure IV.2) showed Arrhenius behavior at low hydration level with relatively low activation energy but as soon as one monolayer of water was reached by increasing hydration, a crossover in the temperature dependence of the relaxation times (from high-temperature non-Arrhenius to low-*T* Arrhenius) was observed. The presence of

this crossover was related with confinement effects [2] and the confinement size was estimated to be 1 nm.

Process 3: At low hydration level the temperature dependence of process 3 also showed an Arrhenius behavior but the activation energy was higher than that of process 2, indicating that water clusters exist even from low hydration levels. In addition, by increasing the hydration, the probability of water molecules to form big clusters increases and therefore water molecules can relax in a cooperative way. At the higher hydration level (15 wt %) water dynamics follows a VFT behavior indicative of cooperative-type motions. No confinement effects were observed for this process, indicating that for this type of water no topological constraints exist and therefore water molecules should be located in big pores.

Process 1: The origin of the fastest relaxation (process 1) observed in C-S-H gel is not obvious. At very low temperatures (130–150 K) it appears as an excess wing, and it cannot be resolved as a separate peak, whereas at higher temperatures (above 200 K) it emerges as a well-resolved peak. It was observed that the relaxation strength of this fastest process is very small compared to that of the main peaks (processes 2 and 3) and that its intensity slightly depends on the water content [1].

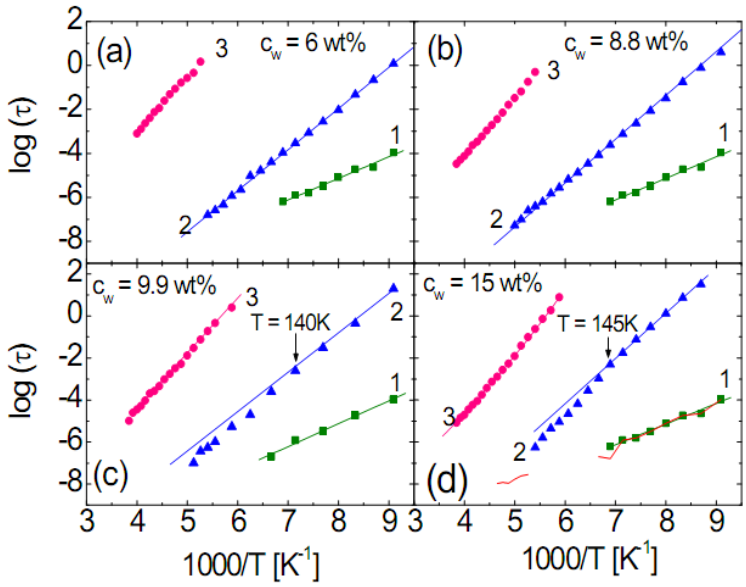

Figure IV.**2** Temperature dependence of the relaxation time τ (T) for C-S-H samples at different water content. All three processes (1 to 3) have an Arrhenius temperature dependence at low water content [see (a) and (b)]. In (d) process 2 shows a slight crossover at 145 K whereas process 3 has Vogel–Fulcher–Tamman temperature dependence. The lines are fits according to the Arrhenius or VFT equation (see text).

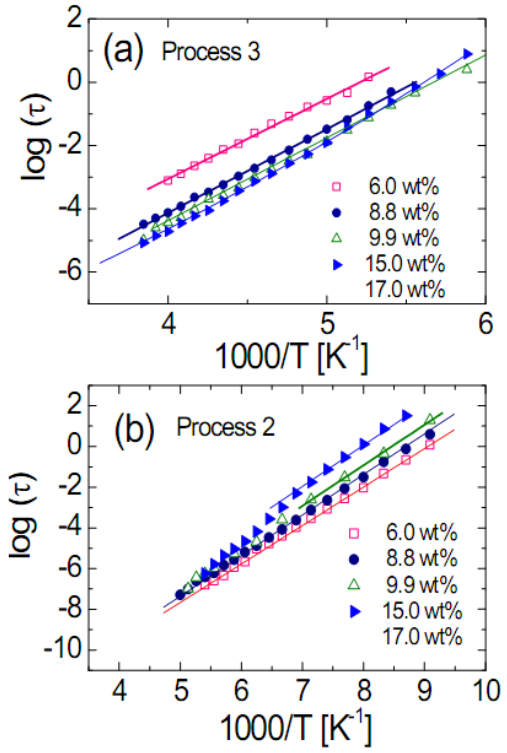

Figure IV.3. Comparison of the temperature dependence of the relaxation time τ (T) for process 3 [in (a)] and process 2 [in (b)] at the different water contents.

b. Dielectric response of C-S-H gel at high water content

b.1 Motivations: In this section we will present the rotational dynamics of hydration water confined in calcium-silicate-hydrate (C-S-H) gel with a water content of c_w = 22 wt%. The motivation behind this study is to analyze the existence of a second critical point proposed for bulk water.

Among a number of atypical properties of bulk water [3,4], a phase transition from a high density liquid to a low density liquid (the liquid-liquid critical point hypothesis [5] in the supercooled liquid region of the water phase diagram) in the temperature range of 220-230 K was predicted [6] (see chapter II). This phase transition is supposed to emerge as a sudden change in the water dynamics, at some point, in the temperature range where water normally crystallizes. Nevertheless, crystallization of water can be avoided by surface interactions or by confining it in small cavities (with a characteristic size of tens Å) and, therefore, some authors have tried to verify this hypothesis by study confined water, instead of bulk water, and from the results the existence of a "fragile-to-strong" transition of confined water at about 220 K have been

proposed. However, this fragile-to-strong scenario has been questioned and, despite numerous discussions, still an agreement has not been reached. It should, however, be noted that confinements always introduce surfaces, which, in turn, have an influence on, as well as modify, the water dynamics. Therefore all extrapolations of such observations to the properties of the bulk state should be done very carefully.

The fragile-to-strong scenario and its possible origin have been widely debated in the literature. From quasi-elastic neutron scattering (QENS) studies it has been observed that the relaxation times of confined water exhibit an abrupt crossover from a non-Arrhenius to an Arrhenius dependence as the temperature decreases, which has been associated with the appearance of the fragile-to-strong transition (FST) expected for bulk water. The sharp change in temperature behavior has been observed for water in a variety of confining systems such as MCM-41 [7], carbon nanotubes [8], white cement [1] as well as in aqueous solution of DNA [9], RNA [10] and lysozyme [11]. Some of these, or similar confining systems, have also been studied by using other different experimental techniques, such as broadband dielectric spectroscopy (BDS) [12–19], nuclear magnetic resonance (NMR) [20], or a combination of different techniques [21–26]. In such studies, most likely due to the broadband frequency range analyzed such crossover for water was either not observed, or attributed to other causes different to that of the fragile-to-strong transition scenario. Thus, no correlation was found by studies of the same sample by QENS and other techniques.

As mentioned, one of the systems investigated by QENS was hydrated cement in which an abrupt crossover was shown to occur for confined water [1]. Therefore we analyzed the dynamics of water confined in C-S-H gel in both a broader frequency (10^{-1}-10^{8} Hz) and temperature (110-300 K) range using broadband dielectric spectroscopy. We explore a higher water content since it enhances the sensitivity at higher frequencies (c_w = 22 wt%, expressed as grams of water/grams of dry cement).

The results are presented in two different ways:

1) Analysis of the dielectric permittivity in the high frequency range 10^6-10^8 Hz
2) Including also lower frequencies and analyze the data in the broad frequency interval 10^{-1} – 10^8 Hz

This twofold analysis method reveals that: 1) only considering a restricted frequency interval, the relaxation times seem to exhibit a clear crossover at T = 220 K, and thereby, we are able to reproduce the exact relaxation map obtained in reference [1]. 2) Including also lower frequencies, i.e. investigating a broader frequency range, the suggested fragile-to-strong transition for water confined in C-S-H gel cannot be observed. Instead, two different well-resolved processes (denoted 1 and 2) are obtained. Obviously, the limitation of the frequency window is the origin of the apparent fragile-to-strong transition, i.e. the crossover in temperature dependence at 210K obtained by QENS. As above mentioned the origin of process 2, which is known to be due to the dynamics of water molecules in small pores, the origin of process 1 is not established before. In this thesis, we will show that the fast process 1 in cementitious materials might be related to a relaxation process that is observed in other systems in which hydroxyl groups are present and of relative importance.

b2. Thermal Characterization

C-S-H gel was prepared as explained in Chapter III (section b.1). The "as received" sample contains c_w = 28 wt% of water as measured by TGA (c_w, expressed as grams of water/grams of dry cement). A water content of 22 wt% was reached by drying the sample in a vacuum oven at 100 ^{o}C. This temperature allows water evaporation without structural damage. The sample was labeled as CSH-22.

Water behavior inside the structure of C-S-H gel was characterized by DSC. Figure IV.4 shows that for c_w = 22 wt%, there is crystallization of water at ~231 K. The depression of the freezing point indicates that water is confined in the solid structure developed during the formation of C-S-H gel. Crystallized water is probably located in pores larger than 3 nm [2]. This result is similar to previous observations for white cement [1].

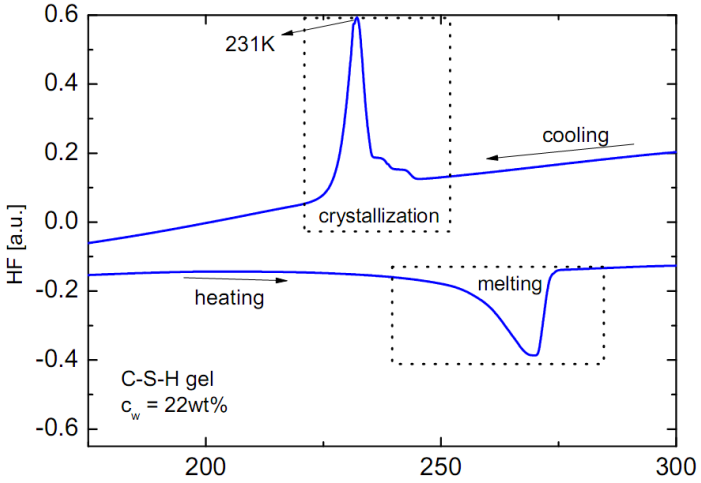

Figure IV.**4.** DSC heat flow curve obtained for the sample CSH-22. The exothermic and endothermic features displayed at cooling and heating is due to crystallization and melting of water, respectively.

b.3 Dielectric relaxation spectra in the frequency range 10^6-10^8 Hz

Figure IV.5 shows the imaginary part (ε'') of the complex permittivity at different temperatures measured (190 – 225 K) in the frequency range 10^6-10^8 Hz obtained for CSH-22. In this frequency region, one single peak is observed at all temperatures, which was fitted with a symmetrical Cole-Cole (CC) function. Figure IV.5 shows the result of the fitting by solid lines.

The temperature dependence of the obtained relaxation time (τ) is shown in Figure IV.6 by red squares. The time scale of this relaxation exhibits an Arrhenius-type temperature dependence below approximately T = (210 ± 5) K. At higher temperatures a clear deviation from the Arrhenius behavior is observed. This behavior is in good agreement with that obtained for white cement by quasielastic neutron scattering (QENS) [1] (see purple triangles in Figure IV.5). It is important to remark that the QENS relaxation times were obtained at four different Q values (0.2, 0.4, 0.6 and 0.8 $Å^{-1}$) simultaneously analyzed to extract the averaged relaxation time τ. In addition, it is indicated that the relaxation times is almost Q-independent [1]. Moreover, a comparison between dielectric and QENS relaxation times can be made since it is well-established that the time scale deduced from neutron scattering at a momentum transfer Q of about 0.9 $Å^{-1}$ is comparable with that obtained by dielectric spectroscopy [27]. As seen in Figure IV.5.b), the time scale obtained from QENS is in perfect agreement to the

corresponding time scale of the dielectric relaxation, as expected for the Q values analyzed. Below 210 K, the relaxation times are fitted by the Arrhenius equation.

The temperature dependences of the relaxation strength ($\Delta\varepsilon$) and shape parameter (α) are shown in Figure IV.5.c). Both parameters follow a smooth behavior, $\Delta\varepsilon$ and α increasing and decreasing with temperature, respectively, i.e. neither the shape parameter not the relaxation strength change its behavior at the crossover in temperature dependence around T = 210 K.

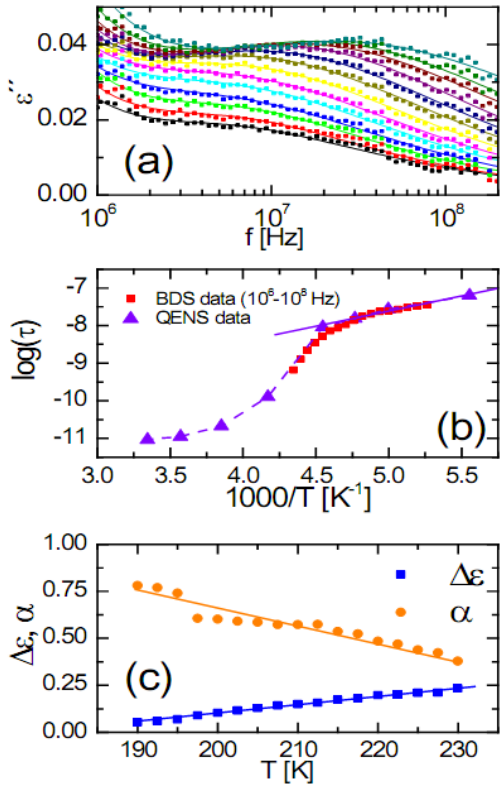

Figure IV.5 (a). The loss component, ε″, of the complex dielectric permittivity (ε*(f)) for CSH-22 at different temperatures. An apparent single dielectric process is observed in this frequency range. The solid line show the least-squares fit of a superposition of a power law for conductivity and a Cole-Cole function for the imaginary part. ***(b)*** Temperature dependence of the relaxation time $\tau(T)$ obtained from this fitting (red squares) compared to the relaxation times of white cement (purple triangles) obtained from reference [1]. The blue solid and dotted lines represent the Arrhenius and the VFT fitting of that sample, respectively. ***(c)*** Dielectric strength ($\Delta\varepsilon$) and shape factor (α) as a function of the temperature.

b.4 Dielectric relaxation spectra in a broad frequency range 10^{-1} to 10^{8} Hz

The situation becomes different when analysing the same sample in the broader frequency range 10^{-1} to 10^{8} Hz, i.e. including also lower frequencies. Figure IV.6 (a and b) shows the imaginary part (ε'') of the complex permittivity at 190K. In this case, we observe three dielectric processes (called process 1, 2 and 3 from the fastest to the slowest relaxation). Since all the obtained dielectric processes in the C-S-H gel are symmetric, we have used a superposition of three Cole–Cole (CC) functions plus a conductivity contribution (at low frequencies and high temperatures) to fit the dielectric spectrum at each temperature. Figure IV.6.a) shows the result of the total fitting as well as the contribution of the three different processes separately at T = 190 K.

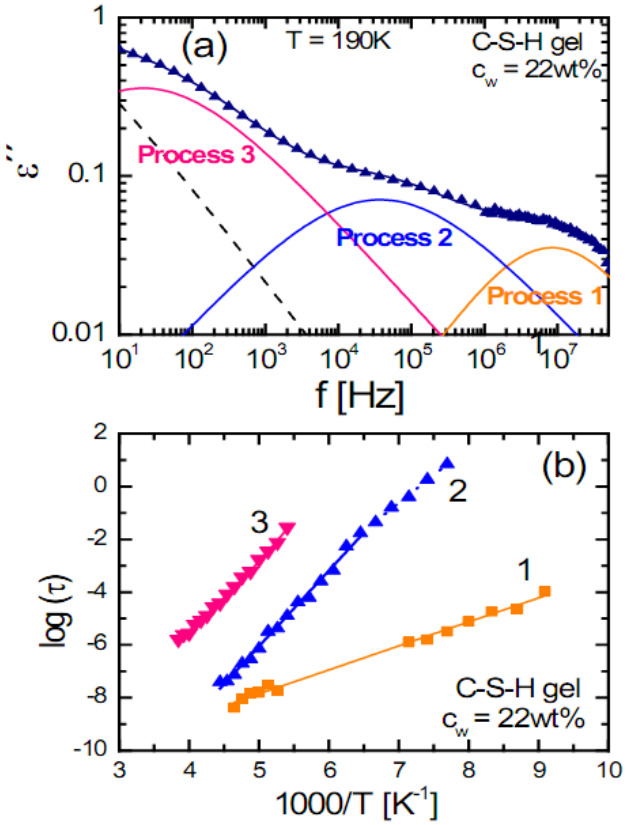

Figure IV.6 (a). The loss component, ε″, of the complex dielectric permittivity (ε*(f)) for CSH-22 at different temperatures. An apparent single dielectric process is observed in this frequency range. The solid line show the least-squares fit of a superposition of a power law for conductivity and a Cole-Cole function for the imaginary part. ***(b)*** Temperature dependence of the relaxation time $\tau(T)$ obtained from this fitting (red squares) compared to the relaxation times of white cement (blue triangles) obtained from reference [1]. The blue solid and dotted lines represent the Arrhenius and the VFT fitting of that sample, respectively. ***(c)*** Dielectric strength ($\Delta\varepsilon$) and shape factor (α) as a function of the temperature.

The temperature dependence of the relaxation times is shown in Figure IV.6b. The relaxation time of process 1 follows an Arrhenius behavior in the entire temperature range, with an activation energy of 0.18 eV and $\log(\tau_0) = -12.4$. Process 2 presents a crossover from high temperature non-Arrhenius behavior to low temperature Arrhenius behavior at a temperature of T_{cross} = 155 K. Table IV.1 shows activation energies and the pre-exponential factor for all water contents for process 2. Process 3 shows a non-Arrhenius behavior which can be fitted with a single VFT. All these results are consistent with the previous results at lower hydration level [2].

Figure IV.7 shows the comparison of the relaxation times obtained from both the restricted frequency and the broad frequency interval, as well as the relaxation times obtained by QENS in reference [1].

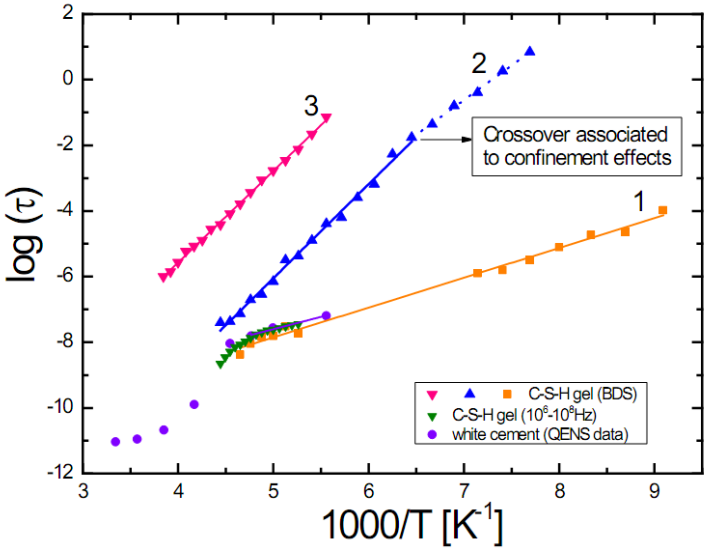

Figure IV.7. Comparison of the relaxation times of CSH-22 and that obtained by QENS [1] obtained for the two different analysis approaches shown in figures IV.5.b) and IV.6.b).

Table IV.1. Activation energy E_a and pre-exponential factor $\log(\tau_o(s))$ corresponding to process 2. Data at low water content were obtained from reference [2].

Sample	c_w [wt %]	Process 2	
		Log (τ_o(s))	E_a (eV)
CSH-06	6.25	-17.0±0.1	0.37±0.01
CSH-09	9.75	-17.5±0.6	0.39±0.02
CSH-11	11.00	-18.2±0.2	0.46±0.02
CSH-15	15.10	-15.4±0.2	0.41±0.03
CSH-22	22.00	-15.4 ± 0.2	0.41± 0.03

c. Discussion

c.1 Crossover at T = 145K associated to finite size effects

The change in temperature behavior of the relaxation times of process 2 at about 145 K, resemble the VFT to Arrhenius crossover, expected for the α-relaxation of glass forming liquids, if the confinement is severe enough [28,29]. This effect can be rationalized in the framework of the cooperativity of the dynamic glass transition [28]. Different models have been proposed to explain the non-Arrhenius behavior of the α-relaxation of glass forming liquids that all assume that the liquid consists of regions which are dynamically correlated. According to Adam and Gibbs [30], glass-formers are characterized by a self-organization of the molecules in the liquid, forming cooperatively rearranged regions (CRR). A CRR is defined as a subsystem, which can rearrange into another configuration, independently of its environment. The CRR size is small at high temperatures and increases with decreasing temperatures. Approaching the glass transition the size of the CRR becomes infinitely large (see cartoon in Figure IV.8) and a temperature dependence described by the VFT law can be deduces.

The CRR size can be described by a characteristic length ξ, that increases with decreasing temperature until the cooperative region comprises the whole system causing the freezing of mobility at T_o (see cartoon in Figure IV.8). The characteristic length of the CRR at T_g was estimated to be 1-4 nm, by different experimental techniques [31–36], for several materials (polymers and glass forming systems). In this picture, confinement induces a crossover in the temperature dependence of the relaxation times when the CRR size reaches the characteristic confinement length. Below this temperature the CRR would remain constant and Arrhenius-like temperature dependence is expected.

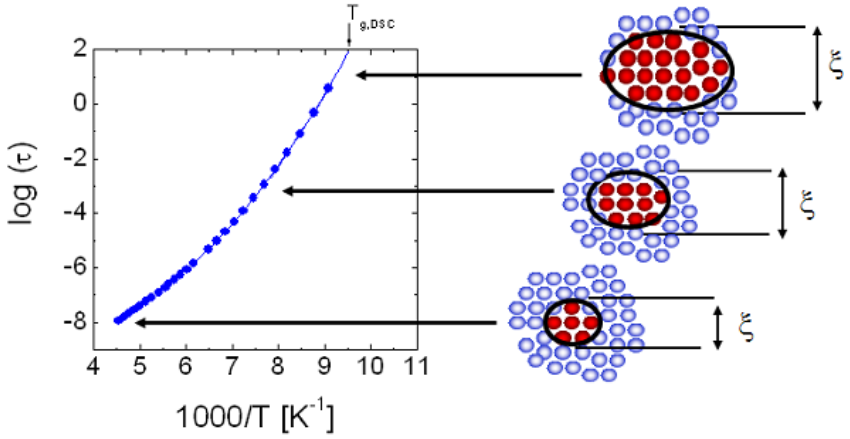

Figure IV.8. Generic relaxation map showing the temperature dependence of the α-relaxation. The temperature at which this process reaches a relaxation time of 100s ($\log(\tau) = 2$) is defined as the glass transition temperature (T_g). In the figure a schematic illustration of the hypothetical cooperatively rearranged region (CRR), and how its size increases with decreasing temperature, is given.

Taking the above arguments into account, process 2 could be assigned to the α-relaxation of water confined in C-S-H gel. Then, the crossover observed can be understood as an onset of finite size effects. At high temperatures (T > 145 K) the CRR size is smaller than the size of the confinement and a VFT-like temperature dependence of the relaxation time is observed. When the temperature is decreased (and the size of the CRR is expected to increase) the presence of confinement walls results in a limitation of the CRR growth. Consequently, an Arrhenius behavior of the relaxation time is detected at lower temperatures. Since the calorimetric glass transition temperature (T_g) corresponds to the VFT extrapolation to relaxation times in the order of 100 s, it would not be experimentally detectable by DSC. A similar behavior has already been observed for several polymers confined under nanometric conditions [28,37–39].

The presence of such a crossover (associated with confinement effects) for water dynamics in well-defined confinement systems has been observed in different types of systems. Water molecules confined in graphite oxide [40] show a crossover at about 180 K, water in molecular sieves at 185 K [41] and water confined in MCM-41 at 180 K [12]. Nevertheless, it is important to note that when water molecules do not suffer from confinement effect, the crossover is not generally observed. Instead, the temperature dependence of the relaxation time is shown to be of Arrhenius type in the

whole temperature range. The absence of such a confinement-related crossover was recently reported in the case of water around silica particles (SiO2) [42], and on rutile (TiO2 particles) [43]. Interestingly, an Arrhenius behavior over the full range of experimental temperatures was also observed for a monolayer of water confined in MCM41 [44]. Note that the main difference between C-S-H gel and silica particles is the fact that in the gel, water is confined in nano-pores of different sizes, whereas on the surface of the particles (SiO_2 or TiO_2) this restriction does not emerge since water molecules are located on the external surface.

c.2 Relaxation map – Comparison between BDS- and QENS-experiments.

As obvious from Figure IV.4b, the temperature dependence of the relaxation times that is obtained by fitting the dielectric data only in a restricted frequency interval (10^6 - 10^8 Hz) resembles that obtained by QENS [1]. We thus get a relaxation map where this process changes from a low temperature Arrhenius behavior to non-Arrhenius dependence at higher temperatures. The change in temperature dependence is observed as an abrupt crossover at about 220 K. The crossover together with an only smoothly variation of the CC (eq. IV.1) fitting parameters (relaxation strength ($\Delta\varepsilon$) and symmetric shape parameter (α) in the entire temperature range (Figure IV.5.c)), gives the impression of one single relaxation process that changes its temperature dependence around 220 K. As a consequence, by taking only this limited frequency interval in consideration, it is possible to believe in the existence of a fragile-to-strong transition displayed by an abrupt crossover in the temperature dependence of the relaxation process. However, by taking a broader frequency interval into account, a different scenario is obtained (Figure IV.6). In contrast to the sudden change in temperature dependence as obtained by QENS (and also by BDS in the limited frequency interval) the relaxation process is well described by an Arrhenius temperature dependence in the entire temperature range where it is visible. However, as seen in Figure IV.6.b, in the temperature interval where the apparent crossover occurs, two different relaxation processes (1 and 2) are approaching in time. At low temperatures (T < 180 K) these two processes are well separated in frequency, whereas at higher temperatures they become very close to each other. So, if the analysis is performed in a restricted frequency interval, only the faster relaxation is observed and, consequently, the crossover is produced. Thus, the crossover is only a merging between two different processes. This

behavior is also in agreement with a recent study on LiCl solution by dielectric spectroscopy and dynamic light scattering [24] where it was shown that the fragile-to-strong transition is only an effect of the limited resolution obtained by QENS. The effect of resolution and the choice of analysis method were also discussed by Doster et al. [21] in a recent QENS study on protein hydration water. Thus, for water confined in various systems, including C-S-H gel, the apparent crossover is not due to a fragile-to-strong transition. Rather it is a consequence of that the analysis is performed in a limited frequency interval, which at least for the C-S-H gel is the merging region of two different relaxation processes, which occur at temperatures above 210 K.

c.3 Possible Molecular Origin of the fastest relaxation in C-S-H

As mentioned above, the origin of the fastest relaxation process (process 1) observed in C-S-H gel is not obvious. At very low temperatures (130-150 K) it appears as an excess wing, and it can thus not be resolved as a separate peak, whereas at higher temperatures (above 200 K) it emerges as a well-resolved peak. In our previous study we observed [2] that the relaxation strength of this fastest process is very small compared to that of the main peaks (processes 2 and 3) and that its intensity slightly depends on the water content. Therefore, we have, stepwise, removed most of the water from the C-S-H gel by drying it under an inert atmosphere (inside the dielectric cryostat) at different temperatures (120, 200, 250, 350 ^{o}C) during one hour in order to study the origin of this fast relaxation process. The inert atmosphere is important since it ensures that neither carbonatation nor other reactions occur in the gel [45]. After each drying cycle, a loss spectrum was collected. In Figure IV.9 the result is shown for T = 130 K. From this Figure, it is observed that process 2 and 3 disappear even at the lowest drying temperature (120 ºC). This is an expected behavior since it is generally considered that free water molecules evaporate when heating/drying cementitious materials at 105 ºC [46]. On the contrary, the fastest process (process 1) is still present after drying at very high temperatures (350 ºC). Thus, even if the intensity of process 1 varies with water content it is not likely that its origin is due to motion of water molecules since this fastest relaxation remains also after extensive drying even at high temperatures. As will be discussed below, another origin than the relaxation of water molecules could also explain this small variation of the dielectric strength.

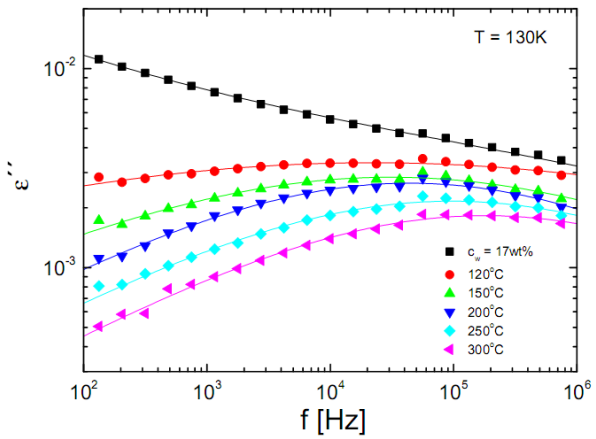

Figure IV**.9.** Loss component (ε″) of the complex dielectric permittivity at 130K, after drying at different temperatures (120, 200, 250, 350°C) during one hour.

From Figure IV.9 it is, furthermore, obvious that the intensity of process 1 is somewhat decreased with increased drying temperature and that the relaxation becomes slightly faster. The calculated activation energy associated with this process is 0.24 ± 0.03 eV, for all the drying temperatures analyzed. The fact that this value is somewhat higher than the corresponding value obtained for the water containing sample (CSH-22) indicates that the water molecules are acting as a plasticizer in the non-dried samples. Thus, even if the origin of process 1 cannot be attributed to a pure water relaxation it seems that the water acts as an amplification of the signal. Therefore, we have to look for other polar groups in our sample, or preferably polar groups at the surfaces of the C-S-H gel to which water can bind (or be released with increasing temperature). The surface of the C-S-H gel contains both silanol (Si-OH) and calcium hydroxide (Ca-OH) groups [45,47–49]. These groups are both polar and have an active dipole moment (1.5 D) comparable to that of the water molecule (1.85 D). As dielectric spectroscopy is probing the fluctuations of dipole moments, our results could thus be an indication on that the fastest process is due to the reorientation of these hydroxyl groups. This view is also supported by the value of the activation energy (0.24eV) founded for this process, which is very close to the energy required to break a single hydrogen bond (0.22 eV) [50]. Such an interpretation is furthermore consistent with an earlier study on high temperature treated silica gel, where a fast process with similar activation energy was attributed to the rotation of surface bonded hydroxyl groups [51]. A similar result was also obtained for water in montmorillonite (hydrated clays) [52]. In addition, studies on dried amorphous polysaccharides (cellulose and dextran) with two and three hydroxyl

groups per ring, respectively, have shown on a weak relaxation similar to the here obtained process 1, however, with a somewhat higher activation energy of 0.33 eV [53]. Intriguingly, a similar fast process with a relatively low value of the activation energy is also found in other systems containing large amounts of hydroxyl groups such as, for instance, MCM-41 and various biological systems [13,14,54,55].

However, even if it cannot be established from the present study that process 1 in C-S-H gel has the same molecular origin as water in various types of hydrophilic confining systems; it is interesting to compare the results with the behavior of water in other types of hydrophilic systems containing large amounts of hydroxyl groups. For instance, in a previous study on D_2O in MCM-41 [56] it was found that water exhibit a crossover from a high temperature VFT to a low temperature Arrhenius behavior, where the low temperature process has about the same activation energy as the here observed process 1. This scenario is thus in agreement with what was found for water in C-S-H gel by analyzing only a limited frequency interval (see Figure IV.5.b)). On the other hand, in a study on water in MCM-41 by dielectric spectroscopy there was no sign of a transition [57]. In that study the fastest dielectric process was shown to follow an Arrhenius temperature dependence in the entire temperature interval where it was observable. Thus, a similar behavior as was found when analyzing the water containing C-S-H gel in a broader frequency interval (see Figure IV.6.b). Moreover, from a study on D_2O in MCM-41 [58] it was suggested that the crossover occurs in the central region of the pores and that the water close to the pore walls does not participate in the transition. This scenario would then be in accordance with our interpretations on surface bonded hydroxyl groups but however in contrast to the results obtained for a copper-based hydrate [59] that showed that it is the relaxation times of water condensed on the surfaces that deviate at low temperatures. Thus, even if it is perfectly clear that process 1 is not due to the relaxation of water itself, we can only speculate about the origin of this process from the present results. More detailed studies are needed to elucidate the origin of the fastest process in C-S-H gel and its possible relation to the fast weak relaxation found in various types of hydrophilic water containing systems.

d. Conclusion

The present dielectric study on the dynamics of water in C-S-H gel shows no sign of the fragile-to-strong transition as previously has been indicated by QENS for a similar system. Instead the apparent crossover in the temperature dependence is here shown to be due to that the analysis is performed in a very limited frequency interval, which, in turn, masks the merging between the main water relaxation and a faster relaxation process. This is also consistent with recent literature data [20–23] on other systems.

When the pore water in C-S-H gel is dried out, it is shown that processes 2 and 3 (both originate from the dynamics of water molecules) disappear whereas the fastest process 1 remains. Due to this, process 1 could be attributed to the non-removable and dielectrically active hydroxyl groups on the surface of the C-S-H gel.

e. References

1. Zhang, Y. *et al.* Observation of dynamic crossover and dynamic heterogeneity in hydration water confined in aged cement paste. *J. Phys. Condens. Matter* **20,** 502101 (2008).

2. Cerveny, S. *et al.* Effect of hydration on the dielectric properties of C-S-H gel. *J. Chem. Phys.* **134,** 034509 (2011).

3. Ball, P. Water as an active constituent in cell biology. *Chem. Rev.* **108,** 74–108 (2008).

4. Debenedetti, P. G. and Stanley, H. E. Supercooled and glassy water. *Phys. Today* **56,** 40–46 (2003).

5. Poole, P. H., Sciortino, F., Essmann, U. and Stanley, H. E. Phase behaviour of metastable water. *Nature* **360,** 324–328 (1992).

6. Mishima, O. and Stanley, H. E. The relationship between liquid, supercooled and glassy water. *Nature* **396,** 329–335 (1998).

7. Liu, L., Chen, S.-H., Faraone, A., Yen, C.-W. and Mou, C.-Y. Pressure Dependence of Fragile-to-Strong Transition and a Possible Second Critical Point in Supercooled Confined Water. *Phys. Rev. Lett.* **95,** 117802 (2005).

8. Mamontov, E. *et al.* Dynamics of water confined in single- and double-wall carbon nanotubes. *J. Chem. Phys.* **124,** 194703 (2006).

9. Chen, S.-H. *et al.* Experimental evidence of fragile-to-strong dynamic crossover in DNA hydration water. *J. Chem. Phys.* **125,** 171103 (2006).

10. Chu, X., Fratini, E., Baglioni, P., Faraone, A. and Chen, S.-H. Observation of a dynamic crossover in RNA hydration water which triggers a dynamic transition in the biopolymer. *Phys. Rev. E* **77,** 011908 (2008).

11. Chen, S.-H. *et al.* Observation of fragile-to-strong dynamic crossover in protein hydration water. *Proc. Natl. Acad. Sci. U. S. A.* **103,** 9012–6 (2006).

12. Sjöström, J., Swenson, J., Bergman, R. and Kittaka, S. Investigating hydration dependence of dynamics of confined water: monolayer, hydration water and Maxwell-Wagner processes. *J. Chem. Phys.* **128,** 154503 (2008).

13. Swenson, J., Jansson, H. and Bergman, R. Relaxation Processes in Supercooled Confined Water and Implications for Protein Dynamics. *Phys. Rev. Lett.* **96,** 247802 (2006).

14. Jansson, H. and Swenson, J. The protein glass transition as measured by dielectric spectroscopy and differential scanning calorimetry. *Biochim. Biophys. Acta* **1804,** 20–6 (2010).

15. Capaccioli, S., Ngai, K. L., Ancherbak, S., Rolla, P. A. and Shinyashiki, N. The role of primitive relaxation in the dynamics of aqueous mixtures, nano-confined water and hydrated proteins. *J. Non. Cryst. Solids* **357,** 641–654 (2011).

16. Grzybowska, K. *et al.* Dynamic Crossover of Water Relaxation in Aqueous Mixtures: Effect of Pressure. *J. Phys. Chem. Lett.* **1,** 1170–1175 (2010).

17. Cerveny, S., Colmenero, J. and Alegría, Á. Dielectric properties of water in amorphous mixtures of polymers and other glass forming materials. *J. Non. Cryst. Solids* **353,** 4523–4527 (2007).

18. Cerveny, S., Colmenero, J. and Alegría, Á. Dynamics of confined water in different environments. *Eur. Phys. J. Spec. Top.* **141,** 49–52 (2007).

19. Cerveny, S., Alegría, Á. and Colmenero, J. Universal features of water dynamics in solutions of hydrophilic polymers, biopolymers, and small glass-forming materials. *Phys. Rev. E* **77,** 031803 (2008).

20. Vogel, M. Origins of Apparent Fragile-to-Strong Transitions of Protein Hydration Waters. *Phys. Rev. Lett.* **101,** 225701 (2008).

21. Doster, W. *et al.* Dynamical Transition of Protein-Hydration Water. *Phys. Rev. Lett.* **104,** 098101 (2010).

22. Pawlus, S., Khodadadi, S. and Sokolov, A. Conductivity in Hydrated Proteins: No Signs of the Fragile-to-Strong Crossover. *Phys. Rev. Lett.* **100,** 108103 (2008).

23. Khodadadi, S., Pawlus, S. and Sokolov, A. P. Influence of hydration on protein dynamics: combining dielectric and neutron scattering spectroscopy data. *J. Phys. Chem. B* **112,** 14273–80 (2008).

24. Nakanishi, M., Griffin, P., Mamontov, E. and Sokolov, A. P. No fragile-to-strong crossover in LiCl-H2O solution. *J. Chem. Phys.* **136,** 124512 (2012).

25. Capponi, S. *et al.* Quasielastic neutron scattering study of hydrogen motions in an aqueous poly(vinyl methyl ether) solution. *J. Chem. Phys.* **134,** 204906 (2011).

26. Busselez, R. *et al.* Component dynamics in polyvinylpyrrolidone concentrated aqueous solutions. *J. Chem. Phys.* **137,** 084902 (2012).

27. Arbe, A. *et al.* Segmental Dynamics in Poly(vinylethylene)/Polyisoprene Miscible Blends Revisited. A Neutron Scattering and Broad-Band Dielectric Spectroscopy Investigation. *Macromolecules* **32,** 7572–7581 (1999).

28. Schönhals, A., Goering, H., Schick, C., Frick, B. and Zorn, R. Glassy dynamics of polymers confined to nanoporous glasses revealed by relaxational and scattering experiments. *Eur. Phys. J. E. Soft Matter* **12,** 173–8 (2003).

29. Brás, A. R. *et al.* Amorphous Ibuprofen Confined in Nanostructured Silica Materials: A Dynamical Approach. *J. Phys. Chem. C* **115,** 4616–4623 (2011).

30. Adam, G. and Gibbs, J. H. On the Temperature Dependence of Cooperative Relaxation Properties in Glass-Forming Liquids. *J. Chem. Phys.* **43,** 139 (1965).

31. Fischer, E., Donth, E. and Steffen, W. Temperature dependence of characteristic length for glass transition. *Phys. Rev. Lett.* **68,** 2344–2346 (1992).

32. Donth, E. The Glass Transition - Relaxation Dynamics in Liquids and Disordered Materials. (2001).

33. Berthier, L. *et al.* Direct experimental evidence of a growing length scale accompanying the glass transition. *Science* **310,** 1797–800 (2005).

34. Schwartz, G. A., Cangialosi, D., Alegría, Á. and Colmenero, J. Describing the component dynamics in miscible polymer blends: towards a fully predictive model. *J. Chem. Phys.* **124,** 154904 (2006).

35. Schwartz, G. A., Alegría, Á. and Colmenero, J. Adam-Gibbs based model to describe the single component dynamics in miscible polymer blends under hydrostatic pressure. *J. Chem. Phys.* **127,** 154907 (2007).

36. Cangialosi, D., Alegría, Á. and Colmenero, J. Dynamical heterogeneity in binary mixtures of low-molecular-weight glass formers. *Phys. Rev. E* **80,** 041505 (2009).

37. Floudas, G. *et al.* Dynamics of polyisoprene in star block copolymers confined in microstructures: A dielectric spectroscopy study. *J. Chem. Phys.* **107,** 5502 (1997).

38. Turky, G., Wolff, D. and Schönhals, A. Confinement Effects on the Molecular Dynamics of Liquid-Crystalline Polymethacrylates-A Broadband Dielectric Spectroscopy Study. *Macromol. Chem. Phys.* **213,** 2420–2431 (2012).

39. Iacob, C. *et al.* Enhanced charge transport in nano-confined ionic liquids. *Soft Matter* **8,** 289 (2012).

40. Cerveny, S., Barroso-Bujans, F., Alegría, Á. and Colmenero, J. Dynamics of Water Intercalated in Graphite Oxide. *J. Phys. Chem. C* **114,** 2604–2612 (2010).

41. Jansson, H. and Swenson, J. Dynamics of water in molecular sieves by dielectric spectroscopy. *Eur. Phys. J. E. Soft Matter* **12 Suppl 1,** S51–4 (2003).

42. Cerveny, S. *et al.* Dielectric Study of Hydration Water in Silica Nanoparticles. *J. Phys. Chem. C* **116,** 24340–24349 (2012).

43. Mamontov, E. *et al.* Suppression of the dynamic transition in surface water at low hydration levels: A study of water on rutile. *Phys. Rev. E* **79,** 051504 (2009).

44. Bertrand, C. E., Liu, K.-H., Mamontov, E. and Chen, S.-H. Hydration-dependent dynamics of deeply cooled water under strong confinement. *Phys. Rev. E* **87,** 042312 (2013).

45. Fonseca, P. C. and Jennings, H. M. The effect of drying on early-age morphology of C–S–H as observed in environmental SEM. *Cem. Concr. Res.* **40,** 1673–1680 (2010).

46. Bordallo, H. N. *et al.* Hindered water motions in hardened cement pastes investigated over broad time and length scales. *ACS Appl. Mater. Interfaces* **1,** 2154–2162 (2009).

47. Ayuela, A. *et al.* Silicate chain formation in the nanostructure of cement-based materials. *J. Chem. Phys.* **127,** 164710 (2007).

48. Rejmak, P., Dolado, J. S., Stott, M. J. and Ayuela, A. 29 Si NMR in Cement: A Theoretical Study on Calcium Silicate Hydrates. *J. Phys. Chem. C* **116,** 9755–9761 (2012).

49. Thomas, J. J., Chen, J. J., Jennings, H. M. and Neumann, D. A. Ca−OH Bonding in the C−S−H Gel Phase of Tricalcium Silicate and White Portland Cement Pastes Measured by Inelastic Neutron Scattering. *Chem. Mater.* **15,** 3813–3817 (2003).

50. Pauling, L. *The Nature of the Chemical Bond and the Structure of Molecules and Crystals: An Introduction to Modern Structural Chemistry*. (1960).

51. Kondo, S. and Muroya, M. The Surface Structure of Silica Gel Studied by Dielectric Dispersion. *Bull. Chem. Soc. Jpn.* **42,** 1165–1170 (1969).

52. Gates, W. P. *et al.* Neutron time-of-flight quantification of water desorption isotherms of montmorillonite. *J. Phys. Chem. C* **116,** 5558–5570 (2012).

53. Montès, H. and Cavaillé, J. Y. Secondary dielectric relaxations in dried amorphous cellulose and dextran. *Polymer (Guildf).* **40,** 2649–2657 (1999).

54. Swenson, J., Jansson, H., Hedström, J. and Bergman, R. Properties of hydration water and its role in protein dynamics. *J. Phys. Condens. Matter* **19,** 205109 (2007).

55. Berntsen, P., Svanberg, C. and Swenson, J. Interplay between hydration water and headgroup dynamics in lipid bilayers. *J. Phys. Chem. B* **115,** 1825–32 (2011).

56. Yoshida, K., Yamaguchi, T., Kittaka, S., Bellissent-Funel, M.-C. and Fouquet, P. Thermodynamic, structural, and dynamic properties of supercooled water confined in mesoporous MCM-41 studied with calorimetric, neutron diffraction, and neutron spin echo measurements. *J. Chem. Phys.* **129,** 054702 (2008).

57. Hedström, J., Swenson, J., Bergman, R., Jansson, H. and Kittaka, S. Does confined water exhibit a fragile-to-strong transition? *Eur. Phys. J. Spec. Top.* **141,** 53–56 (2007).

58. Yoshida, K., Yamaguchi, T., Kittaka, S., Bellissent-Funel, M.-C. and Fouquet, P. Neutron spin echo measurements of monolayer and capillary condensed water in MCM-41 at low temperatures. *J. Phys. Condens. Matter* **24,** 064101 (2012).

59. Yamada, T. *et al.* Quasi-elastic neutron scattering studies on dynamics of water confined in nanoporous copper rubeanate hydrates. *J. Phys. Chem. B* **115,** 13563–9 (2011).

Chapter V
Structure and dynamic of water in C-S-H gel synthesized with nanoparticles

In this chapter we analyze whether dielectric spectroscopy is able to detect changes on water dynamics when changes in the microstructure of C-S-H gel are produced. Changes in the microstructure of C-S-H gel, were produced by adding silica nanoparticles during the synthesis.

We used two types of nanoparticles: colloidal silica (SiO_2) and aminopropyl functionalized silica nanoparticles. Unlike in other studies, here the composites were obtained by adding silica nanoparticles and aminopropyl functionalized silica nanoparticles to C_3S before its hydration reaction. The main motivation for adding functionalized nanosilica is that mechanical properties can be improved. In our particular case, we also want to address the behavior of water confined in the new microstructures formed. Therefore, we need to do a structural study of the synthesized product. After a short introduction, we characterize the materials and we analyze the dynamics of water by means of BDS.

a. Introduction

It is known that the addition of a small amount of silica particles during hydration of cements materials improve its mechanical properties [1–6]. A wide variety of nanoparticles (such as SiO_2, TiO_2, nano-clays, carbon nanotubes and Fe_2O_3 nanoparticles) were added to cement like materials to improve it performance. The addition of colloidal silica (SiO_2) promotes and accelerates the dissolution of C_3S and, therefore a rapid formation of C-S-H phase in cement paste is produced [1]. Nanoparticles also react with CH (i.e. pozzolanic reaction), promoting the increase of C-S-H gel in the cement paste [7–9] and it has been also reported a decreasing of the Ca/Si ratio which benefits the properties of the final product [10]. It is important to note that these processes are affected by both the size and the dispersion of the nanoparticles, being the colloidal dispersions more effective than the powder [11].

Microstructural studies performed by area BET and nuclear magnetic resonance indicated that Portland cement with nano-silica produce a more solid and stable bonding framework [12] due to the formation of denser microstructures through growth of silica chains in C-S-H instead of pozzolanic effects [13]. Moreover, the incorporation of organic moieties inside the C-S-H gel structure could also improve its properties such as mechanical and durability [14,15]. These improves have been studied by many authors, incorporating organic compounds/moieties in the C-S-H gel structure trying to obtain the properties of the organic material as it is seen in natural biocomposites [14–18].

b. Samples – C-S-H gel and C-S-H gel synthesized with nanoparticles

Three different samples were prepared by hydration of C_3S in excess of water:

a) Pure C-S-H gel (CSH),
b) C-S-H gel with commercial silica nanoparticles (CSH-Nyasil),
c) C-S-H with amine functionalized silica nanoparticles (CSH-Stoga).

It is important to remark that the C_3S was added last to the water with the nanoparticles (previously dispersed with an ultrasonic probe) and therefore the pozzolanic and hydration reactions took place at the same time.

The three samples were characterized by TGA (see Figure V.1)) C-S-H gel has a water content (cw, expressed as grams of water/grams of dry solute) of approximately c_w = 21 wt % whereas in the case of CSH-Nyasil and CSH-Stoga the resulting gels had a water content of about c_w = 24 wt %. Immediately after preparation, samples were further dried at 70 ^{o}C in a vacuum oven (this temperature allows water evaporation without structural damage) to reach the same water concentration than ordinary C-S-H sample. Table IV.3 shows the carbonatation and water content for all the three samples analyzed.

Table V.1. Water content (c_w) and carbonatation content (c_{carb}) obtained from the thermo gravimetric curves in Figure V.1.

	C_w [wt%]	C_{carb} [wt%]
C-S-H-22	21.24	7.90
CSH-Nyasil	21.77	2.70
CSH-Stoga	21.25	5.50

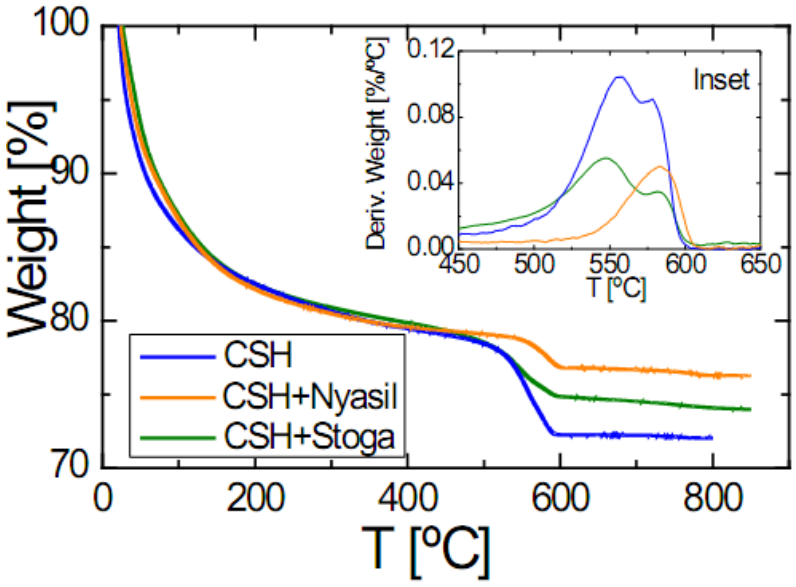

Figure V.1. Thermogravimetric measurements (TGA) of the loss mass up to 800 °C for CSH, CSH-Nyasil and CSH-Stoga. The inset shows the weight derivative plot for the same samples.

c. Structural effect of the addition of nanoparticles on C-S-H gel

We will first discuss the structural aspects observed in all the samples by ^{29}Si MAS-NMR. By this technique, the chemical shift of silicon is determined by the chemical nature of their neighbors. In particular, two different structures are considered: T_n and Q_n structures [19]. *Q*-species represent the silicon atoms bonded to four oxygen atoms whereas *T*-species are the silicone atoms only bond to three oxygen atoms (see a scheme in Figure V.2).

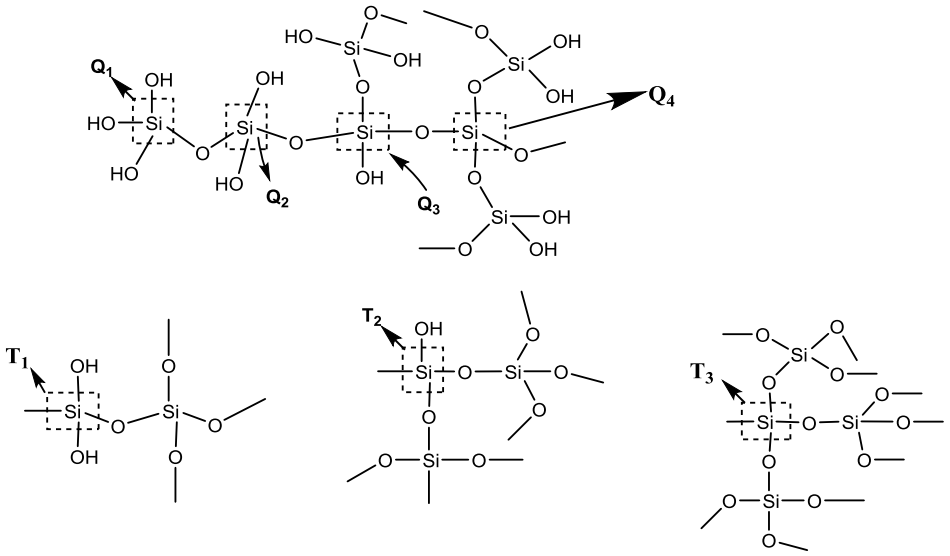

Figure V.2 Schematic representation of a silicate chain to analyze the ^{29}Si NMR for the structure of C-S-H. Q_n (n = 1- to 4) and T_n (n = 1 to 3) species are showed in the pictures.

c.1 ^{29}Si NMR

Figure V.3 shows the NMR spectra for all the samples analyzed. For CSH, the result is similar to that found in previous studies [20–23]. This spectrum shows two chemical shifts at -81.30 (Q_1) and -87.05 (Q_2) ppm respectively. Between Q_1 and Q_2 there is a small shoulder, located at -84.0 ppm (Q_{2B}) which can be only distinguished after deconvolution of the signal. Q_1 has been assigned to the end-chain tetrahedron; Q_2 corresponds to the in-chain tetrahedra and Q_{2B} to the bridging positions of the dreierketten structure (i.e. silicate chains with a period of three tetrahedrons). For CSH-Stoga and CSH-Nyasil, we observe a shift of all the signals to more negative values. This shift is particularly noticeable in the case of CSH-Stoga and it indicates that the degree of silicate polymerization becomes much more important with the addition of amino-propyl functionalized nanoparticles. In addition, the lack of Q_0 in all samples indicates that C_3S in these samples was fully hydrated.

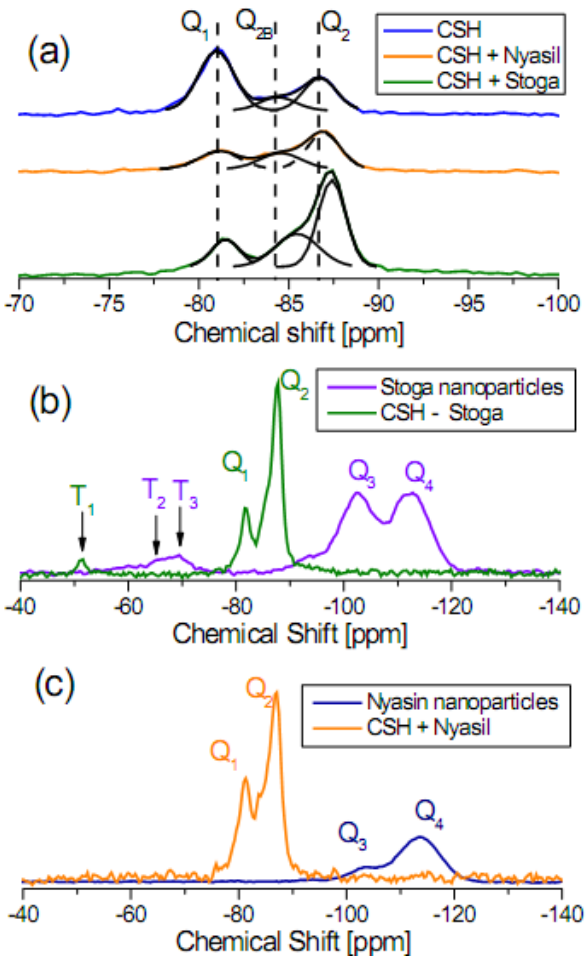

Figure V.3. (a) ^{29}Si NMR spectrum of CSH, CSH-Nyasil and CSH-Stoga. The solid line is the superposition of three peaks for CSH and CSH-Nyasil (Q_1, Q_2 and Q_{2B}) or four peaks for CSH-Stoga. (Q_1, Q_2, Q_{2B} and T_1). ***(b)*** *and* ***(c)***. Comparison between ^{29}Si NMR spectra of Stoga nanoparticles and CSH-Stoga and Nyasil nanoparticles and CSH-Nyasil respectively.

The components of the spectra of C-S-H gels obtained from the deconvolution process are shown in Figure IV.3.and the relative area of each component (Q_1, Q_{2B} and Q_2) is shown in Table V.1. The average degree of connectivity n_c can be calculated by [24]:

$$n_c = \frac{Q_1+2Q_2+T_1}{Q_1+Q_2+T_1} \qquad \text{(V.1)}$$

Similarly, the average chain length L (number of silicates bound together in a chain) is:

$$L = 2\left(1+\frac{Q_2}{Q_1+T_1}\right) \qquad \text{(V.2)}$$

Table V.1 shows the results of both n_c and L. The degree of connectivity and the length of the silicate chains increase with the addition of the nanoparticles being larger in the case of CSH-Stoga. This result is in agreement with previous studies on the effect of the addition of SiO_2 nanoparticles to cement based materials. However, to the best of our knowledge this is the first time this behavior is observed for amino-propyl functionalized silica. Table V.1 also shows an increase in the Q_2/Q_1 ratio in samples with nanosilica which is, once again, bigger for the amino-propyl functionalized particles. It is known that the mean chain length increases with decreasing Ca/Si ratio especially for values below 1.1–1.3[25,26]; therefore this might also be the reason for the formation of longer silicate chains. In addition, the amino-propyl group is highly hydrophilic and this could also have an impact on the gel formation because of rapid hydration compared with Nyasil nanoparticles [27].

Table V.1. Area of Q_1, Q_2, Q_{2B} and T_1 peaks of ^{29}Si NMR spectra in Figure 3a. n_c is the average degree of connectivity, L is the average chain length and C/S represents the Calcium/Silicon ratio obtained by XRF.

Sample	Q_1	Q_{2B}	Q_2	T_1	n_c	L	*Ca/Si*
C-S-H-22	0.58	0.13	0.29	0.00	1.54	3.45	1.30
CSH-Nyasil	0.28	0.25	0.47	0.00	1.72	7.14	0.98
CSH-Stoga	0.16	0.29	0.49	0.06	1.78	9.21	0.96

Now we compare the spectra of bulk nanoparticles with that of CSH-Nyasil (Figure V.3b) and CSH-Stoga (Figure V.3c) respectively. Stoga and Nyasil nanoparticles show two resonances of Q-species (Q_3 ~ -103 ppm and Q_4 ~ -113 ppm) attributed to isolated silanol groups at the surface of silica nanoparticles and Si-O-Si bond in the bulk of the particles respectively. CSH-Stoga and CSH-Nyasil do not show these Q_4 and Q_3 resonances as the Stoga and Nyasil nanoparticles do [28], which indicates that the silica nanoparticles have reacted and have formed 2D silicate chains. In addition, although T_2 and T_3 resonances are present in the spectrum of Stoga particles (T_2 and T_3 correspond to silicon units that contain the organic moiety and condensed with two or three siloxane bonds respectively) they are absent in CSH-Stoga. However, the apparition of T_1 resonance in CSH-Stoga (which does not appear in the Stoga particle spectrum) indicates that the amino-propyl functionalized siloxane groups have incorporated predominantly at the end of the chains. This structural preference of the aminopropyl functionalized silicate tetrahedra has also been observed by Minet et al. at low concentrations of functionalization (trialkoxysilane) [14,29]

c.2 FT-IR

To gain further insight into the nature of the nanoparticle addition in C-S-H gel, we have performed measurements of attenuated-total-reflectance Fourier Transform infrared (ATR-FTIR) at room temperature. The results of the measurements are shown in Figure V.4.

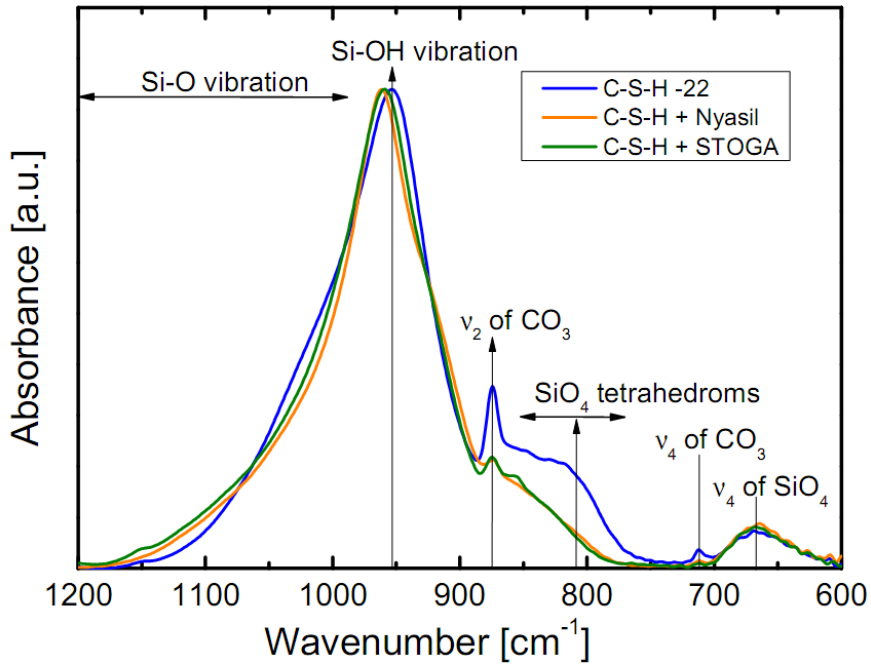

Figure V.4. ATR-FTIR spectra in the range of 1200-600 cm^{-1} of CSH, CSH-Nyasil and CSH-Stoga.

The intense band at 952 cm^{-1} is attributed to the stretching vibrations of Si-O bonds in the tetrahedra of C-S-H gel. This band slightly moves to 959 cm^{-1} in both CSH-Nyasil and CSH-Stoga. The band at 811 cm^{-1} (due to symmetric stretching vibrations of Si-O bonds in C_3S) [30] shifts to 830 cm^{-1} and its intensity decreases for the CSH-Stoga and CSH-Nyasil. This indicates [1] that the presence of nanoparticles accelerates the dissolution of C_3S. The broadband region from 1000 to 1200 cm^{-1} is attributed to the Si-O stretching vibrations. Björnström et al [1], by quantum chemical model calculations, established that for silicates with increasing connectivity (similar to those found in the layered structure of C-S-H gel), the vibrational frequencies of Si-O increase. Deconvoluting the region from 900 to 1150 cm^{-1}, we found that for CSH, two bands at 987 and 950 cm^{-1} are enough to describe the data. By contrast deconvolution of

CSH-Stoga and CSH-Nyasil requires four bands located at 1060, 989, 961, and 921 cm^{-1} respectively. Thus, the band at 987 cm^{-1} of C-S-H slightly shifts to 989 cm^{-1} and, in addition, another band appears at 1060 cm^{-1}. This new band, placed at higher wavenumbers, reflects the fact that the silicate chains are longer in CSH-Nyasil and CSH-Stoga than in the C-S-H. These findings are in agreement with the above results obtained by ^{29}Si NMR.

c.3 XPS

Finally, with the aim of detecting the presence or absence of the amine group in CSH-Stoga, we performed XPS measurements. This technique is sensitive to the presence of a given chemical group based on the binding energy of the emitted photoelectrons. Figure V.5 shows a survey spectrum of CSH-Stoga, whereas the Inset shows the N 1s region. As shown, N 1s signal appears as a single peak located at 399.6 eV, which can be assigned to the C-NH_2 bond. This confirms the existence of this functional group in CSH-Stoga.

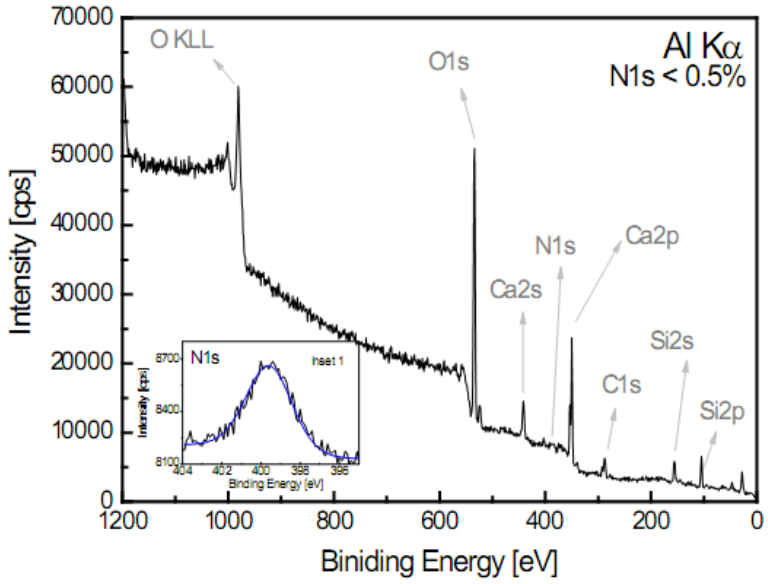

Figure V.5. Survey spectrum of CSH-Stoga acquired by means of XPS. The Inset shows the N 1s region, where the blue line corresponds to the fitting with a single peak centered at 399.6 eV.

In conclusion, the structural study on these materials reveals that the silicate chains of C-S-H gel when the nanoparticles are added during hydration of C_3S, are longer than in the case of ordinary C-S-H gel; being this effect more important in the

case of aminopropyl functionalized nanoparticles. In CSH-Stoga the functionalization of silica particles (-$(CH_2)_3$-NH_2) remains in the C-S-H network (XPS measurements and ^{13}C NMR) and particularly at the ends of the silicate chains of C-S-H gel (presence of T_1 species in ^{29}Si NMR).

Hence, the silicate chains looks as shown in Figure V.6 where we show that the aminopropyl group is grafted onto the end of the silicate chains and even the amino group can establish a hydrogen bond with the silicon in the SiO_4 tetrahedra. In the silicon–oxygen tetrahedron, the central silicon ion has a value of electronegativity lower than oxygen and therefore there is an "electronic appetite" on the silicon atom. Thus, the tetrahedron feels the attraction of the lone pair electrons of the amine, and it approaches causing hydrogen bonding between the oxygen (in the silicon tetrahedron) and the hydrogen atom belonging to the amine as shown in Figure V.6. This also explains the absence of T_2 in the ^{29}Si NMR spectrum of CSH-Stoga.

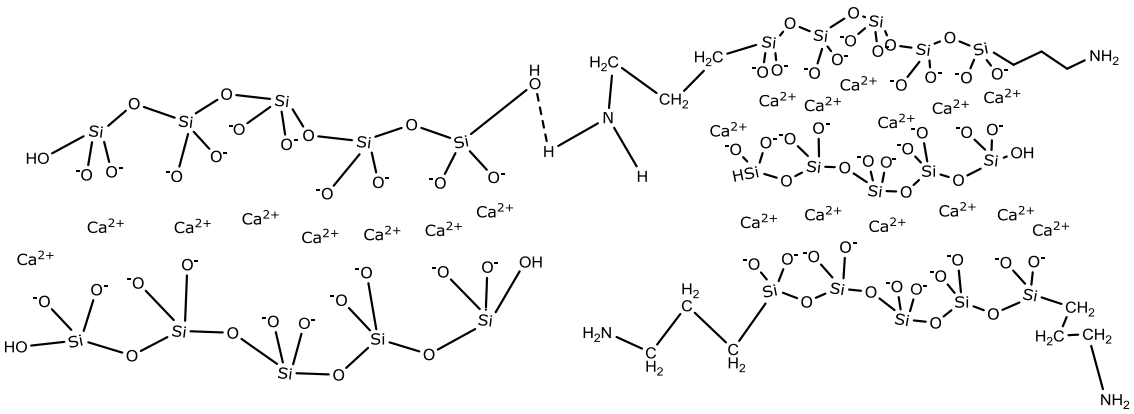

Figure V.6. Proposed structure for CSH-STOGA based on structural results (see text).

c.4 Water dynamics in C-S-H, CSH-Nyasil and CSH-Stoga

Now, we focus on the results of water dynamics confined in the microstructure of the three different samples (C-S-H, CSH-Nyasil and CSH-Stoga) at a water content of 21 wt%. It is known that some calcium silicates react with water to give place to a porous system that evolves during the setting process, from being percolated macro-porous to micro or nano-porous structure [10,31]. Water molecules are an essential part of this structure, being located in different environments (nano-, micro- and macro-pores, chemically bond to cement particles or even free inside the capillary pores). In

general, water molecules in C-S-H gel can be categorized as hydration water and/or confined water.

Figure V.7 shows the comparison of the dielectric response of the three samples at 170 K (panel A) and at 200 K (Panel B). For CSH-Nyasil, we found the same general characteristics as those of C-S-H, i.e., three dielectric processes associated to water confined in the structure. In contrast, CSH-Stoga has a somewhat different dielectric response. In this case, we found the same processes 1 to 3 in well correspondence with the processes visible in C-S-H and CSH-Nyasil. However, between processes 2 and 3 we found an extra relaxation which is labeled as 2*. Thus, the dielectric response of CSH-Stoga shows four different relaxations in this temperature range. All the relaxations in Figure V.7 were fitted using the Cole-Cole functions (see chapter III) for each relaxation process. In both cases the result of the fitting is shown in solid lines.

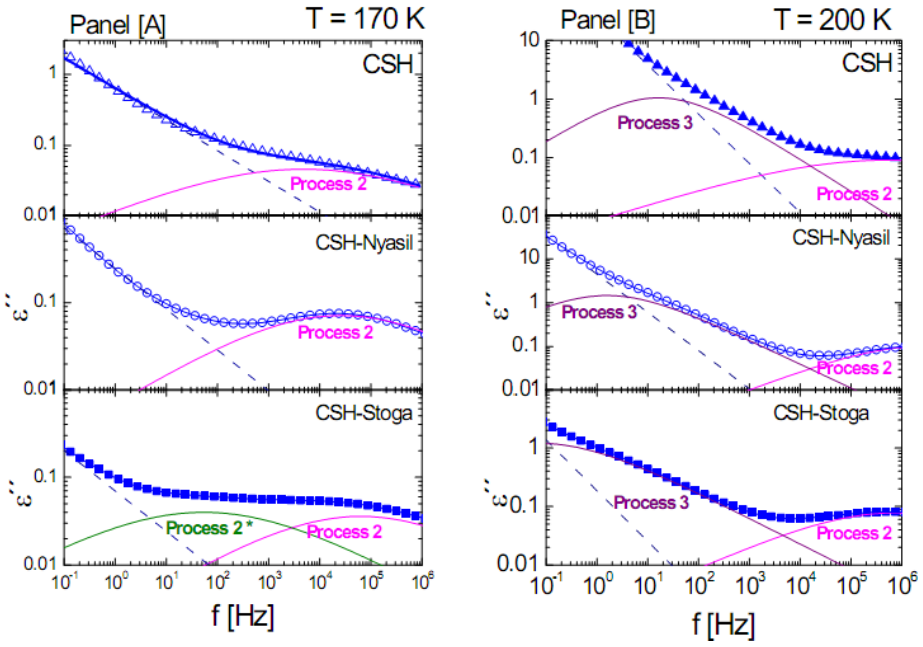

Figure V.7. Frequency-dependent losses of the complex dielectric permittivity, *ε*(f)*, of the sample C-S-H, CSH-Nyasil and CSH-Stoga. Panel [A] at 170 K and Panel [B] at 200K. The solid line through the data points is a least-square fit to a superposition of the imaginary part of one or two Cole–Cole functions respectively for (a) and (b).

Figure V.8 shows the relaxation maps for the three samples. The time scale of the main relaxations 1, 2, and 2* exhibits Arrhenius-type temperature and Table V.2 shows the activation energy of all processes. In contrast, process 3 shows a Vogel-Fulcher-Tamman (VFT) temperature dependence indicating that the nature of both processes (2 and 3) is different.

Table V.2. Activation energy E_a and pre-exponential factor (log (τ_o) corresponding to processes 1, 2 and 2* for data in Figure VI.1.9.

	Process 1		Process 2		Process 2*	
Sample	Log (τ_o(s))	E_a (eV)	Log (τ_o(s))	E_a (eV)	Log (τ_o(s))	E_a (eV)
C-S-H-22	-15.2	0.24	-15.4	0.41	-	-
CSH-Nyasil	-14.7	0.24	-17.7	0.42	-	-
CSH-Stoga	-14.2	0.22	-18.9	0.45	-24.3	0.74

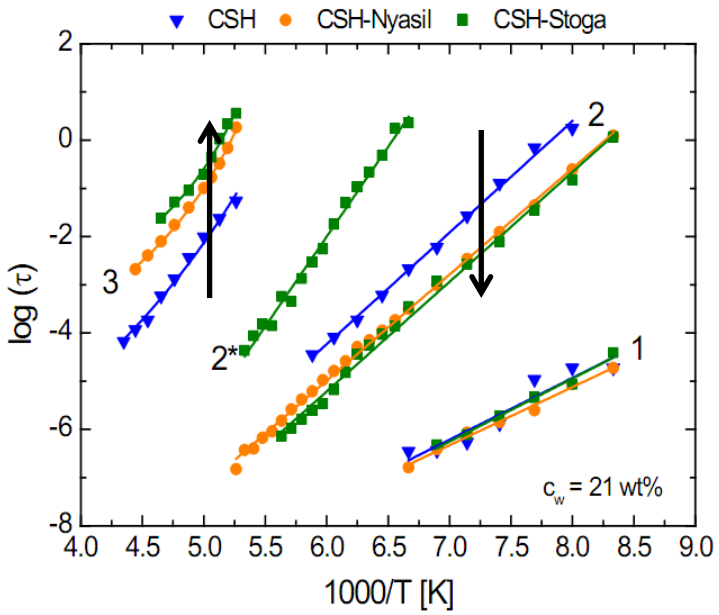

Figure V.8. Temperature dependence of the relaxation time τ (T) for the three samples analyzed at c_w = 21 wt%.

c.4.1 Interpretation of the different processes

In the following, we will discuss each dielectric process separately.

Process 1

The relaxation time of process 1 follows an Arrhenius behavior in the entire temperature range for all the three samples analyzed. The relaxation time of this process does not change with the addition of nanoparticles although the intensity increases in the case of CSH-Nyasil and CSH-Stoga. On average, the activation energy has a value of (0.24 ± 0.20) eV for all the samples. At very low temperatures (130–150 K), it

appears as an excess wing, and therefore it cannot be resolved as a separate peak. In a previous work [32], we showed that the fast process 1 could be attributed to the non-removable and dielectrically active hydroxyl groups on the surface of the C-S-H gel. This view was supported by the value of the activation energy (0.24 eV) which is close to the energy required to break a single hydrogen bond (0.22 eV) [33]. Besides, this structural interpretation is also consistent with the fact that the population of hanging hydroxyl groups increases when the Ca/Si is reduced [22,25], explaining why the intensity of the dielectric signal of CSH-Stoga and CSH-Nyasil is bigger than in C-S-H. In addition, it might be related to a relaxation process that is observed in other systems in which hydroxyl groups are present, such as hydrated clays [34] and hydrated ordinary Portland cement [35].

Process 2

Process 2 was attributed to the relaxation of water extremely confined in small pores (~1 nm), adsorbed on the neighboring calcium silicate sheets. The activation energy is similar for all the three samples, indicating that the environment seen for the water molecules is similar in all the cases and similar to that founded in other aqueous systems at very low water content [36] and supporting that this type of water (observed in process 2) is chemically bound water. Nevertheless, in spite of the fact that all the samples has the same water content, the relaxation time for both CSH-Stoga and CSH-Nyasil becomes faster compared with the water dynamic in C-S-H.

It is well-known that the dynamical behavior of water undergoes variations depending on the type of porous systems where water is confined [35]. For instance, when the pore structure is highly disordered, with a broad pore size distribution and the pores are not completely filled, water-surface interactions are promoted. As a result, water dynamics become faster compared with that in a well-ordered porous system [35]. This is the case of water in C-S-H gel where the nano-porous organization is much distorted and the filling of these nano-pores could not be equally for all the cavities in the sample. Thus, the dynamics of water confined in these small pores is largely in influenced by both the solid–water interface and the distribution of water in this network.

In both CSH-Stoga and CSH-Nyasil, the silicate chains are longer than in ordinary C-S-H and therefore at same water content, water molecules are more scattered in the interlayer space than in C-S-H as schematically show in Figure V.9 (a) and (b). For this reason water dynamics is faster in CSH-Stoga and CSH-Nyasil compared with ordinary C-S-H.

In other words, as the silicate chains are longer and more actives sites for water interactions are available, surface-water interaction are more important than in C-S-H gel and this is compatible with the acceleration of the dynamics. Another implication of this result is that the nano-porous structure in CSH-Nyasil and CSH-Stoga seems to be bigger than in ordinary C-S-H gel.

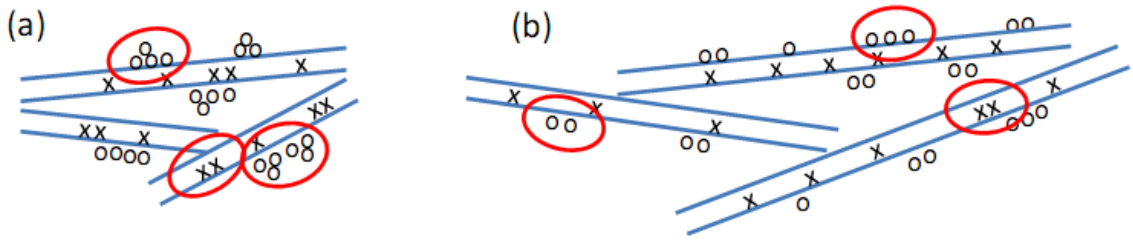

Figure V.9. Representation at nanoscale of molecular water positions. The blue lines represent the C-S-H chain, "x" are interlayer water and "o" are adsorbed water. (a) is shown a typical C-S-H gel structure. (b) shows a C-S-H gel with nanoparticles, with longer C-S-H chains

Process 3

Process 3 is significantly slower than process 2 and therefore it arises from a different population of water molecules. As we previously studied in ordinary C-S-H at different water contents [32,37], this process corresponds with water molecules located in the mesoporous structure of C-S-H gel. These water molecules are forming small clusters (i.e. water molecules connected by more than a single hydrogen bond) and they are involved in cooperative motions, as seen in the non-Arrhenius behavior of the temperature dependence of the relaxation times.

The water dynamics reflected by process 3 becomes slower in CSH-Stoga and CSH-Nyasil compared with that in C-S-H (see Figure V.8). This behavior contrasts with that of process 2, where the dynamics become faster. This is not surprising as these two processes reflect the behavior of water molecules in different environments.

For CSH-Stoga and CSH-Nyasil it has been shown above that the silicate chains are longer than in CSH and therefore a densification of the structure is expected [38] which in turn retards the relaxation of water molecules in the interior of the pore structure. This suggests that the size of the gel pores is on average smaller in CSH-Stoga and CSH-Nyasil than in C-S-H.

Process 2*

Finally, we focus on process 2* which is only observed in CSH-Stoga. The main difference between C-S-H and CSH-Nyasil compared with CSH-Stoga is the presence of the aminopropyl chain in CSH-Stoga. Amines can form hydrogen bonds with each other as well as with water molecules. In addition, the C-S-H solution is alkaline (pH of the order of 11 or 12). At this high pH, it is reasonable to think that the amino group is in its uncharged state as NH_2 as shown by XPS measurements. We think that process 2*, is related with the dynamics associated to the aminopropyl chain enhanced by water. The high activation energy of this process (0.74 eV) indicates that we are not sensing only clusters of water molecules (in such a case, it is expected activation energy of approximately of 0.5 eV [39]).

To probe that, we also measured the dielectric response of the Stoga particles with 10 wt% of water. In this last case, we observe two dynamics: one associated with water molecules on the surface of the particles and a second one similar to that found in CSH-Stoga. Although we need more studies to probe this hypothesis, our results are compatible with the idea that the dynamics of process 2* could be associated with the relaxation of the aminopropyl group enhanced by water molecules.

d. Conclusion

In light of the experiments performed on C-S-H synthesized from C_3S with and without the addition of different types of nanoparticles we can conclude that:

1) The addition of nanoparticles during the synthesis of C-S-H gel increases the length of the silicate chains.
2) In the case of the functionalized nanoparticles, the aminopropyl chain remains in the microstructure of C-S-H gel at the end of the silicate chain as seen by ^{29}Si NMR and XPS measurements.
3) Water dynamics, revealed by BDS, indicate that the microstructure of C-S-H gel changes appreciably with the addition of nanoparticles. These results suggest that in CSH-Stoga and CSH-Nyasil there are more water-surface interactions and smaller gel pores than in C-S-H.
4) BDS can detect changes in water dynamics when structural changes are produced.

e. References

1. Björnström, J., Martinelli, A., Matic, A., Börjesson, L. and Panas, I. Accelerating effects of colloidal nano-silica for beneficial calcium-silicate-hydrate formation in cement. *Chem. Phys. Lett.* **392,** 242–248 (2004).

2. Richardson, I. G. Tobermorite/jennite- and tobermorite/calcium hydroxide-based models for the structure of C-S-H: Applicability to hardened pastes of tricalcium silicate, β-dicalcium silicate, Portland cement, and blends of Portland cement with blast-furnace slag, metakao. *Cem. Concr. Res.* **34,** 1733–1777 (2004).

3. Li, H., Xiao, H., Yuan, J. and Ou, J. Microstructure of cement mortar with nano-particles. *Compos. Part B Eng.* **35,** 185–189 (2004).

4. Qing, Y., Zenan, Z., Deyu, K. and Rongshen, C. Influence of nano-SiO2 addition on properties of hardened cement paste as compared with silica fume. *Constr. Build. Mater.* **21,** 539–545 (2007).

5. Lin, K. L., Chang, W. C., Lin, D. F., Luo, H. L. and Tsai, M. C. Effects of nano-SiO2 and different ash particle sizes on sludge ash-cement mortar. *J. Environ. Manage.* **88,** 708–714 (2008).

6. Yu, R., Spiesz, P. and Brouwers, H. J. H. Effect of nano-silica on the hydration and microstructure development of Ultra-High Performance Concrete (UHPC) with a low binder amount. *Constr. Build. Mater.* **65,** 140–150 (2014).

7. Gaitero, J. J., Sáez de Ibarra, Y., Erkizia, E. and Campillo, I. Silica nanoparticle addition to control the calcium-leaching in cement-based materials. *Phys. status solidi* **203,** 1313–1318 (2006).

8. Jo, B.-W., Kim, C.-H., Tae, G. and Park, J.-B. Characteristics of cement mortar with nano-SiO2 particles. *Constr. Build. Mater.* **21,** 1351–1355 (2007).

9. Gaitero, J. J., Campillo, I., Guerrero, A. and J.J. Gaitero, I. Campillo, A. G. Reduction of the calcium leaching rate of cement paste by addition of silica nanoparticles. *Cem. Concr. Res.* **38,** 1112 (2008).

10. Taylor, H. F. *Cement Chemistry:2nd edition*. *1990*

11. J.J. Gaitero, I. Campillo, P. Mondal, and S. P. S., Gaitero, J. J., Campillo, I., Mondal, P. & Shah, S. P. Small changes can make a great difference. *Transp. Res. Rec. J. Transp. Res. board* **2141,** 1–5 (2010).

12. Shih, J.-Y., Chang, T.-P. and Hsiao, T.-C. Effect of nanosilica on characterization of Portland cement composite. *Mater. Sci. Eng. A* **424,** 266–274 (2006).

13. Porro, A., Campillo, I., Erkizia, E., De Miguel, Y. and Sáez de Ibarra, Y. Effects of Nanosilica Additions on Cement Pastes. in *Design, International Conference on applications of nanotechnology in concrete* 87 (2005).

14. Minet, J. *et al.* Organic calcium silicate hydrate hybrids: a new approach to cement based nanocomposites. *J. Mater. Chem.* **16,** 1379 (2006).

15. Franceschini, A. *et al.* New covalent bonded polymer?calcium silicate hydrate composites. *J. Mater. Chem.* **17,** 913 (2007).

16. Beaudoin, J. J., Dramé, H., Raki, L. and Alizadeh, R. Formation and properties of C-S-H–PEG nano-structures. *Mater. Struct.* **42,** 1003–1014 (2008).

17. Raki, L., Beaudoin, J., Alizadeh, R., Makar, J. and Sato, T. Cement and concrete nanoscience and nanotechnology. *Materials (Basel).* **3,** 918–942 (2010).

18. Sanchez, F. and Sobolev, K. Nanotechnology in concrete – A review. *Constr. Build. Mater.* **24,** 2060–2071 (2010).

19. He, H., Duchet, J., Galy, J. and Gerard, J.-F. Grafting of swelling clay materials with 3-aminopropyltriethoxysilane. *J. Colloid Interface Sci.* **288,** 171–6 (2005).

20. Richardson, I. . The nature of C-S-H in hardened cements. *Cem. Concr. Res.* **29,** 1131–1147 (1999).

21. Jönsson, B., Wennerström, H., Nonat, A. and Cabane, B. Onset of cohesion in cement paste. *Langmuir* **20,** 6702–9 (2004).

22. Ayuela, A. *et al.* Silicate chain formation in the nanostructure of cement-based materials. *J. Chem. Phys.* **127,** 164710 (2007).

23. Kim, J. J., Foley, E. M. and Reda Taha, M. M. Nano-mechanical characterization of synthetic calcium–silicate–hydrate (C–S–H) with varying CaO/SiO2 mixture ratios. *Cem. Concr. Compos.* **36,** 65–70 (2013).

24. Le Saoût, G., Lécolier, E., Rivereau, A. and Zanni, H. Chemical structure of cement aged at normal and elevated temperatures and pressures, Part II: Low permeability class G oilwell cement. *Cem. Concr. Res.* **36,** 428–433 (2006).

25. Cong, X. and Kirkpatrick, R. J. 29Si MAS NMR study of the structure of calcium silicate hydrate. *Adv. Cem. Based Mater.* **3,** 144–156 (1996).

26. Chen, J. J., Thomas, J. J., Taylor, H. F. W. W. and Jennings, H. M. Solubility and structure of calcium silicate hydrate. *Cem. Concr. Res.* **34,** 1499–1519 (2004).

27. Singh, L. P., Karade, S. R., Bhattacharyya, S. K., Yousuf, M. M. and Ahalawat, S. Beneficial role of nanosilica in cement based materials - A review. *Constr. Build. Mater.* **47,** 1069–1077 (2013).

28. Perez, G. *et al.* Effect of self-healing additions on the development of mechanical strength of cement paste. in *Special Issue for International congress on Materials & Structural Stability: Chemistry and Materials Research* 102 (2013).

29. Minet, J. *et al.* New layered calcium organosilicate hybrids with covalently linked organic functionalities. *Chem. Mater.* **16,** 3955–3962 (2004).

30. Yu, P., Kirkpatrick, R. J., Poe, B., McMillan, P. F. and Cong, X. Structure of Calcium Silicate Hydrate (C-S-H): Near-, Mid-, and Far-Infrared Spectroscopy. *J. Am. Ceram. Soc.* **82,** 742–748 (1999).

31. Papatzani, S., Paine, K., Holley, J. A comprehensive review of the models on the nanostructure of calcium silicate hydrates. *Construction and Building Materials* (2015).

32. Monasterio, M., Jansson, H., Gaitero, J. J., Dolado, J. S. and Cerveny, S. Cause of the fragile-to-strong transition observed in water confined in C-S-H gel. *J. Chem. Phys.* **139,** (2013).

33. Pauling, L. *The Nature of the Chemical Bond and the Structure of Molecules and Crystals: An Introduction to Modern Structural Chemistry*. (1960).

34. Kremer, F. and Schönhals, A. *Broadband Dielectric Spectroscopy*. *Springer: Berlin* 729 (2003).

35. Swenson, J. and Cerveny, S. Dynamics of deeply supercooled interfacial water. *J. Phys. Condens. Matter* **033102,** 33102 (2015).

36. Cole, K. S. Dispersion and Absorption in Dielectrics II. Direct Current Characteristics. *J. Chem. Phys.* **10,** 98 (1942).

37. Cerveny, S. *et al.* Effect of hydration on the dielectric properties of C-S-H gel. *J. Chem. Phys.* **134,** 034509 (2011).

38. Valori, A., McDonald, P. J. J. and Scrivener, K. L. L. The morphology of C-S-H: Lessons from 1H nuclear magnetic resonance relaxometry. *Cem. Concr. Res.* **49,** 65–81 (2013).

39. Cerveny, S., Alegría, Á. and Colmenero, J. Universal features of water dynamics in solutions of hydrophilic polymers, biopolymers, and small glass-forming materials. *Phys. Rev. E* **77,** 031803 (2008).

Chapter VI

Natural and Synthetic Tobermorite

Confined water in the slit mesopores of the mineral tobermorite provides an excellent model system to analyze the dynamical properties water confined in cement like materials. In this chapter, we use broadband dielectric spectroscopy (BDS) to analyze the water dynamic entrapped in this crystalline material. Structural characterization is analyzed using ^{29}Si and ^{27}Al NMR, X-ray diffraction and FTIR-ATR. Two samples, one natural and one synthetic, were analyzed (see chapter III) and, despite their similar structure, the motion of confined water in their zeolitic cavity displays considerably different behavior.

a. Introduction

Tobermorite has a double silicate chain between layers of Ca atoms with basal reflections between 9 Å and 14 Å (depending on the water content and Ca/Si ratio) [1]. In natural specimens and promoted by the geological environment, aluminium (Al^{3+}) can substitute for silicon (Si^{4+}) in the bridging or branching tetrahedral (Al-tobermorite, see Figure VI.1) which causes a charge imbalance which is neutralized by the incorporation of cations into interlayer sites [2,3].

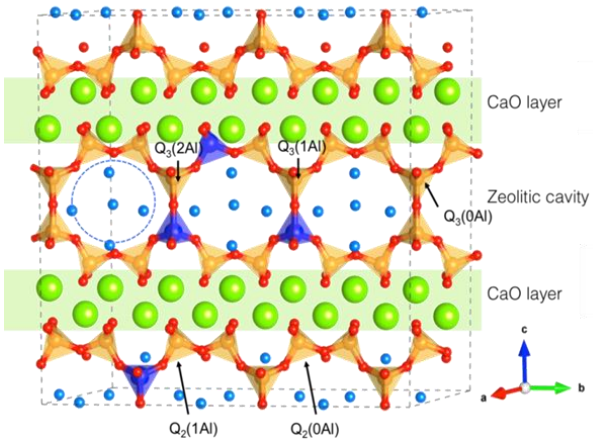

Figure VI.1. Schematic diagram of the Al-tobermorite structure. The Q_n (mAl) sites are also indicated in the figure (n =0-4, m = 0-2, where Q_n are connected via n bridging O atoms to mAl).

Calcium silicate hydrate (C-S-H gel) is the main constituent of cement-based materials, and essentially responsible for cement strength. C-S-H is a nearly amorphous material as seen by X-ray diffraction composed by disordered sheets of oxygen and calcium atoms and silicate chains separated by water [4,5] which locally resemble the structure of tobermorite. Therefore, although tobermorite crystal is an occasional mineral in the nature, it is very relevant for the cement industry and also often used as mineral analogue of the structural characteristics of C-S-H gel [1,6–8]. In fact, according to the colloidal model developed by Jennings [5], the microstructure of the cement paste is composed by a disk-like object (globule) having a layered internal structure similar to tobermorite and jennite.

The microstructure of tobermorite and Al-tobermorite has been studied for a long time and by using different experimental techniques (mainly X-ray diffraction, infrared spectroscopy, nuclear magnetic resonance) [2,9–15]. However, the distribution and dynamics of water in this crystalline material has not been extensively investigated from an experimental point of view. Nevertheless, the increasing interest on understanding it is reflected in the recent studies using molecular simulation. For instance Churakov [16] analyzed the structural position of H_2O molecules and hydrogen bonding in anomalous tobermorite (ab initio MD simulations), Hou and Li [17] studied the structural and dynamical properties of the water/ions at the tobermorite surface, and Bhatt et al [18] studied the diffusion of water in anomalous tobermorite.

b. Samples

Natural (N) and synthetic (S) tobermorites were analyzed at different water contents. The samples were dried in a vacuum oven at 300 °C for 24 hours, and the resulting water content is shown in Table V-1. With further drying, no more water could be extracted. In addition, both samples were hydrated for 2 days at 100% relative humidity. S-tobermorite reaches 11.4 wt%, but there is no water uptake in N-tobermorite. Table VI.1 also shows the identification of the analyzed samples in this work with the Ca/Si ratio and water content after each thermal treatment.

Table VI.1. Identification of the samples. c_w represents the water content in weight (with respect to the dry material), and Ca/Si is the Calcium/Silicon ratio.

Sample	Identification	c_w [wt %]	Ca/Si
Natural Tobermorite – as received	N -10.6 wt%	10.60	0.89
Natural Tobermorite – dried at 300 °C	N -0.12 wt%	0.12	0.89
Synthetic Tobermorite - hydrated	S – 11.4 wt%	11.40	0.82
Synthetic Tobermorite – as received	S – 10.9 wt%	10.90	0.82
Synthetic Tobermorite – dried at 300 °C	S - 4.2 wt%	4.20	0.82
C-S-H [19]	CSH - 9.9 wt%	9.90	1.30

c. Structural characterization of natural and synthetic tobermorite

Figures VI.2.a) and b) shows the X-ray diffraction pattern of both natural (N) and synthetic (S) tobermorite as a function of the *d*-spacing (*d* = distance between consecutive CaO layers) at different water contents. At c_w = 10 wt%, we found an intense reflection at 11.45 and 11.38 Å for N- and S-tobermorite, respectively. This value is the typical basal spacing (or interlayer distance) for tobermorite, which depends on the water content and Ca/Si ratio [1,20]. S-tobermorite has a broader peak than N-tobermorite most likely because of the mixtures of hydrates with different interlayer spacing [20]. In addition, typical reflections of tobermorite at lower *d*-spacing (not shown) were found as discussed in other references [1,9]. When both samples were dried at 300 °C for 24 hours, the interlayer distance decreased to 9.32 and 10.20 Å for N- and S-tobermorite, respectively.

Figure VI.2.c) shows the infrared spectrum (FTIR) of N- and S-tobermorite (10.6 wt% and 10.9 wt%, respectively). The FTIR spectroscopy provides additional information about the functional groups in the internal surface of the samples. The region of 1300-600 cm^{-1} has a complex group of bands that correspond to the vibrations of different Si-O bonds. From the FTIR experiments, it is difficult to distinguish different tobermorite types [21]. However, Vidmer et al [15] as simulated the infrared spectra of tobermorite from first principles to provide a detailed description of each vibrational mode. Table VI.2 shows the position of the peaks in both natural and synthetic tobermorite and the origin of each resonance as analyzed in that reference [15]. The OH stretching region of 3800-3000 cm^{-1} is shown in the inset of Figure

VI.2.c). We observe that the broadband in natural tobermorite is shifted to lower wavenumbers: the maximum shifts from ~3500 cm^{-1} in the synthetic tobermorite to ~3360 cm^{-1} in the natural tobermorite. This shift can indicate that the natural sample has a more crystalline network than the synthetic one (as observed in the SEM images Figure III.11); therefore, the strength of the OH is reduced. In addition, because the water content is similar in both samples (~ 10 wt%), we expect a similar intensity of the infrared signal in this region. However, the band that corresponds to the synthetic tobermorite is more intense that of the natural tobermorite. Note that the hydroxyls from both water molecules and Si-OH and Ca-OH contribute to this signal, which can be the origin of this difference. Finally, the presence of water molecules is also observed in the bending band at ~1640 cm^{-1}. In this case, both bands overlap notably well, which indicates that the differences in the band of 3800-3000 cm^{-1} originate from the different behavior of the hydroxyl groups of Si-OH and Ca-OH and not from water molecules.

Table VI.2. Peaks position in the region of 1300-600 cm^{-1} for natural and synthetic tobermorite. The interpretation of each peak is also indicated and it was taken from reference [15]

Natural Specimen Peak position[cm^{-1}]	Synthetic Specimen Peak position[cm^{-1}]	Origin Reference [15]
1164	1200	Si-O stretching (O-links between bridging tetrahedra)
1024	1058	Si-O stretching (in SiO_2)
987	---	Not reported
954	965	Si-O stretching (O-SiCa, O-Si_2)
878	900	Si-O stretching (OH-SiCa in bridging tetrahedra)
715	725	H_2O librations
671	671	O-Si-O bending, H_2O librations

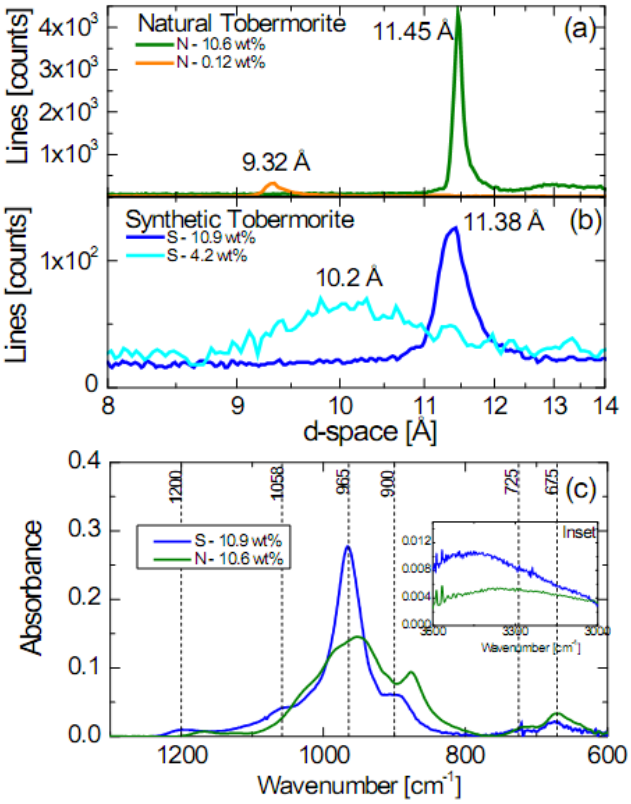

Figure VI.2. (a and b) X-ray diffraction patterns of natural **(a)** and synthetic **(b)** tobermorite as a function of the crystallographic *d*-spacing. The scattering angle *Q* was converted to a crystallographic *d*-spacing. **(c)** ATR-FTIR spectra in the range of 1300-600 cm^{-1} of natural and synthetic tobermorite. Inset: the range of 3800-3000 cm^{-1} is also shown.

Finally, we also analyzed the ^{29}Si NMR of the "as received samples" to identify different connectivity degrees among the silicate tetrahedrals (Q_n (mAl) sites, n =0-4, m = 0-2, where Q_n are connected via n bridging O atoms to mAl; see Figure VI.1 for the identification of Q_n). In addition, ^{27}Al NMR was used to identify the Al coordination structures based on the chemical shifts.

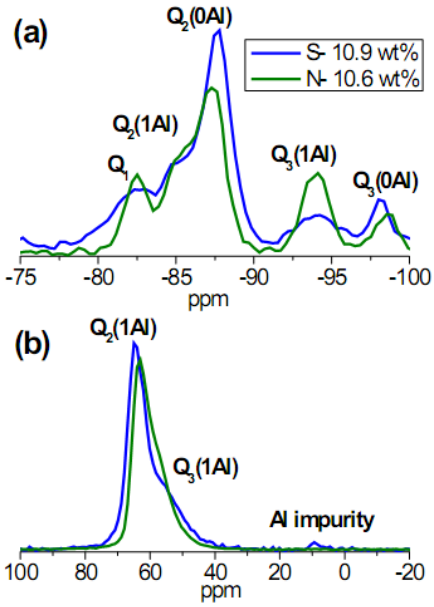

Figure VI.3. (a) Normalized ^{29}Si NMR spectrum of natural and synthetic tobermorite, respectively. Q_1 dimers or chain terminations, Q_2 middle groups, and Q_3 branching sites describe the connectivity of SiO_2 tetrahedral. Figure VI.1 shows a schematic diagram of the types of Q_n. **(b)** ^{27}Al NMR spectrum of natural and synthetic tobermorite.

Figures VI.3.a) and b) show the ^{29}Si NMR and ^{27}Al NMR results. The obtained spectra are analogous to that found in previous studies, although the ^{29}Si NMR resonances are shifted to slightly more negative values most likely because of the substitution of aluminum [2,13,22,23]. Both natural and synthetic tobermorite have notably similar spectra, and the analysis indicates the presence of four resonances, which are assigned to Q_2(0Al), Q_2(1Al), Q_3(1Al) and Q_3(0Al) (see Figure VI.3.a)). This result indicates that aluminum was replaced in the middle (Q_2) and branching (Q_3) sites, which is consistent with the Al content of 5 and 2 % for N- and S-tobermorite, respectively. The ^{27}Al NMR results (Figure VI.3.b)) confirm the presence of two different aluminum environments at ~ 58 and ~64 ppm in the branching (Q_3(1Al)) and bridging (Q_2(1Al)) sites. Both samples also show the Q_1 resonance at ~-82 ppm, which is associated to detectable final chains. Finally, we note that for the synthetic sample, we also found a resonance at 9 ppm in the ^{27}Al NMR spectrum because of [6] Al (octahedral coordination) and the characteristic of Al coordination sites in amorphous Al_2O_3 starting material [24].

d. Dielectric response of natural and synthetic tobermorite

The main objective is to investigate the dynamics of water confined in tobermorite and compare it with that observed in C-S-H gel, which was previously studied [19,25]. The water dynamics were measured at subzero temperatures (100-200 K); therefore, we used differential scanning calorimetry (DSC) measurements to detect any feature in the thermal response of the samples at low temperatures. For all samples (synthetic or natural), there is no water crystallization at low temperatures in the calorimetric response. Therefore, we can assume that water remains amorphous (no ice formation occurs even for the fully hydrated natural tobermorite) at low temperatures for all water contents in this work. Another implication is that the water molecules are confined in the matrix of tobermorite because of the absence of crystallization.

Figure VI.4 shows the imaginary part (ε'') of the complex permittivity at T = 110 K (a) and T = 135 K (b) of S-tobermorite at three different water contents. In Figure VI.4.a), we observe two processes: one at high frequencies (fast process) and one at low frequencies (slow process), which is centered in the frequency window of Figure VI.4.b). The amplitude of these two processes increases with the water content; therefore, both are attributed to water molecules that are confined or interact with the pore walls of tobermorite. Undoubtedly, we detect two different water dynamics, which can be attributed to two different populations of water in synthetic tobermorite.

The dielectric response of natural tobermorite is shown in Figures VI.4.c) and d) for two water contents at T = 110 K (c) and T = 150 K (d). The dielectric response also shows two processes (fast and slow, respectively) for high water content, but the fast process almost vanishes at a notably low water content (c_w = 0.12 wt%). Similar to the case of synthetic tobermorite, the amplitude of these two processes increases with the water content and is also attributed to the presence of water molecules. However, the relaxation strength (intensity) and broadness of both processes differ from that observed in S-tobermorite, which will be discussed in the next section.

The dielectric response of water in tobermorite can be described using standard fit functions as explained in Chapter III. We used the Cole–Cole function [26] to describe each relaxation process.

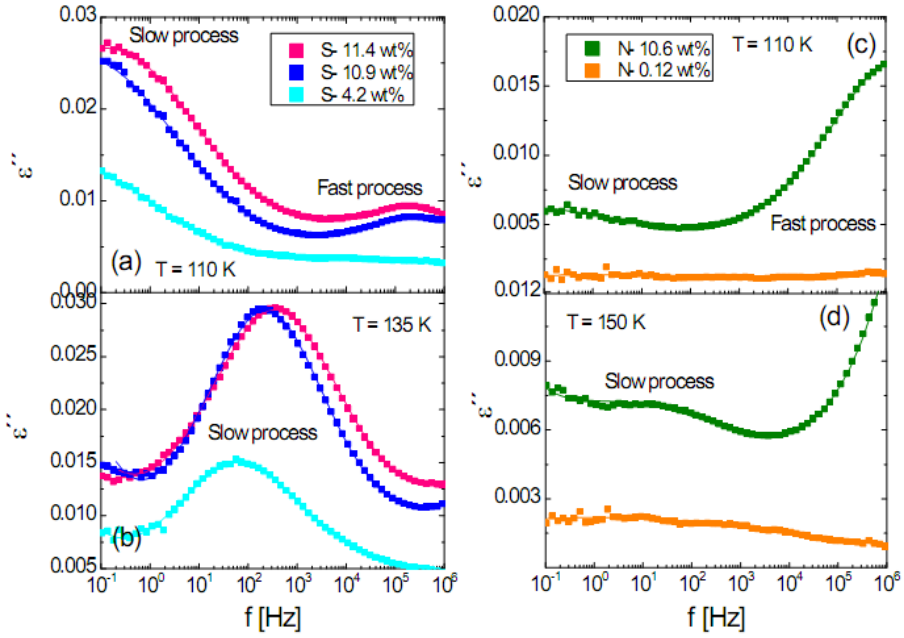

Figure VI.4. Imaginary part (ε'') of the dielectric spectra for water in synthetic tobermorite **(a and b)** at two temperatures (T = 110 K and T = 135K) and different water contents. **(c and d)** Imaginary part (ε'') of the dielectric spectra for water in natural tobermorite at two temperatures ((a) T = 110 K (b) T = 150K) and different water contents. The solid lines through the data points represent the fits to the experimental data.

Figures VI.5.a) and b) shows the temperature dependence of the relaxation times ($\tau = 1/(2\pi f)$, where f is the frequency of the corresponding ε'' maximum that was obtained from the fitting) for all water concentrations. The time scale of the main relaxation exhibits Arrhenius-type temperature dependence in the entire temperature range with a small deviation from this behavior at temperatures above 190 K. This crossover in the temperature dependence of the relaxation time was previously analyzed in several works [27] and will not be discussed in this chapter.

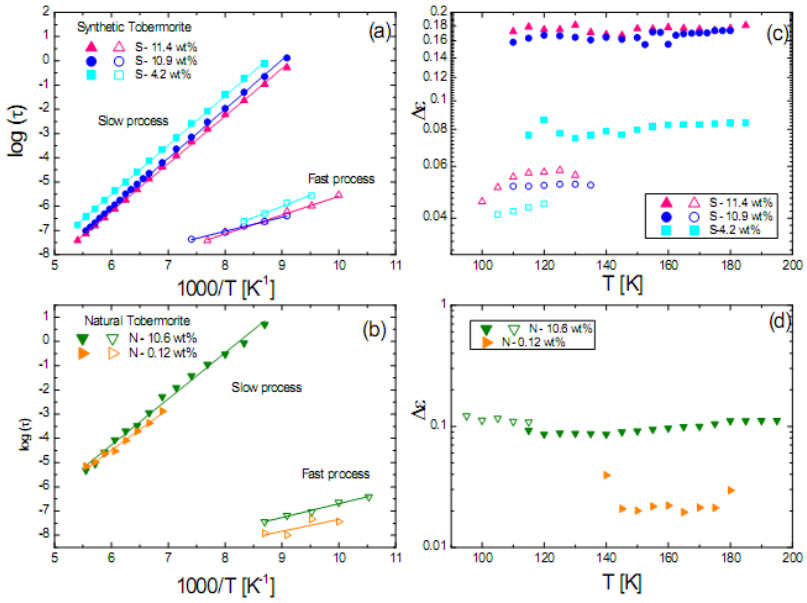

Figure VI.5. a) and b) Temperature dependence of the relaxation times (τ) for water confined in synthetic **(a)** and natural **(b)** tobermorite at different water contents. **(c and d).** Relaxation strength ($\Delta\varepsilon$) for slow and fast processes in **(c)** synthetic and **(d)** natural tobermorite.

The relaxation time of both processes is basically independent of the hydration level (see Figures VI.5.a) and c)) as normally observed in other hard confinements [27–29], and only their relative strengths are affected. Therefore, both processes exhibit the typical behavior of a local relaxation. The relaxation times were fitted to the Arrhenius equation

$$\tau = \tau_0 \exp\left(E_a / kT\right) \qquad \text{(VI.1)}$$

where E_a represents a mean activation energy, k is the Boltzmann's constant, and τ_o is related to a molecular vibration time. The E_a and $\log(\tau_o)$ values are shown in Table VI.3, and these values will be discussed in the next section.

Figure VI.5.c) shows the relaxation strength ($\Delta\varepsilon$) that corresponds to both processes. In both cases, the intensity decreases with temperature as typically for local process [30]. Additionally, the α-values in the CC equation depend on temperature, and it varies approximately from 0.30 at 110 K to 0.60 at 200 K for S-tobermorite and from 0.16 at 110 K to 0.40 at 200 K for N-tobermorite.

Table VI.3. Activation Energy (E_a) and Pre-Exponential Factor (log (τ_o)), which were obtained from the Arrhenius equation that was applied to the data in Figure VI.5.

Sample	Slow Process		Fast process	
	log (τ_0)	E_a [eV]	log (τ_0)	E_a [eV]
S– 11.4 wt%	-18.10	0.39	-13.44	0.16
S– 10.9 wt%	-18.20	0.40	-11.70	0.12
S– 4.2 wt%	-17.70	0.40	-14.21	0.18
N– 10.6 wt%	-15.70	0.38	-12.40	0.11
N -0.12 wt%	-14.70	0.34	12.20	0.10

e. Discussion

e.1 Structural characteristics

As shown in Figure VI.2.a), the intercalation of water in natural tobermorite is evident since the interlaying spacing grows from 9.3 Å (c_w = 0.12 wt%) up to 11.45 Å (c_w = 10.60 wt%). This result is consistent with the behavior of normal tobermorite (the interlayer distance changes to ~9 Å upon heating at 300 ^{o}C) and consequently N-tobermorite can be classified as a normal type. On the other hand, S-tobermorite reaches 10.3 Å after subjected to the same heat treatment and therefore, it is classified as a mixture of normal and anomalous type.

The above results found further confirmation when compared the ATR-FTIR measurements in Figure VI.2.c). Based on the work of Vidmer et al [15], the main difference between normal and anomalous tobermorite takes place in the Si-O stretching region. In particular, the band at 1200 cm^{-1} is much extended in normal (i.e. the peak tends to disappear) than in anomalous tobermorite, where a clear peak is observed. This is what we observed in Figure VI.2.c) where for S-tobermorite we can distinguish a peak at 1200 cm^{-1}, almost absent in N-tobermorite. This also indicates that S-tobermorite is of anomalous type. In addition, in the region from 1300-600 cm^{-1}, natural tobermorite is shifted towards lower wavenumbers compared with that of synthetic tobermorite and therefore, our results indicate [31] some degree of depolymerization of the silicate chains in natural tobermorite (i.e. the silicate chains are longer in the synthetic sample).

Additional structural related information can be extracted from the results of ^{29}Si NMR and ^{27}Al NMR in Figure VI.3. Both tobermorite samples have similar characteristics as seen from NMR.

As above mentioned Al can replace Si in both middle and branching sites of tobermorite structures [32]. The higher intensity of the peak at Q_3(1Al) relative to Q_3(0Al) indicates there is more Al in the bridging sites than in the branching sites for N-tobermorite whereas the opposite behavior is observed for the synthetic sample.

The presence of Q_1 resonance at about -82 ppm suggests that both samples have detectable final chains possibly because the material presents structural disorder. However, the higher intense of the Q_2(0Al) and Q_2(1Al) resonances relative to Q_1 intensity indicates that both samples contains long silicate chains as it corresponds to the crystal.

As a conclusion, we find structural similarities between the two studied samples. Both samples have defects in the tetrahedral chain (substitution of aluminum in the chain middle groups as well as branching sites) and whereas N-tobermorite is of normal type, S-tobermorite is a mixture between normal and anomalous type.

e.2 Dielectric behavior of water in N- and S-tobermorite

Water molecules in Al-tobermorite are situated in the interlaminar pore space interacting with hydroxyls groups or oxygen atoms from the (alumino) silicate chains, with interlaminar cations, or with other water molecules. From the dielectric results, it is evident the presence of two water dynamics in both N- and S-tobermorite with different characteristics. Since dielectric spectroscopy senses the reorientation of permanent dipoles in a given environment by changing the dipole value due to interactions with the host material or even with other dipoles, we expected changes in the dielectric spectrum.

Both tobermorite samples have the substitution of Al^{3+} for Si^{4+} in the silicate chain (see Figure VI.1), yet the quantity of aluminum is considerably higher in N-tobermorite (2.70% wt) than in S-tobermorite (1.05% wt). The charge excess induced

by the Al^{3+} for Si^{4+} substitution is usually compensated by insertion of K^+, Ca^+ or Na^+ cations in the interlayer [33]. Apart from Calcium, our N-tobermorite contains 0.17% (wt) of potassium and 0.16% of magnesium whereas S-tobermorite has 0.13% of magnesium. These cations are present in the cavities where Al is present to compensate the charge imbalance. From analogy with other mesoporous aluminosilicates, as zeolites [34], we hypothesize that water dynamic change when water is located in Al-rich cavities compared to water located in cavities only built by SiO_4.

To test our assumption about the nature of each process (fast and slow) we first compare the relaxation times of water (τ) confined in tobermorite with that observed in the most regular hard confinement systems such as MCM-41 [35] in Figure VI.6. Focus on the behavior of τ at low temperatures (below 200 K), both the activation energy and the relaxation time are almost independent of the system [27] and hence, this low-temperature process can be regarded as a universal water relaxation (see colored region in Figure VI.6). The typical activation energy of the universal β-relaxation of confined water is around 0.50 eV [36]. The relaxation times of water confined in tobermorite are faster than the universal one (Figure VI.6) and the activation energy decreases to ~ 0.40 eV. This is typical for the dynamic of water molecules with a strong dependence on the host material, and/or for water confined in a highly disordered porous system [27,29]. In tobermorite, the zeolitic cavities have an approximated diameter of half a nanometer, where about 5 water molecules must pack. Hence, the water-solid interaction must be considerably more important than the water-water interaction. Therefore, we can conclude that water molecules in N- and S-tobermorite are more strongly affected by "surface" interactions than in MCM-41. In addition, and despite tobermorite is a crystalline material, the such a strong confinement implies that the hydrogen bond network of water in tobermorite is not fully developed, similarly to what one could expect from a disorder porous system. This two facts together, namely the strong interaction between the water molecules and the substrate and the scarce hydrogen bond network, are the main reasons to obtain lower activation energy (0.40 eV) compared with that obtained for water in other well-defined and homogeneous confinement systems (0.5 eV) where relevant water-water interactions takes place. For instance, a low value of E_a is typical of water solutions at low water content where interactions between the water molecules and the solute are expected [37].

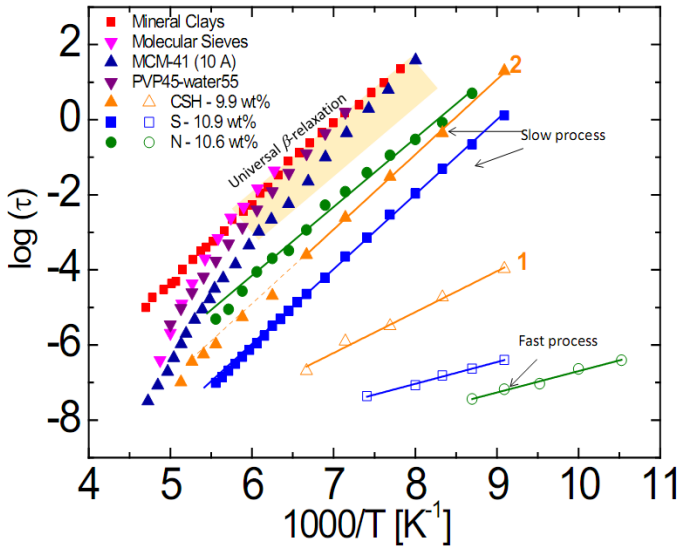

Figure VI.6. Temperature dependence of the universal β-relaxation times of water in different hard confinement systems: vermiculite clay [38], molecular sieves [39], MCM-41 (21 Å) [35] and Poly(vinyl pyrrolidone, PVP) at high water content [37] (see shadow area). In addition, the relaxation times of the slow and fast processes in Al-tobermorite and that in C-S-H-gel [19] are displayed.

In addition to insight gained from the relaxation times, we can extract important information from the dielectric strength (the intensity of the process) which measures the number of dipoles relaxing in the dielectric process [40]. Figure VI.7 shows the comparison between the permittivity of N- and S-tobermorite at 110 K. Clearly, for the fast process the intensity of N-tobermorite is bigger than that in S-tobermorite, indicating that more water dipoles are involved in the fast process of N-tobermorite. The Al content in N-tobermorite is almost triple than in S-tobermorite and therefore we can assume that the slow process is due to water confined in the zeolitic cavities rich in Al. In addition, the "slow process" is closer to the universal relaxation of confined water than the "fast process" (see Figure VI.6) and also similar to water around silica particles [28] where the interaction between the host and water is produced through silanol groups. Therefore, it is expected that the "slow process" arises from the motion of water molecules confined in silicon rich cavities. The relaxation strength (Figure VI.7) also indicates that there are more dipoles associated to this relaxation in S-tobermorite than in N-tobermorite and this fact agrees with a major number of cavities constructed by SiO_4 in S-tobermorite.

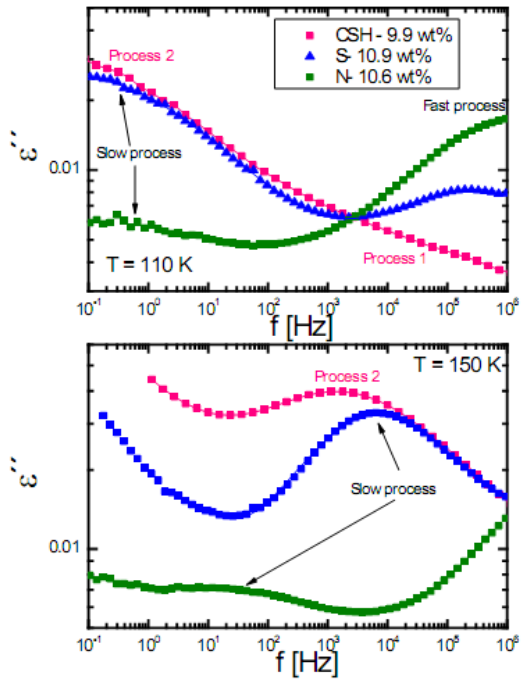

Figure VI.7. Comparison of ε'' for water confined in N- and S-tobermorite and C-S-H gel [19] at $c_w \sim 10$ wt% and at two temperatures (a) T = 110 K and (b) T = 150 K. Two processes are observed in all the samples. In the case of C-S-H gel these processes were labeled [19] as "1 and 2".

Finally, we wonder why the relaxation times are so different (5 orders of magnitude in Figure VI.6) in these two distinct cavities. According to the wait-and-switch model [41], the relaxation time is controlled by the time for which a water molecule has to wait until a new partner is available to establish a strong interaction by a rotational movement. The presence of Al and the associated counterion provide those suitable sites; in addition, anions and cations become surrounded by clusters of water molecules and hydrogen-bonds are formed between them. As a result, the relaxation time is faster compared with a breaking of a hydrogen bond between two water molecules in silanol rich-cavities. In agreement with this view, the potential barrier for reorientational motions (E_a value, table VI.3), is lower for the fast process (~0.15 eV) compared with that of the slow process (~0.40 eV) which is consistent with the above view.

As a conclusion, Al-substituted tobermorite has two different types of water populations, according to their relaxation times. The SLOW dielectric processes observed for water in tobermorite represents the dynamics of water molecules in

siliceous zeolitic cavities (built solely by SiO_4 tetrehedra) and the FAST dynamics of water molecules in aluminum rich zeolitic cavities (built of both SiO_4 and AlO_4 tetrahedra).

e.3 Comparison of water dynamics in C-S-H gel

In the chapter IV, we investigated the rotational properties of water molecules confined in C-S-H gel of different water contents (from 6 to 15 wt%) by BDS. The studied C-S-H gel had a Ca/Si ratio of 0.89, which is slightly higher of 0.82 in tobermorite samples, and a greater structural disorder as the X-ray diffraction reflected. For C-S-H gel in the temperature region of 100 – 200 K, we found two relaxation processes (labeled 1 and 2, see Figure VI.6) each one related with different environments for the water molecule confined in this material. Process 2 observed in C-S-H gel was associated [19] with the relaxation of water molecules located in gel pores, whereas process 1 was related [25] with the rotation of some intrinsic hydrated dipolar group (hydroxyl groups) in the internal surface of C-S-H gel. This view was supported by the value of the activation energy (0.24 eV), which is very close to the energy required to break a single hydrogen bond (0.22 eV) [41]. We wonder whether these two processes (1 and 2) are related with the fast and slow processes observed in tobermorite.

Figure VI.6 shows the relaxation time of C-S-H gel at c_w = 9.9 wt%, an amount of water similar to that analyzed for tobermorite in this work. It is obvious in Figure VI.6 that the relaxation time of process 2 (water in gel pores) is similar to that of the "slow process" in tobermorite. Even more, the activation energy is the same in both samples (~0.40 eV) which implies that both processes arise from the same relaxation mechanism. This strongly suggests that water molecules in C-S-H gel relax in small cavities similar to that in tobermorite. By contrast, process 1 in C-S-H gel is somehow different of the "fast process" in tobermorite (figure VI.6). We attribute the fast process in tobermorite to the relaxation of water molecules in Al rich cavities, but the C-S-H analyzed had only 0.13 % of Al_2O_3 as observed in the fluorescence experiment. One option is that also in C-S-H we are sensing the relaxation of water molecules in the solvation shell of Al cations. The low intensity of the process 1 observed in C-S-H gel is in agreement with this interpretation [25] although the relaxation time is 2 decades

slower in C-S-H gel. To determine the origin of this process, C-S-H with different Al content should be analyzed.

Finally, Figure VI.7 compares the permittivity measured for C-S-H gel, S-tobermorite, and N-tobermorite at two temperatures. The similarities between the slow process in S-tobermorite and process 2 in C-S-H are noticeable in the high frequency side indicating that faster water dipoles relax in a similar way in both samples. However, the dielectric response of water in C-S-H is broader (α-parameter in eq. VI.1)) than that observed in S-tobermorite. This is because the water molecules in C-S-H gel are confined in a highly heterogeneous environment [42] compared with that in crystalline tobermorite, where the cavities are more regular.

f. Conclusions

In this chapter the properties of confined water in the zeolitic cavity of tobermorite were analyzed by broadband dielectric spectroscopy. Despite tobermorite minerals are rare in nature; they are excellent models to study the more complex C-S-H gel, the main component of cement and responsible of its excellent mechanical performance.

Two tobermorite samples were investigated, a natural one and a synthetic one. The structure of these minerals was characterized using X-ray, ATR-FTIR and NMR spectroscopies determining that both belong to the 11Å variety. The BDS results reveal two different water relaxation dynamics, with a considerable different relative weight in the natural and synthetic minerals, despite their matching structures. We attribute the difference to the higher Al content in the natural specimen, which strongly affects water dynamics. Such a deep impact of aluminum impurities on the water dynamics could be of vital importance to understand ion migration and chemical degradation of fly-ash and slag Al-rich cements.

In addition, we have compared the dielectric response of water in tobermorite and in the C-S-H gel. The porous structure in the C-S-H is more heterogeneous than that in tobermorite and therefore the dielectric signal is different (Figure VI.7). This is

particular marked on the low frequency side (the slower dipolar reorientation). Conversely, the faster water molecules, relax in a similar way for C-S-H and tobermorite.

g. References

1. Richardson, I. G. Tobermorite/jennite- and tobermorite/calcium hydroxide-based models for the structure of C-S-H: Applicability to hardened pastes of tricalcium silicate, β-dicalcium silicate, Portland cement, and blends of Portland cement with blast-furnace slag, metakao. *Cem. Concr. Res.* **34,** 1733–1777 (2004).

2. Komarneni, S. *et al.* 27Al and 29Si magic angle spinning nuclear magnetic resonance spectroscopy of Al-substituted tobermorites. *J. Mater. Sci.* **20,** 4209–4214 (1985).

3. Komarneni, S., Breval, E., Miyake, M. and Roy, R. Cation-exchange properties of (Al plus Na)-substituted synthetic tobermorites. *Clays Clay Miner.* **35,** 385–390 (1987).

4. Jennings, H. M. A model for the microstructure of calcium silicate hydrate in cement paste. *Cem. Concr. Res.* **30,** 101–116 (2000).

5. Jennings, H. M. Refinements to colloid model of C-S-H in cement: CM-II. *Cem. Concr. Res.* **38,** 275–289 (2008).

6. Ridi, F., Luciani, P., Fratini, E. and Baglioni, P. Water confined in cement pastes as a probe of cement microstructure evolution. *J. Phys. Chem. B* **113,** 3080–7 (2009).

7. Scrivener, K. L. and Nonat, A. Hydration of cementitious materials, present and future. *Cem. Concr. Res.* **41,** 651–665 (2011).

8. Papatzani, S., Paine, K. and Holley, J. A comprehensive review of the models on the nanostructure of calcium silicate hydrates. *Construction and Building Materials* (2015).

9. Sugama, T., Kukacka, L. E. and Horn, W. Effects of tobermorite and calcium silicate hydrate (I) crystals formed within polymer concretes. *J. Mater. Sci.* **16,** 345–354 (1981).

10. Merlino, S., Bonaccorsi, E. and Armbruster, T. The real structure of tobermorite 11 angstrom: normal and anomalous forms, OD character and polytypic modifications. *Eur. J. Mineral.* **13,** 577–590 (2001).

11. Mostafa, N. Y., Shaltout, A. A., Omar, H. and Abo-El-Enein, S. A. Hydrothermal synthesis and characterization of aluminium and sulfate substituted 1.1nm tobermorites. *J. Alloys Compd.* **467,** 332–337 (2009).

12. Biagioni, C., Bonaccorsi, E., Merlino, S. and Bersani, D. New data on the thermal behavior of 14Å tobermorite. *Cem. Concr. Res.* **49,** 48–54 (2013).

13. Tränkle, S. *et al.* Conventional and microwave assisted hydrothermal syntheses of 11 Å tobermorite. *J. Mater. Chem. A* **1,** 10318 (2013).

14. Mogami, Y. *et al.* Hydrogen cluster/network in tobermorite as studied by multiple-quantum spin counting 1H NMR. *Cem. Concr. Res.* **66,** 115–120 (2014).

15. Vidmer, A., Sclauzero, G. and Pasquarello, A. Infrared spectra of jennite and tobermorite from first-principles. *Cem. Concr. Res.* **60,** 11–23 (2014).

16. Churakov, S. V. Structural position of H2O molecules and hydrogen bonding in anomalous 11A?? tobermorite. *Am. Mineral.* **94,** 156–165 (2009).

17. Hou, D. and Li, Z. Molecular dynamics study of water and ions transport in nano-pore of layered structure: A case study of tobermorite. *Microporous Mesoporous Mater.* **195,** 9–20 (2014).

18. Bhatt, J. S., McDonald, P. J., Faux, D. a., Howlett, N. C. and Churakov, S. V. NMR relaxation parameters from molecular simulations of hydrated inorganic nanopores. *Int. J. Quantum Chem.* **114,** 1220–1228 (2014).

19. Cerveny, S. *et al.* Effect of hydration on the dielectric properties of C-S-H gel. *J. Chem. Phys.* **134,** 034509 (2011).

20. Richardson, I. G. Model structures for C-(A)-S-H(I). *Acta Crystallogr. B. Struct. Sci. Cryst. Eng. Mater.* **70,** 903–23 (2014).

21. Yu, P., Kirkpatrick, R. J., Poe, B., McMillan, P. F. and Cong, X. Structure of Calcium Silicate Hydrate (C-S-H): Near-, Mid-, and Far-Infrared Spectroscopy. *J. Am. Ceram. Soc.* **82,** 742–748 (1999).

22. Maeshima, T., Noma, H., Sakiyama, M. and Mitsuda, T. Natural 1.1 and 1.4 nm tobermorites from Fuka, Okayama, Japan: Chemical analysis, cell dimensions, 29Si NMR and thermal behavior. *Cem. Concr. Res.* **33,** 1515–1523 (2003).

23. Faucon, P. *et al.* Aluminum Incorporation in Calcium Silicate Hydrates (C-S-H) Depending on Their Ca / Si Ratio. *J. Phys. Chem. B* **103,** 7796–7802 (1999).

24. Hill, M. R., Bastow, T. J., Celotto, S. and Hill, A. J. Integrated Study of the Calcination Cycle from Gibbsite to Corundum. *Chem. Mater.* **19,** 2877–2883 (2007).

25. Monasterio, M., Jansson, H., Gaitero, J. J., Dolado, J. S. and Cerveny, S. Cause of the fragile-to-strong transition observed in water confined in C-S-H gel. *J. Chem. Phys.* **139,** (2013).

26. Cole, K. S. Dispersion and Absorption in Dielectrics II. Direct Current Characteristics. *J. Chem. Phys.* **10,** 98 (1942).

27. Swenson, J. and Cerveny, S. Dynamics of deeply supercooled interfacial water. *J. Phys. Condens. Matter* **033102,** 33102 (2015).

28. Cerveny, S. *et al.* Dielectric Study of Hydration Water in Silica Nanoparticles. *J. Phys. Chem. C* **116,** 24340–24349 (2012).

29. Cerveny, S., Barroso-Bujans, F., Alegría, Á. and Colmenero, J. Dynamics of Water Intercalated in Graphite Oxide. *J. Phys. Chem. C* **114,** 2604–2612 (2010).

30. Ngai, K. L. *Relaxation and diffusion in complex systems (partially ordered systems)*. 650 (2011).

31. Björnström, J., Martinelli, A., Matic, A., Börjesson, L. and Panas, I. Accelerating effects of colloidal nano-silica for beneficial calcium-silicate-hydrate formation in cement. *Chem. Phys. Lett.* **392,** 242–248 (2004).

32. Manzano, H., Dolado, J. S. and Ayuela, A. Aluminum incorporation to dreierketten silicate chains. *J. Phys. Chem. B* **113,** 2832–9 (2009).

33. Tsuji, M., Komarneni, S. and Malla, P. Substituted Tobermorites: 27Al and 29Si MASNMR, Cation Exchange, and Water Sorption Studies. *J. Am. Ceram. Soc.* **74,** 274–279 (1991).

34. Coudert, F.-X., Cailliez, F., Vuilleumier, R., Fuchs, A. H. and Boutin, A. Water nanodroplets confined in zeolite pores. *Faraday Discuss.* **141,** 377–98; discussion 443–65 (2009).

35. Sjöström, J., Swenson, J., Bergman, R. and Kittaka, S. Investigating hydration dependence of dynamics of confined water: monolayer, hydration water and Maxwell-Wagner processes. *J. Chem. Phys.* **128,** 154503 (2008).

36. Cerveny, S., Alegría, Á. and Colmenero, J. Universal features of water dynamics in solutions of hydrophilic polymers, biopolymers, and small glass-forming materials. *Phys. Rev. E* **77,** 031803 (2008).

37. Cerveny, S., Alegría, Á. and Colmenero, J. Broadband dielectric investigation on poly(vinyl pyrrolidone) and its water mixtures. *J. Chem. Phys.* **128,** 044901 (2008).

38. Bergman, R. and Swenson, J. Dynamics of supercooled water in confined geometry. *Nature* **403,** 283–6 (2000).

39. Jansson, H. and Swenson, J. Dynamics of water in molecular sieves by dielectric spectroscopy. *Eur. Phys. J. E. Soft Matter* **12 Suppl 1,** S51–4 (2003).

40. Kremer, F. and Schönhals, A. *Broadband Dielectric Spectroscopy*. *Springer: Berlin* 729 (2003).

41. Kaatze, U., Behrends, R. and Pottel, R. Hydrogen network fluctuations and dielectric spectrometry of liquids. *J. Non. Cryst. Solids* **305,** 19–28 (2002).

42. Manzano, H. *et al.* Confined water dissociation in microporous defective silicates: mechanism, dipole distribution, and impact on substrate properties. *J. Am. Chem. Soc.* **134,** 2208–15 (2012).

Chapter VII

Water dynamics confined in Ordinary Portland cement of different water-to-cement ratio

As mentioned in the Chapter I, Portland cement (OPC) is the most common type of cements because more than 1 m^3 is produced per person worldwide [1]. Portland cement consists of at least two-thirds by mass of calcium silicates (3 $CaO{\cdot}SiO_2$ and 2 $CaO{\cdot}SiO_2$) and the rest consists of aluminum- and iron-containing phases and other crystalline compounds. During hydration several chemical and physical reactions take place to obtain a product with an immense complexity formed by different crystalline phases and other hydration products [2]. All these crystalline products are glued by a semi-crystalline material called C-S-H gel also produced during the hydration. The structure of the products formed during hydration contains several pores of different shapes and sizes. These pores also evolve from a macro-porous structure to a nano-porous structure. The water molecules remain in the final product as a structural part of all these components. Moreover, some properties of cements such as shrinkage, creep, or durability [3] were attributed to the water confined on the structure of cement materials. Consequently, water is a vital component of the cement structure [2,4].

In this chapter we analyze the dielectric response of Portland cement at different water-to-cement ratio. From our results it is evident that the dielectric response is complex with several relaxations. Although the complete picture is still not fully understood, we think it is worth to show these results in the framework of this thesis.

a. Introduction

In the previous chapters, we have studied the dynamics of water confined in C-S-H In these previous studies [5,6], we observed 3 different water relaxation related to: 1) water molecules located in pore structure of C-S-H gel (processes 2 and 3) and 2) the rotation of hydroxyl groups on the internal surfaces of C-S-H (process 1) (see Figure IV.2). Now we focus on the water dynamics in hydrated cement at different *w/c* ratio.

In addition to gel pores in C-S-H gel, cements also have capillary pores (also called macropores or mesopores) which are due to empty spaces after the hydration reaction takes place. Regardless of the model considered, the structure of both C-S-H gel and cements is highly complex and comprises pores of different sizes in which water molecules can be located.

The *w/c* ratio not only affects at the water dynamics related with the water. It can also modify strongly the percentage of capillary pores in the cement samples [7]. Thus, we prepared samples with different *w/c* ratio to study its influence in the different processes obtained from the cement. In addition, increasing the *w/c* ratio increases the total porosity of cement samples and also the hydration degree [8]. As a consequence, *w/c* ratio controls final strength and the durability as well as workability of cements.

b. Samples

Samples were prepared as explained in Chapter III. Figure VII.1 shows the calorimetric response of Portland cement at different *w/c*. During the cooling, two different thermal features, at ~ 239 K, and ~ 225 K are shown for the water confined in cements at different *w/c* ratio. These values are close to the values reported by Snyder and Bentz [9] for Portland cement at different *w/c* ratio and also for Ridi et al for white cement [10] after 28 days of hydration. Since a depression of the freezing point of water is known to occur for water in confining geometries, these temperatures can be considered to reflect the sizes of pores in the materials. The lowest crystallization temperature (~ 225 K) can be associated with crystallization of water in pores of few nanometers wide whereas the highest crystallization temperature should be associated to freezing of water in larger pores.

The intensity of the peaks is highly dependent on the *w/c* ratio; the lower the *w/c* ratio is (i.e. lower water content), the lower is the intensity of the peaks. In general, it is expected that a higher *w/c* ratio results in a smaller fraction of smaller pores (gel pores, 1-10 nm) and larger fraction of capillary pores, which is the reason for a lower strength and a higher permeability [2] compared to materials with lower water content. Thus in case of the sample *w/c* = 0.4 the porosity should be higher than in the sample of *w/c* =

0.3, which is also in agreement with the increase in intensity of the peaks in the calorimetric response.

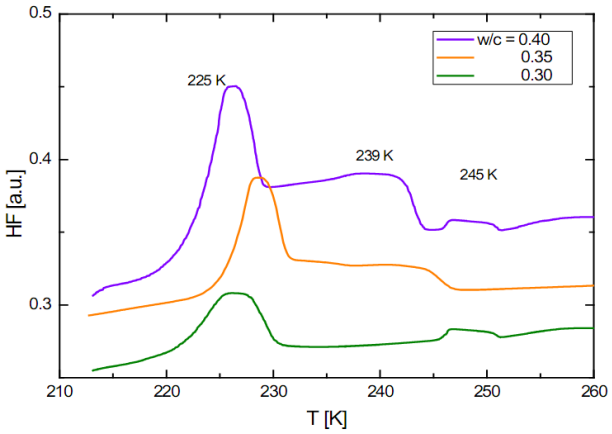

Figure VII.1. Heat flow measured by DSC during cooling at a rate of 10 K/min for different *w/c* ratio, as indicated in the figure. Crystallization is observed at different temperatures according to the size of the cavity.

c. Dielectric response of Portland cement

The dielectric experiments were performed from the lowest (110 K) to the highest (250 K) temperature. Therefore in our samples, amorphous and crystalline water coexists as previously explained. Figure VII.2 (a and b) shows the imaginary part (ε'') of the complex permittivity at different temperatures for *w/c* = 0.4 (samples at a different *w/c* ratio show a similar dielectric response). We observe the presence of different dielectric processes whose maximum shifts to higher frequency with increasing temperature. In addition, Figure VII.2 (c and d) shows the comparison between the dielectric losses (ε'') of OPC at different *w/c* ratios at two different temperatures (T = 120 K (a) and T = 155 K (b)), where the similarities of the response for different *w/c* ratio are evident.

The dielectric response in Figure VII.2 can be described by using standard fit functions. We used the symmetric Cole–Cole function to describe each relaxation process (see chapter III). Over the temperature range of 100 to 150 K we found two dielectric processes (1 and 2) whereas over the temperature range of 150 to 250 K three relaxations (3, 4 and 5) were found. In addition, at low frequencies conductivity effects dominate, and to account for that a power law term was added (last term in eq. VII.1),

where ε_0 denotes the vacuum permittivity and σ is the static ionic conductivity. The total fit function was given by:

$$\varepsilon^*(\omega) = \varepsilon_\infty + \sum_{j=1}^{5} \frac{\Delta\varepsilon_j}{1+(i\omega\tau_j)^{\alpha_j}} - i\left(\frac{\sigma}{\varepsilon_o\omega}\right)^N \quad \text{(VII.1)}$$

In figure VII.2.d is observed that the intensity of processes 1 to 3 increases with water content and the maximum of the curves remain almost at the same frequency following the typical behavior observed in other confinement systems [11,12] where no crystallization of water was observed. Therefore, these dielectric processes are related with the dynamic of amorphous water (i.e. no crystalline). Two other slower processes (4 and 5) are also visible in the dielectric spectra, but here we will focus on the low temperature relaxation (processes 1 to 3).

c.1 Temperature dependence of the relaxation times and shape factors

Figure VII.3 (a) shows the temperature dependence of the relaxation times for different *w/c* ratio. Whereas processes 1 and 2 displays Arrhenius-type temperature dependence, process 3 exhibits a crossover from different Arrhenius-type temperature dependence below and above ~ 165 K. Table VII.1 shows the values of E_a and log (τ_0) for processes 1 to 3.

The relaxation times of processes 1 to 3 are basically independent of the water content, as normally observed for water molecules in hard confinement systems [11], although the intensity of these processes are affected by the water content. Thus, these processes exhibit the typical behavior of water molecules relaxing in a hard confinement environment [11,12].

The temperature dependence of the relaxation strength ($\Delta\varepsilon$) for different *w/c* ratios are shown in Figure VII.3 (b, c and d). The intensity of all the processes remains almost constant with temperature as typically for a local process. $\Delta\varepsilon_3$ depends on *w/c* ratio (and therefore on water content) whereas for processes 2 and 3 a weak dependence

on *w/c* ratio is observed. In the following we discuss the origin of each relaxation process and the relationship with water confined in C-S-H gel.

Table VII.2. Activation Energy (*Ea*) and Pre-Exponential Factor (log (*τo*)) obtained from the data in Figure VII.3.

Sample	*w/c*	c_w [wt%]	Process 1		Process 2		Process 3 (Below 155 K)	
			log (τ_0)	E_a [eV]	log (τ_0)	E_a [eV]	log (τ_0)	E_a [eV]
Cem-0.40	0.40	24.50	-14.05	0.21	-13.95	0.26	-13.50	0.40
Cem-0.35	0.35	22.10	-12.80	0.18	-13.80	0.26	-13.70	0.40
Cem-0.30	0.30	18.10	-14.50	0.22	-13.90	0.26	-13.70	0.40

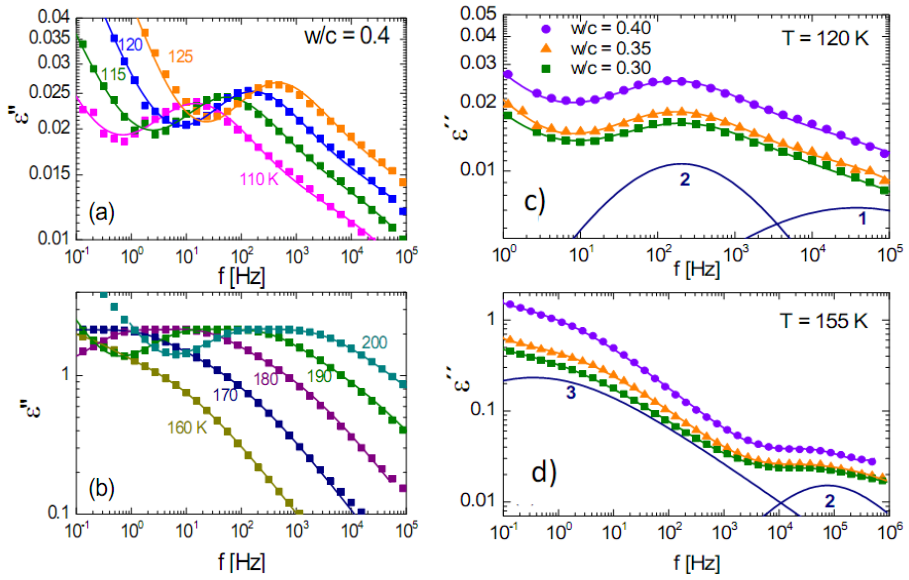

FigureVII.2. (a and b) Imaginary part (*ε´´*) of the dielectric spectra of Portland cement with *w/c* = 0.4 at different temperatures (see plot). The solid lines through the data points represent the fits to the experimental data. **(c and b)** Imaginary part (*ε´´*) of the dielectric spectra of Portland cement at different *w/c* ratio at T= 120 K (c)) and T = 155 K (d)). The solid lines through the data points represent the fits to the experimental data. In addition, all the processes

c.2 Interpretation of the dielectric processes

Water molecules in OPC are principally situated in the inter-laminar pore space between the calcium silicate layers. In addition Ca^{2+} cations, which balance the negative charge of the main alumino-silicate layer [13], are also located in the inter-laminar pore space. Water molecules can interact with these cations and with the hydroxyl groups in the surface of silicate chains. Regardless of the model considered, the structure of cements comprises pores of different sizes in which water molecules can be also located. With regards to the topology of the pore network and, compared with other

silica-based confinement systems such as MCM-41, SBA-15, or molecular sieves [14,15], cement materials are much more complex systems. In hydrated cements, there are different multiple crystalline hydrates (for instance portlandite or ettringite) immersed in C-S-H gel matrix, which in addition has also a complex pore distribution [16]. Whereas MCM-41 has a cylindrical shaped pore pierced by large holes which do not greatly perturb the wall structure, the shapes and the topology of the pore network in Portland cements are much disordered [17]. As water molecules are an integral part of this pore network, it is not surprising to obtain a rich and complex dielectric spectrum corresponding with the dynamics of water molecules.

for sample *w/c* = 0.3 are shown in both Figures.

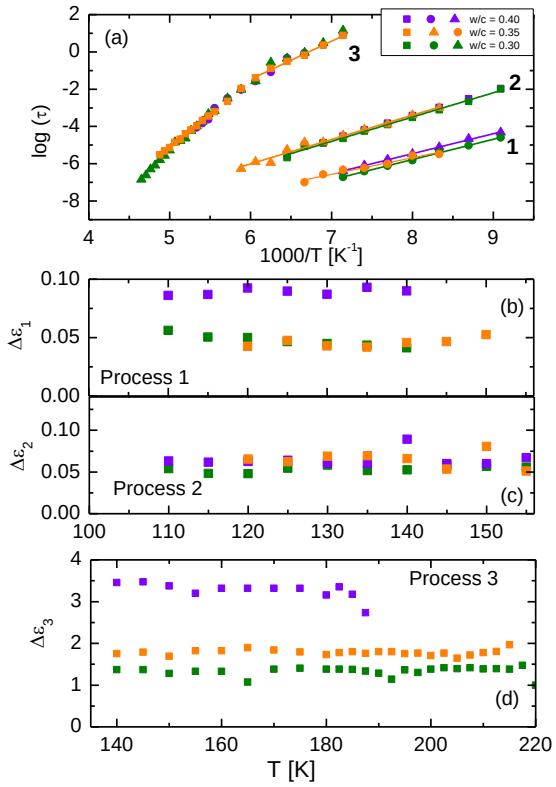

Figure VII.3. (a) Temperature dependence of relaxation times of water confined in cements with different *w/c* ratio. **(b-d)** Temperature dependence of relaxation strength ($\Delta\varepsilon$) of Processes 1 to 3 and for different *w/c* ratio.

As above mentioned processes 1 to 3, reflects the dynamics of amorphous water in the pore network of cements. The activation energy of processes 1 and 2 are 0.20 and 0.26 eV respectively of all *w/c* ratios. These values are lower than the activation energy of the more collective behavior of confined water (0.5 eV) [18] and therefore in our case, a weak hydrogen bond network could be formed. In other words, these two

dielectric processes have origin in water molecules without interactions with so many other water molecules. By contrast, process 3 (below 165 K) has higher activation energy (0.40 eV) and even higher at T > 150 K (0.70 eV). These values are compatible with a more extended hydrogen bond network of water molecules [11, 18].

Due to the low activation energy of processes 1 and 2, they could correspond with the relaxation of water in ice which is also present in samples. To rule out this possibility, we dried the sample *w/c* = 0.4 at 80 ^{o}C during 90 min (see Figure VII.4). After this drying, most of the water molecules can be evaporated and we do not expect crystallization (as confirmed by calorimetric measurements). In this dried sample, we still can observe both processes 1 and 2. Both intensities are smaller than that of undried sample (because the lower water content) and the relaxation times are similar to the original sample. Thus, we can rule out that the origin of these processes is the ice contained in the samples and in addition, we confirmed that the relaxation of water molecules is the origin of these processes.

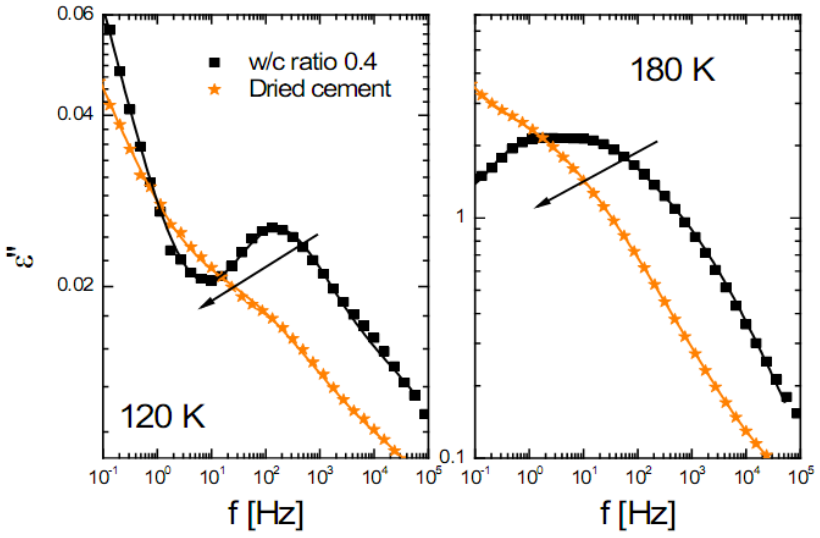

Figure VII.4. Imaginary permittivity signal of the Cem-0.4 before and after the drying process.

The temperature dependence of the relaxation time of processes 1 to 3 (see Figure VII.3) does not vary with *w/c* ratio. As mentioned above, this is a typical behavior of the relaxation time of water under hard confinement systems where the shape of the pore is well-defined [11]. This behavior contrasts with water confined in isolated C-S-H gel, where significant variations of the relaxation time with water content were observed [6]. This indicates that the “isolated C-S-H gel” and the “C-S-H

grown within cements" have not the same structural characteristics. We have to notice that the pore network of the previously studied C-S-H gel [5,6], can more easily grow in an "empty" environment compared with the developing of C-S-H gel within cements, where several hydration products coexist. Thus, in the case of "isolated C-S-H gel" we assume a more disordered and inter-connected network with further variation of size and shape of the pores. By contrast in Portland cement, after 3 weeks of hydration, we expect a denser morphology of C-S-H gel than in isolated C-S-H gel. This could be the reason for which the shape of the pores seems to be more defined in the case of C-S-H within cements.

Following the above result, process 3 reflects the dielectric response of water in C-S-H gel but in a more compact network and with pore size and topology better defined than in isolated C-S-H gel. In agreement with this result, Figure VII.5 shows the comparison of the relaxation times of process 3 with water confined in molecular sieves [19]. The relaxation times are very similar in both systems. Molecular sieves are crystalline metal alumino-silicates having a three dimensional interconnecting network of silica and alumina tetrahedral similar to that found in cements. Therefore, it is not surprising to obtain a similar response. However, for the relaxation times of water confined in molecular sieves represented in Figure VII.5, it is known that the average pore size is 1 nm [19]. We can therefore assume that process 3 is related with water in pores about of 1 nm. In agreement with this, process 3 exhibits a crossover from an Arrhenius to other Arrhenius dependence as the temperature decreases (see Figure 4a) at ~165 K. This feature has been observed for water confined in C-S-H gel [5,6] as well as in several confinement systems [11,12,19,20]. We have associated this crossover with confinement effects which are produced by the matrix where water is situated [18]. This confinement effect is usually observed for water in small cavities in agreement with the comparison with molecular sieves of 1 nm.

Focusing on process 1, Figure VII.5 shows the comparison of the temperature dependence of the relaxation times this process observed in isolated C-S-H gel and in Portland cement. The relaxation times of process 1 in both systems are very similar suggesting the same origin in both cases. Process 1 in C-S-H gel was associated with the rotation of hydrated dipolar group (hydroxyl groups) in its internal surface [5] and we expect the same origin for water confined in Portland cement. In contrast to process

3, where a different dynamical behavior was observed between isolated- and in-cement CSH, in this case we do not expect such changes. This is due to the different origin of both processes. Process 1 is originated in the reorientation of hydroxyl groups on the internal surfaces and this should be independent of the topology of the pore network. Thus, it is not surprising obtain a similar result in this case.

Now we discuss the origin of process 2. As τ_2 is significantly different of τ_1 and τ_3, a different water population should be the origin of this process. We therefore consider different environments for water molecules in Portland cement. The first possibility is that water molecules located are in cavity of a different size of 1nm (origin of process 3). In fact, Jennings´s model assumed two different sizes for the gel pores (1 nm and 3-10 nm) [16] and we also observe two water dynamics in the case of isolated CSH gel. However, the dynamics of water in bigger pores than 1 nm is expected to be slower than that observed for 1 nm pores. This is not our case, because process 2 is significantly faster than process 3. In addition, it has been proposed the existence of two types of morphologies of CSH gel in cements (the so called “early” and “late”, “outer” and “inner” products or “low-density” and “high-density” CSH gel). As these two types of gels are produced by the presence of the other components in cements, these two varieties are not developed in the isolated CSH gel and therefore, this process 2 was not previous observed. However, the relaxation time of process 2 is much faster than that observed in several confinement systems of different sizes [11]. Therefore, we discard that this process corresponds with the relaxation of water molecules in a cavity of a given size or even in another variety of CSH gel.

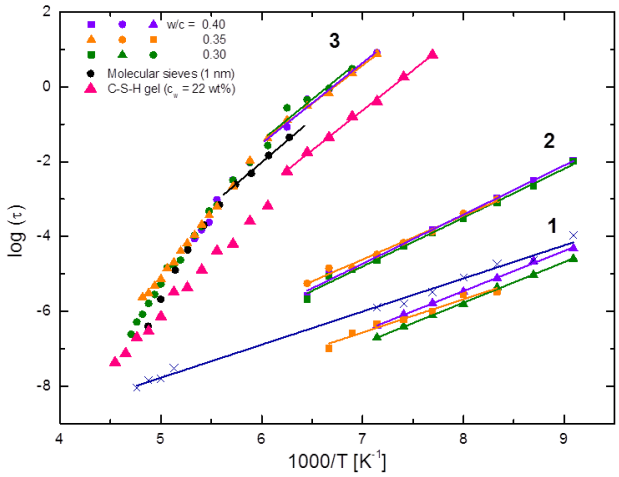

Figure VII.5. Temperature dependence of the relaxation time $\tau(T)$ obtained from the cement samples with different *w/c* ratio for the processes 1, 2 and 3.

Given the fact than process 2 has a low activation energy (0.26 ev), it is much faster than water located in holes of different sizes and it the typical crossover usually observed in pores is not observed, we guess that these water molecules are located in the a more local environment than water in a pore. One possibility to consider is the hydration water around Ca^{2+} cations which are a significant ingredient in Portland cements. Water around Ca^{2+} cations arrange in a hexagonal ring and water molecules can relax in this environment. However, we cannot make in this case an assignment for this process.

d. Conclusions

Summarizing, at supercooled temperatures we find three different populations of water each of them related with water molecules in different environments: hydration water close to hydroxyl groups (process 1), water in 3D pores of ~1 nm (process 3) and a third environment which could be hydration water of Ca^{+2} atoms.

f. References

1. Scrivener, K. L. & Nonat, A. Hydration of cementitious materials, present and future. *Cem. Concr. Res.* **41,** 651–665 (2011).

2. Taylor, H. F. *Cement Chemistry:2nd edition*. *1990*

3. Vandamme, M. & Ulm, F.-J. Nanogranular origin of concrete creep. *Proc. Natl. Acad. Sci. U. S. A.* **106,** 10552–7 (2009).

4. Manzano, H. *et al.* Confined water dissociation in microporous defective silicates: mechanism, dipole distribution, and impact on substrate properties. *J. Am. Chem. Soc.* **134,** 2208–15 (2012).

5. Monasterio, M., Jansson, H., Gaitero, J. J., Dolado, J. S. & Cerveny, S. Cause of the fragile-to-strong transition observed in water confined in C-S-H gel. *J. Chem. Phys.* **139,** (2013).

6. Cerveny, S. *et al.* Effect of hydration on the dielectric properties of C-S-H gel. *J. Chem. Phys.* **134,** 034509 (2011).

7. Mindess, S. & Young, J. F. *Concrete*. 671 (1981).

8. Hansen, T. C. Physical structure of hardened cement paste. A classical approach. *Mater. Struct.* **19,** 423–436 (1986).

9. Snyder, K. A. & Bentz, D. P. Suspended hydration and loss of freezable water in cement pastes exposed to 90% relative humidity. *Cem. Concr. Res.* **34,** 2045–2056 (2004).

10. Ridi, F., Luciani, P., Fratini, E. & Baglioni, P. Water confined in cement pastes as a probe of cement microstructure evolution water confined in cement pastes as a probe of cement microstructure evolution. *J. Phys. Chem. B* **113,** 3080–7 (2009).

11. Swenson, J. & Cerveny, S. Dynamics of deeply supercooled interfacial water. *J. Phys. Condens. Matter* **033102,** 33102 (2015).

12. Cerveny, S., Barroso-Bujans, F., Alegría, Á. & Colmenero, J. Dynamics of Water Intercalated in Graphite Oxide. *J. Phys. Chem. C* **114,** 2604–2612 (2010).

13. Van Maaren, P. J. & van der Spoel, D. Molecular Dynamics Simulations of Water with Novel Shell-Model Potentials. *J. Phys. Chem. B* **105,** 2618–2626 (2001).

14. Liu, Z. *et al.* A review of fine structures of nanoporous materials as evidenced by microscopic methods. *Reprod. Syst. Sex. Disord.* **62,** 109–46 (2013).

15. Han, L. *et al.* Structures of Silica-Based Nanoporous Materials Revealed by Microscopy. *Zeitschrift für Anorg. und Allg. Chemie* **640,** 521–536 (2014).

16. Jennings, H. M., Thomas, J. J., Gevrenov, J. S., Constantinides, G. & Ulm, F.-J. J. A multi-technique investigation of the nanoporosity of cement paste. *Cem. Concr. Res.* **37,** 329–336 (2007).

17. Coasne, B., Galarneau, A., Pellenq, R. J. M. & Di Renzo, F. Adsorption, intrusion and freezing in porous silica: the view from the nanoscale. *Chem. Soc. Rev.* **42,** 4141–71 (2013).

18. Cerveny, S., Alegría, Á. & Colmenero, J. Universal features of water dynamics in solutions of hydrophilic polymers, biopolymers, and small glass-forming materials. *Phys. Rev. E* **77,** 031803 (2008).

19. Jansson, H. & Swenson, J. Dynamics of water in molecular sieves by dielectric spectroscopy. *Eur. Phys. J. E. Soft Matter* **12 Suppl 1,** S51–4 (2003).

20. Sjöström, J., Swenson, J., Bergman, R. & Kittaka, S. Investigating hydration dependence of dynamics of confined water: monolayer, hydration water and Maxwell-Wagner processes. *J. Chem. Phys.* **128,** 154503 (2008).

Chapter VIII

Final Conclusion

Along this thesis, we have performed a detailed studied of the dynamics of water in different hard confinements systems with variable nano-porosity. The selected nanostructures were porous silicate based materials. These kind of porous materials have important applications in the fields of energy, adsorption, catalysis and geological science. In addition, the study of these systems has consequences on the basic problems related to the dynamics of confined water at supercooled temperatures. In particular, we focused on nanostructures related with cementitious materials.

First, we have explored the dynamics of water in C-S-H gel. C-S-H gel is a disordered nanostructured material and responsible for most of the engineering properties of cement paste. This study has allowed us to better understand the way in which water is distributed along the pore network of C-S-H gel. The water content has a large influence on the dynamics. The results showed three dynamics associated with water molecules located in pores of different sizes and with non-removable and dielectrically active hydroxyl groups on the surface of the C-S-H gel. As in several confinement systems at high hydration level, a crossover associated to confinement effects was observed for the dynamics in small gel pores. The present dielectric study shows no sign of the fragile-to-strong transition as previously has been indicated by QENS for a similar system. Instead, the apparent crossover in the temperature dependence was shown to be due to that the analysis is performed in a very limited frequency interval, which, in turn, masks the merging between the main water relaxation and a faster relaxation process (Chapter IV).

Other of the systems we have studied was C-S-H gel synthesized with nano-particles (Chapter V). We have analyzed the changes produced in the structure of C-S-H because of the presence of nanoparticles by means of NMR and FTIR spectroscopy. In this case, the silicate chains are longer than in C-S-H without the addition of nanoparticles. In this context, dynamic of water also has changed. The dynamics of water in small pores becomes faster when water is confined in this different matrix with longer silicate chains.

In Chapter VI we have studied aluminum substituted tobermorite. Tobermorite has a defined crystalline structure, similar to the C-S-H gel, but with even longer silicate chains. We have distinguished two different water dynamics due to different environments where water is located. Water in aluminum rich cavities is faster than water in siliceous rich cavities. The impact of aluminum impurities on the water dynamics could be of importance to understand ion migration and chemical degradation of fly-ash and slag Al-rich cements.

In Chapter VII, we have studied the dynamics of water in Portland cement. Portland cement has a very broad distribution of pores (sizes and topology) and therefore the results are more complex. Although the complete picture is still not fully understood, we have some promising results for futures works. We have observed that one of the fastest processes (process 3) has the same universal dynamics founded in other confinement systems. In particular water in molecular sieves has the same water dynamics at low temperature.

Finally, here we compare the relaxation time of the main water process founded in all the systems analyzed: C-S-H, C-S-H with nanoparticles and tobermorite. We can observe that the relaxation time becomes faster when the silicate chain becomes longer: increasing the silicate chain, water is more interfacial. However, for Portland cement the response is two decades slower. This should be related with the different environment of C-S-H gel when immersed in the cement network and therefore a different dynamic is observed. This result could be of some importance for modeling the structure of C-S-H as well as for molecular dynamic simulations of water in these types of materials.

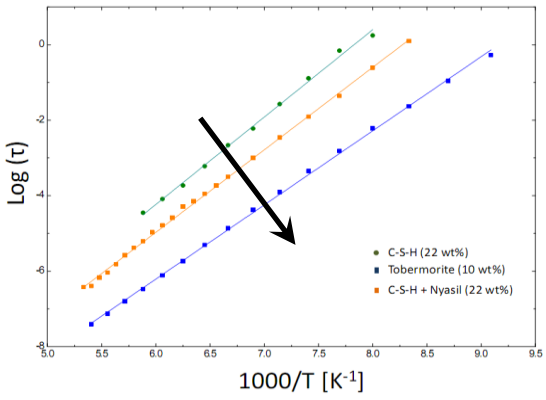

Figure VIII.1. Temperature dependence of the relaxation time of C-S-H gel, CSH-nanoparticles and synthetic tobermorite.

List of Publications

This thesis has contributed to the following publications:

1. ***Cause of the fragile-to-strong transition observed in water confined in C-S-H gel.***
   Manuel Monasterio, Helen Jansson, Juan J. Gaitero, Jorge Dolado, Silvina Cerveny.
   J. Chem. Phys. 2013, **139** (16), 164714.

2. ***Effect of addition of silica- and amine functionalized silica-nanoparticles on the microstructure of C-S-H gel.***
   Manuel Monasterio, Juan José Gaitero, Edurne Erkizia, Ana M. Guerrero Bustos, Luis A. Miccio, Jorge S. Dolado, Silvina Cerveny.
   Accepted in *Journal of Colloid And Interface Science (2015)*

3. ***Effect of chemical environment on the dynamics of water confined in calcium silicate minerals - natural and synthetic tobermorite.***
   Manuel Monasterio, Juan José Gaitero, Hegoi Manzano, Jorge S. Dolado, Silvina Cerveny.
   Langmuir (2015) (under Review)

4. ***Dynamics of nano-confined water dynamics in Portland cement of different water-to-cement ratio.***
   Manuel Monasterio, Helen Jansson, Silvina Cerveny.
   Manuscript in preparation (2015)